Max-Planck-Institut für Festkörperforschung

Stuttgart

MAX-PLANCK-INSTITUT
für Festkörperforschung

2007

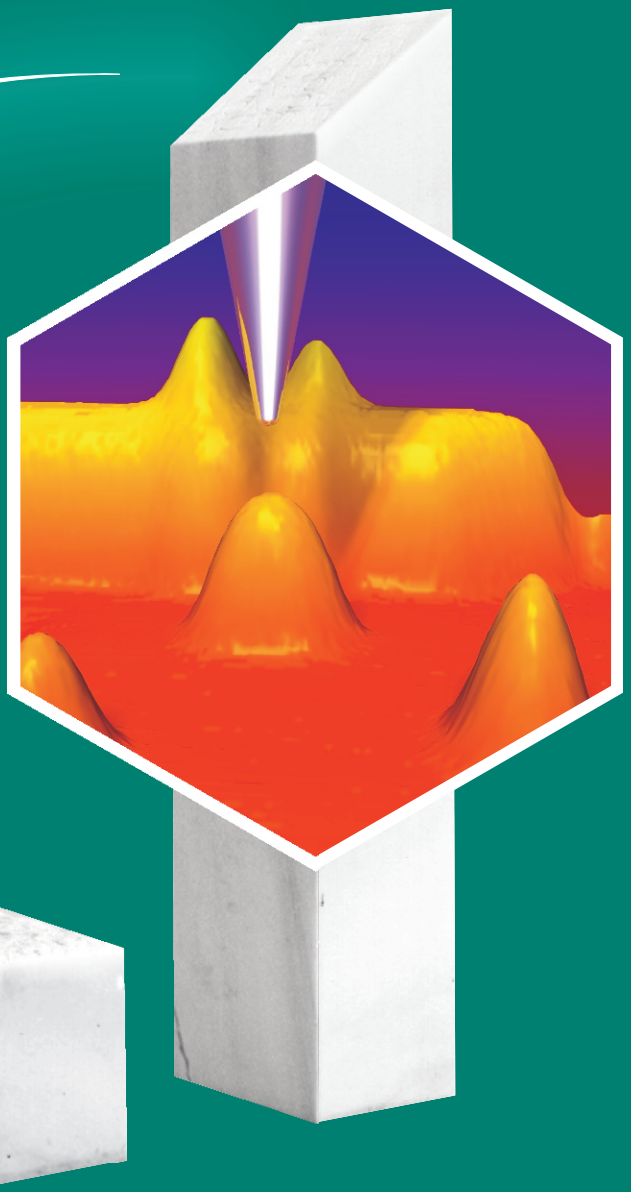

MAX-PLANCK-INSTITUT FÜR FESTKÖRPERFORSCHUNG

STUTTGART

ANNUAL REPORT

JANUARY 1st – DECEMBER 31st, 2007

Max-Planck-Institut für Festkörperforschung
Heisenbergstraße 1, D–70569 Stuttgart
Postfach: 80 06 65, D–70506 Stuttgart
Telefon: (0711) 6 89 – 0
Telefax: (0711) 6 89 – 10 10

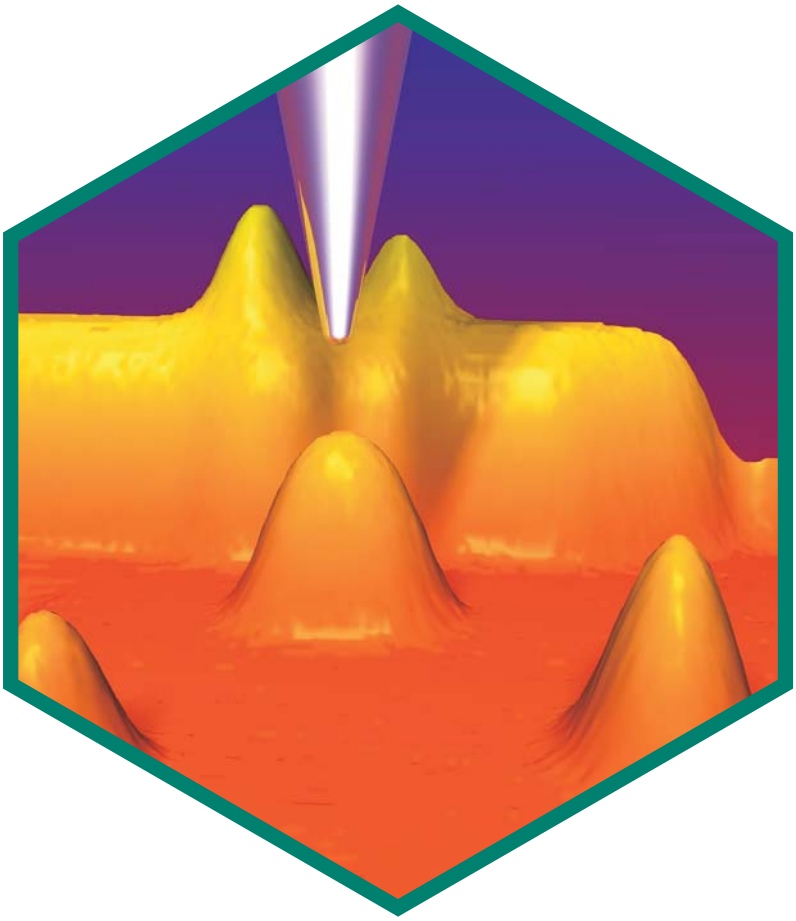

About the hexagon on the title page

Artists view of the experimental setup which has been used to measure the exchange interactions between single magnetic adatoms (cf. p. 25). The metallic tip of the microscope is placed on top of a chain of three cobalt adatoms on a copper (100) surface. The bump to the left is a single cobalt adatom. The surface morphology is obtained from an low-temperature scanning tunneling microscope image. Tunneling spectra acquired with the tip positioned above cobalt adatoms in dimers and trimers reveal characteristic spectroscopic signatures which can be exploited to assess magnetic interactions between single atoms.

Corresponding article:
Wahl, P., P. Simon, L. Diekhöner, V.S. Stepanyuk, P. Bruno, M.A. Schneider and K. Kern.
Exchange interaction between single magnetic adatoms. Physical Review Letters **98**, 056601 (2007).

In this report we intend to give an impression of the manifold scientific activities at the Max-Planck-Institut für Festkörperforschung during the year 2007. In the first part, we present some highlights of the scientific accomplishments in our Departments, Junior Research Groups, and Scientific Service Groups. The second part contains a complete list of publications as well as other useful information on our Institute. More details can be found on our web page 'www.fkf.mpg.de'.

This year another Independent Junior Research Group, led by Gabriel Bester, was established at the Institute. The new group performs ab initio calculations of semiconductor nanostructures, complementing nicely experimental research on nanostructured systems at the Institute.

We thank all the members of the Institute for their hard work and dedication. It is thanks to their efforts and performance that the Institute has been able to maintain its high standard of research.

Stuttgart DAS KOLLEGIUM

May, 2008

Contents

Selected Research Reports

Nanostructures

Rational synthesis and structure of complex compounds

Ion conduction

Organic and carbon-based materials

Superconductivity

Electron interactions and unusual electronic properties

Chemistry

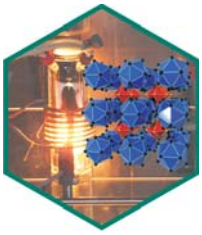

JANSEN's department puts its main emphasis on basic research in the field of preparative solid state chemistry with the goal of developing modern materials. Classes of materials currently under investigation include oxides and nitrides of metals and nonmetals as well as fullerenes, e.g., new binary and ternary oxides synthesized under high oxygen pressure, ionic conductors, structural oxide ceramics and pigments, amorphous inorganic nitridic covalent networks, or endohedral fullerenes and fullerides.
Besides employing traditional solid state synthesis methods, a large number of alternative techniques is used, e.g., the sol-gel process, synthesis under high pressure, via an rf-furnace, at low temperatures in liquid ammonia, by electrochemical methods, or by low-temperature atomic beam deposition. Optimizing the syntheses of these materials is only a first, though crucial step, however. In addition, their chemical and physical properties, in particular optical, electrical and magnetic behavior, are analyzed both at high and low temperatures, with particular emphasis on X-ray diffraction and spectroscopic methods. This provides the basis for placing the results in the proper context regarding structure-property relationships and modern concepts of bond theory.
A long-term goal of the department is to increase the predictability of solid state chemistry, i.e., to predict the existence of not-yet synthesized compounds, calculate their properties, and finally provide prescriptions for their synthesis. This work involves both theoretical and synthetic aspects. On the theoretical side, structure candidates are determined by studying the energy landscapes of chemical systems using global exploration techniques, while on the preparative side kinetically controlled types of reactions that allow low-temperature synthesis of (possibly metastable) compounds are being developed. [29,33,84]

⬡ LHS: When simultaneously evaporating graphite and a metal in an rf-furnace (shown), endohedral fullerenes can be synthesized in relatively high yields. RHS: Synthesis at high oxygen pressures produces novel materials with interesting electronic, chemical and physical properties. Compounds such as $Ag_{13}OSO_6$ (shown) are characterized using various spectroscopic, physical and diffractive methods.

MAIER's department is concerned with physical chemistry of the solid state, more specifically with chemical thermodynamics and transport properties. Emphasis is laid on ion conductors (such as inorganic or organic proton, metal ion and oxygen ion conductors) and mixed conductors (typically perovskites). As local chemical excitations (point defects) are responsible for ion transport and simultaneously represent the decisive acid-base active centers, a major theme of the department is the understanding of mass and charge transport, chemical reactivities and catalytic activities in relation to defect chemistry. This includes experiments (in particular electrochemical studies) as well as theory (in particular phenomenological modelling), and comprises investigations of elementary processes but also of overall system properties. In this context, interfaces and nanosystems are to the fore.
Since electrochemical investigation immediately affects the coupling of chemical and electrical phenomena, the research is directed towards both basic solid state problems and the technology of energy and information conversion or storage (fuel cells, lithium-batteries, chemical sensors).

Conceptually speaking, we want to address the following questions: Can we – given the materials, the control parameters and the driving force – understand or even predict concentrations, mobilities and reactivities of ionic charge carriers? How do these properties change at interfaces and in confined systems? What are the basic mechanisms of ion transport and ion transfer? How can we use this fundamental knowledge to develop at will materials for given (or novel) applications? [45,47,49]

⬡ Ionic and electronic charge carriers (e.g., vacancies) are the relevant particles as far as chemical kinetics and mass transport is concerned. They are establishing the interaction with the neighboring phases and act on electrical and chemical driving forces.

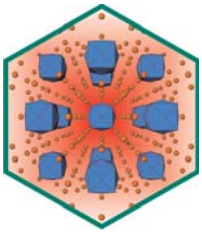

SIMON's department emphasizes the investigation of metal-metal bonding with main group, *d*- and *f*-metals. The purpose of the work is on one side the development of structural concepts (e.g., condensed cluster concept) and on the other side the search for new materials, their phase relationships and connections between structure, chemical bonding and properties.
Targets are metal-rich compounds of transition metals, particularly oxides and halides, reduced rare earth metal halides, hydride, carbide, boride, boride carbide, aluminide and silicide halides of the rare earth metals, alkali and alkaline earth metal suboxides and subnitrides. Electron microscopy is used to characterize microcrystalline phases up to full structure refinement as well as analysis of real structure. Superconductivity is of special interest following a chemical view of the phenomenon in terms of a tendency towards pairwise localization of conduction electrons in a flat band–steep band scenario. New colossal magnetoresistance materials result from an interplay of *d*- and *f*-electrons.
Other fields of interest are structures of molecular crystals, in particular, *in situ* grown crystals of gases and liquids. Experimental techniques like diffractometry with X-rays and neutrons, high-resolution transmission electron microscopy, electron crystallography and measurements of magnetic susceptibility as well as electrical transport properties are used. [31,39]

⬡ $Ba_{14}CaN_6Na_{14}$ – subnanodispersed salt in a metal.

Physics

KEIMER's department studies the structure and dynamics of highly correlated electronic materials by spectroscopic and scattering techniques. Topics of particular current interest include the interplay between charge, orbital and spin degrees of freedom in transition metal oxides and the mechanism of high-temperature superconductivity. Experimental techniques being used include elastic and inelastic neutron scattering, normal and anomalous X-ray scattering, Raman scattering off and in resonance, spectral ellipsometry (including synchrotron radiation as a source), and infrared, Raman, and X-ray measurements under high magnetic fields. Experiments at external neutron sources are carried out on a regular basis, and a spectrometer at the new research reactor FRM-II in Munich has recently been completed. The latter instrument uses a novel combination of triple axis and neutron spin echo techniques to optimize the energy resolution and allow the determination of lifetimes of magnetic and lattice vibrational excitations throughout the Brillouin zone.
The group operates a high-magnetic field facility for X-ray scattering at the National Synchrotron Light Source (NSLS) at Brookhaven National Lab (USA). At the ANKA synchrotron in Karlsruhe, the group also operates Fourier ellipsometers for the far infrared spectral range. Close collaborations also exist with the theory and chemistry departments at the MPI-FKF; with the Crystal Growth Service Group where large, high-quality single crystals of oxide compounds are prepared with optical furnaces, and with the Technology Service Group that prepares state-of-the-art oxide heterostructures and superlattices. [19,67]

⬡ Investigation of a mosaic of crystals of a high-temperature superconductor with neutron beams (yellow). Neutrons are elementary particles that generate a magnetic field through their internal rotation ('spin'), similar to a tiny bar magnet. When a neutron beam falls onto a magnetic material, the neutron spin is flipped and the beam is deflected. In experiments with neutron beams, Max Planck scientists are studying an unusual, fluctuating magnetic order in high-temperature superconductors that could be of central importance for an explanation of this phenomenon.

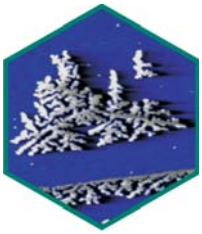

Research efforts in KERN's department are centered on nanometer-scale science and technology, primarily focusing on solid state phenomena that are determined by small dimensions and interfaces. Materials with controlled size, shape and dimension ranging from clusters of a few atoms to nanostructures with several hundred or thousand atoms, to ultrathin films with nanometer thickness are studied.
A central scientific goal is the detailed understanding of interactions and processes on the atomic and molecular scale. Novel methods for the characterization and control of processes on the atomic scale as well as tools to manipulate and assemble nanoobjects are developed. Of particular interest are: Self-organization phenomena, atomic scale fabrication and characterization of metal, semiconductor and molecular nanostructures, quantum electronic transport in nanostructures, atomic scale electron spectroscopy and optics on the nanometer-scale. As surface phenomena play a key role in the understanding of nanosystems, the structure, dynamics and reactivity of surfaces in contact with gaseous or liquid phases are also in the focus of interest. [25,55,63,90]

⬡ The scanning tunneling microscope image shows a silver dendrite grown at 130 K on a platinum (111) surface.

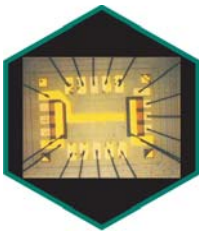

The electronic properties of heterostructures, quantum wells, superlattices and carbon based quantum structures (graphene, nanotubes), in particular the influence of quantum phenomena on the transport and optical response are the main topics in VON KLITZING's department. Optical and transport measurements in magnetic fields up to B = 21.5 Tesla and temperatures down to 10 mK combined with TEM/scanning probe techniques are used to characterize the systems. Picosecond sampling techniques are developed for ultrafast time-resolved measurements on nanodevices. The quantum Hall effect is studied by analyzing time-resolved transport, edge channels, the behavior of composite fermions and the response on microwave radiation and surface acoustic waves. Time-resolved photoconductivity, luminescence, and Raman measurements in magnetic fields are methods of characterizing the low-dimensional electronic systems. Coupled two- and zero-dimensional electronic systems are produced by highly specialized molecular beam epitaxy growth and by electron beam lithography. Phenomena like electron drag, exciton condensation, Kondo resonance, Coulomb blockade, ballistic transport, commensurability phenomena in periodically modulated two-dimensional systems and the interaction between electron and nuclear spins are investigated. The detection and generation of terahertz radiation using low-dimensional electron systems is one of the new research activities. [21,61,82]

⬡ Demanding technologies are needed for the preparation of devices used in quantum transport experiments. The figure shows a typical example where the combination of interrupted epitaxial growth, special etching processes, focused ion beam writing, contact diffusion, and gate evaporation leads to two electron layers with a distance of only 10 nm and separate contacts.

Theory

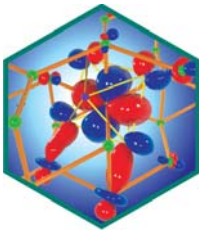

The electronic structure plays a key role in determining transport, magnetic, optical, and bonding properties of solids. The members of Abteilung ANDERSEN study the electronic structure of both weakly and strongly correlated materials, where the dominating energy of the electrons is the kinetic and Coulomb energy, respectively.

The work on weakly correlated systems is based on the density functional formalism. For strongly correlated systems, an essential aim is to introduce chemical realism into the description also of these materials by developing realistic model Hamiltonians, e.g., by using down-folding in the NMTO method. The model Hamiltonians have been solved in the static and dynamical mean-field approximations, often together with Karsten Held and collaborators from Metzner's department. Of particular interest has been metal-insulator transitions in transition metal oxides, as well as magnetic, optical, and dynamical properties studied experimentally in Keimer's department. Another focus of the department is the interaction between electrons and nuclei, the electron-phonon interaction, which is important for superconductivity and other transport properties of many metals. Materials of particular interest has been intercalated graphites, studied together with the Chemical Service Group, transition metal compounds, high-T_c cuprates, and fullerides. [96]

⬡ One of the three congruent t_{2g} NMTO Wannier-like orbitals for V_2O_3. Lobes of opposite signs are respectively red and blue.

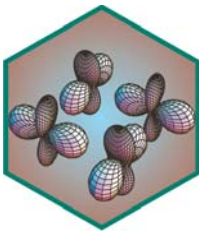

Electronic properties of solids are analyzed and computed in METZNER's department with a main emphasis on systems where electronic correlations play a crucial role, such as cuprates, manganites and other transition metal oxides. Besides symmetry-breaking phase transitions leading to magnetism, orbital and charge order, or superconductivity, correlations can also cause electron localization and many other striking many-body effects not described by the generally very successful independent electron approximation.

Our present research focuses in particular on high-temperature superconductors with their complex interplay of magnetic, superconducting and charge correlations, and also on manganites and vanadates, whose electronic properties are determined by the interplay of orbital, spin and charge degrees of freedom. Another topic is the influence of lattice degrees of freedom on electronic properties, via Jahn-Teller distortion and electron-phonon interaction. Besides bulk properties of one-, two- and three-dimensional systems also problems with a mesoscopic length scale such as quantum dots and inhomogeneous quantum wires are being studied. The correlation problem is attacked with various numerical and field-theoretical techniques: exact diagonalization, density matrix renormalization group, dynamical mean-field theory, functional renormalization group and (1/N)-expansion. Modern many-body methods are not only being applied, but also further developed within our group. [72,75]

⬡ Orbital order in a single layer of undoped $LaMnO_3$. The study of electronic properties of doped manganites, which show such remarkable phenomena like the colossal magnetoresistance, is an active research field because of the subtle interplay of charge, orbital, spin and lattice degrees of freedom.

Junior Research Groups

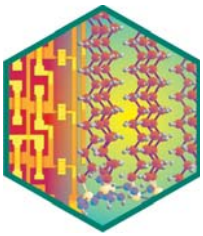

Research in the ORGANIC ELECTRONICS GROUP (Klauk) focuses on novel functional organic materials and on the manufacturing and characterization of organic electronic devices, such as high performance organic thin-film transistors, carbon nanotube field-effect transistors, inorganic nanowire field-effect transistors, and organic/inorganic hybrid radial superlattices. Of particular interest is the use of organic self-assembled monolayers in functional electronic devices. For example, we are developing materials and manufacturing techniques that allow the use of high-quality self-assembled monolayers as the gate dielectric in low voltage organic and inorganic field-effect transistors and low power integrated circuits on flexible substrates. We are also studying the use of self-assembled monolayers for the preparation of nanoscale organic/inorganic superlattices that exhibit unique optical and mechanical properties. Scientific work in organic electronics is highly interdisciplinary and involves the design, synthesis and processing of functional organic and inorganic materials, the development of microfabrication techniques, device and circuit design, manufacturing, and materials and device characterization. [58]

⬡ n-Octadecylphosphonic acid $C_{18}H_{37}PO(OH)_2$ forms dense, insulating monolayers on natively oxidized metal substrates, such as aluminum. As a high-capacitance gate dielectric, these monolayers allow organic transistors and large-scale digital circuits (background) to operate with low voltage (1.5 V) and low power (1 nW per gate).

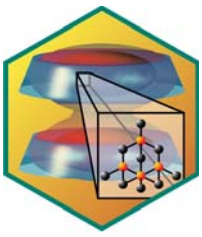

The Independent Junior Research Group THEORY OF SEMICONDUCTOR NANOSTRUCTURES (Bester) was established in October 2007. The research will focus on the theory of semiconductor nanostructures. The special interest resides in quantum mechanical effects that become apparent when the carriers of charge and magnetic moment, i.e., electrons or holes, are confined into space regions with dimensions in the nanometer range. The aim is to develop theoretical concepts and implement them into computational methods where the atomistic nature of the problem is retained. At one end of the size scale, when the confining region encompasses only dozens of atoms, we are in direct contact with the chemical world of molecules. At the other side of the length scale we enter the fast growing and expanding world of artificially structured solids, such as quantum wells, quantum wires and quantum dots. We work in close collaboration with experimentalists to benchmark our theory and to provide understanding and insight into the quantum states probed experimentally.

⬡ State density of the bonding electron state of two vertically stacked self-assembled InGaAs quantum dots (quantum dot molecule) calculated with the atomistic empirical pseudopotential method. The dots have the shape of a truncated cone with 25 nm diameter and a vertical separation of 5 nm. The two translucent red isosurfaces enclose 75% and 40% of the total state density. The physical dot dimensions are shown in blue.

The ULTRAFAST NANOOPTICS GROUP (Lippitz) is a joint junior research group of the Max Planck Institute for Solid State Research and the Department of Physics at the University of Stuttgart. The research interest is ultrafast spectroscopy at and beyond the optical resolution limit. The group combines nonlinear optical methods such as pump-probe spectroscopy and higher harmonics generation with high-resolution optical microscopy to investigate ultrafast dynamics on the nanoscale. One focus is on single nanoobjects such as metal nanoparticles, semiconductor quantum dots or molecules. Traditional ultrafast spectroscopy averages over large ensembles of these systems, thereby removing all the details of the variation between individual objects. Only the spectroscopy of a single particle can yield the full picture of a nanoobject's ultrafast dynamics. We use for example single-particle pump-probe spectroscopy to investigate elastic properties at the nanoscale. A second focus is on nanostructured materials like metallic photonic crystals. The periodic arrangement of metallic structures leads to new optical properties of the combined medium. We make use of interactions between metal stripes or layers to, e.g., increase the lifetime of particle plasmons or produce ultrafast transmission changes. [17]

⬡ Optical parametric amplifier generating tunable femtosecond pulses for coherent spectroscopy.

Scientific Service Groups

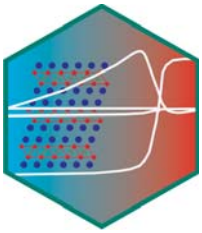

The CHEMICAL SERVICE GROUP (Kremer) develops techniques and maintains experimental facilities in order to perform physical measurements to support all experimental groups of the Institute with the characterization of electrical, thermal and magnetic properties of new compounds and samples. Our mission requires a great versatility of the supported experimental methods including the development and cultivation, e.g., of experimental techniques to perform measurements on chemically highly sensitive and reactive small samples under inert gas conditions. Presently available are two commercial SQUID magnetometers, home-built ac-susceptometers, dc- and ac-electrical resistivity setups and calorimeters in a broad range of temperature and magnetic fields. Materials currently under investigation are novel superconductors (rare earth carbides and carbide halides, intercalated graphite, magnesium diboride), new or unusual magnetoresistive materials (rare earth halides and hydride halides), low-dimensional and frustrated magnetic systems and systems with unusual magnetic ground states (spin-Peierls systems, frustrated quantum chain systems). [78,92]

⬡ $Y_2C_2X_2$ – A halide superconductor. The white solid lines symbolize the electrical resistivity, the heat capacity and the magnetic susceptibility proving $Y_2C_2I_2$ to be a superconductor with a T_c of 10 K.

The COMPUTER SERVICE GROUP (Burkhardt) runs the Institute's central mail, print, software, backup and web servers, as well as the ten servers providing department specific services. All servers use the Linux operating system. The central Fibre Channel based Storage Area Network (SAN) allows to add additional storage when needed without service interrupt. Backup remains based on Tivoli Storage Manager (TSM); currently the total backup data volume is about 40 TB. The Backup hardware has been modernized, the 10 years old tape robot has been replaced, increasing the total tape capacity to 112 TB mainly due to a ten fold increase of the capacity of a single LTO3 tape cartridge (now 400 GB). The servers were >99.99% online, this translates to total fileserver downtimes around 15 minutes in 2007 due to security and kernel updates.

In 2007 the group integrated about 110 new PCs into the network, bringing the estimated total number to well above 1000 PCs used as desktops and for data acquisition purposes. Of these about 70% run Windows and 30% run Linux. The IBM Bladecenter System was extended to 114 Intel/AMD blades (456 cores), making the x86/x86-64 based systems the new computational backbone for the Andersen, Bester and Metzner groups. Three rack mounted Linux clusters with a total of 208 Intel Xeon cores (IBM xSeries 335, x3550) provide additional cost effective computational resources for the Jansen, Maier and Metzner departments. Existing codes were ported by the group to the new set of compilers (Intel, Portland) and libraries (Intel mkl, gsl). The number of PowerBlades remained constant at 128 CPUs (258 cores). All machines are based on the SuSE Linux Enterprise Server operating system with the exception of the AIX based IBM p655 system for jobs with high memory requirements which was extended to 64 POWER4 CPUs using hardware from the former Gao group at the MPI-MF. The IBM SP3 was subsequently shut down after 9 years of service.

⬡ View inside the Tape library of the DV-FKF. Every night the data of 120 computers in the Institute is backed up. At the moment the total TSM backup and archive volume amounts to 40 Terabytes.

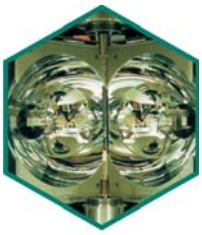

The CRYSTAL GROWTH SERVICE GROUP (Lin) applies, modifies and develops techniques, such as traveling solvent floating zone with infrared image furnace, Bridgman, top seeded solution growth and Czochralski methods to grow single crystals from the melt or solution. These range from isotopically pure semiconductors to fullerenes and transition metal oxides. Three floating zone furnaces, including Xenon lamps heating up to 3000°C, are fully operational. They are used predominantly to grow large single crystals of transition metal oxides for neutron and optical spectroscopy. Vapor transport methods are modified to grow crystals of II-VI and III-V compounds with defined isotopic components from low amounts of source materials. Accurate characterization is done with the aim of obtaining high-quality single crystals, for instance, superconductivity and magnetism performed using SQUID, crystal compositions determined by SEM/EDX, structure and phase identified by X-ray diffraction method, polling of twin domains, differential thermal and thermal gravimetric analysis. Thermal behavior of investigated compounds can be direct in situ observed under high temperature optical microscope. [36]

⬡ A view of the inside chamber of the four ellipsoidal infrared image (TSFZ) furnace.

Research within the HIGH PRESSURE SERVICE GROUP (Syassen) is concerned with the effects of hydrostatic pressure on structural, lattice dynamical, and electronic properties of crystalline solids and their high-pressure phases. Advantage is taken of recent developments in diamond anvil cell techniques, including progress in analytical methods that utilize synchrotron X-ray radiation (diffraction as well as inelastic scattering), synchrotron infrared radiation, and laboratory-based low-temperature optical spectroscopy. Subjects of interest range from improving the understanding of chemical bonding and phase formation at high densities to illuminating the interplay between subtle changes in crystal structure, electron delocalization, magnetism, and superconductivity in correlated electron systems of different dimensionality. In terms of materials, the interest in covalently bonded semiconductors and nanostructures continues, while the 'simple' alkali metals have attracted attention due to their surprisingly complex structural and electronic behavior at high density. The main focus, though, is on the physics of transition metal compounds with metal ions in high oxidation states, i.e., systems being located close to the insulator-metal borderline and undergoing pressure-driven Mott-like delocalization transitions. [70]

⬡ Schematic view of a diamond window high-pressure cell.

The CENTRAL INFORMATION SERVICE (Marx/Schier) for the institutes of the Chemical Physical Technical (CPT) Section of the Max Planck Society is located at the Max Planck Institute for Solid State Research in Stuttgart. The CPT Information Service is accessible for all scientists within the entire society and provides support in all demands of scientific information. The service has access to many commercial databases and patent files not included in the range of end user databases and should be contacted, if searches in the available databases are not sufficient. Professional searches in chemistry, materials science, and physics are performed in the various files offered by STN International. In particular, the files of the Chemical Abstracts Service in conjunction with the STN search system enable sophisticated searches regarding compounds, reactions, and spectra. New analyze tools allow establishing research field statistics.

Beside the databases, covering general disciplines like chemistry and physics, there are many databases for specific research fields like materials science, engineering, and environmental sciences. In addition, factual databases enable searching numerical data like chemical and physical properties of compounds and various national and international patent files are available. Furthermore, the service offers citation data, including citation statistics with respect to scientists or research institutes for the demands of research evaluation. Finally, the service offers help and training for searching end user databases like SciFinder, INSPEC, and Web of Science.

⬡ The archives of science are rapidly growing: One of the about 30 million substances registered in the compound file of the American Chemical Abstracts Service. Powerful databases and search systems have become indispensable tools in processing the actual information flood in science.

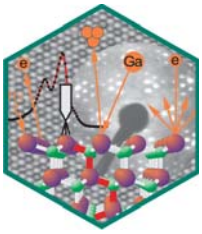

INTERFACE ANALYSIS SERVICE GROUP (Starke) investigates the atomic and electronic structure of solid-solid and gas-solid interfaces. Using electron spectroscopy techniques, quantitative low-energy electron diffraction, scanning probe microscopy and secondary ion mass spectrometry (SIMS), the atomic geometry and morphology as well as the chemical composition and bond coordination are determined for the sample surface and its immediate vicinity. Thin films and buried interfaces are accessible by sputtering techniques or sample cleavage methods. Experimental facilities available include a time-of-flight SIMS machine to quantify the chemical composition at the surface, within the film and at interfaces. Chemical and electronic properties are investigated in a multicomponent chamber containing high-resolution electron spectroscopy for chemical analysis. A scanning Auger microscope yields spectroscopic images with high lateral resolution. Sample morphology can be studied using an atomic force microscope and a white-light interferometer. The research activities of the group are directed towards growth and analysis of surfaces and ultrathin films of novel materials for semiconductor technology, e.g., wide bandgap semiconductors (SiC), metal silicides, as well as epitaxial metal films. Material growth, heterojunctions, metallization and ferromagnetic layers are investigated on an atomic level for a detailed understanding of the fundamental interactions involved in the growth process. In particular, graphene layers grown epitaxially on SiC surfaces are investigated. In addition, molecular adsorbates are studied on these surfaces as model systems for a variety of applications. [51]

⬡ Chemical composition, electronic structure and atomic geometry are investigated for complex compound systems such as 4H-SiC (bottom). Scanning probe techniques provide real-space images (background), electron diffraction yields accurate geometry data (right), photoelectron spectra are analyzed for chemical information (left).

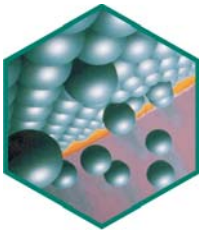

The subject in the MBE SERVICE GROUP (Dietsche/Schmidt) is the preparation and characterization of III/V and group IV semiconductor heterostructures. We apply molecular beam epitaxy (MBE) for the material systems AlGaAs/GaAs and InGaAs on GaAs substrates, and SiGe/Si on Si substrates. One interest is the preparation of low-dimensional nanostructures. Lateral confinement is achieved by island formation in epitaxial growth of strained heterostructures. To control the spatial position of self-assembled nanostructures we grow quantum dots on lithographically pattered substrates. Another subject is the formation of free-standing semiconductor nanotubes. The preparation is controlled by selective under-etching of strained epitaxial semiconductor bilayers. The other activity is the growth of heterostructures which are used to study electronic transport and optical properties by research groups inside and outside the Institute. One focus is the achievement of two-dimensional electron gases with extremely high mobility. This re-

quires a substantial reduction of the impurity levels compared to traditional MBE. Over the last few years we managed to approach the purity levels of the best systems in the world. Using samples of the MBE group it was possible to obtain the strongest evidence for exciton superfluidity in bilayers reported so far. [13]

⬡ Atoms impinge, diffuse and nucleate on the surface of a heated crystalline substrate under ultrahigh vacuum conditions. This process is called molecular beam epitaxy.

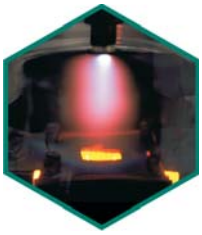

The TECHNOLOGY SERVICE GROUP (Habermeier) offers service work in the fields of thin film preparation, microlithography and fabrication of bonded contacts to semiconductors and ceramic materials. The experimental facilities include high-vacuum evaporation and sputtering (dc, rf and reactive) techniques. Additionally, pulsed laser deposition systems are installed to prepare thin films of materials with complex chemical composition such as high-temperature superconductors (HTS), perovskites with colossal magnetoresistance (CMR) and other related functional oxide ceramics. Dry etching techniques complement the spectrum of experimental techniques available. The research activities are closely related to the service tasks. Thin film deposition of doped Mott insulators such as HTS and CMR materials play a central role. The main focus of interest is the study of interface related phenomena in complex oxides such as epitaxial strain in functional ceramics, mesoscopic phase separation and electronic and magnetic interactions at HTS–CMR interfaces as well. This research activities is performed in close scientific cooperation with the departments Maier and Keimer. Additionally, the preparation and investigation of magnetic and superconducting oxide superlattices (manganites, ruthenates and cuprates) and their mutual electronic interaction as well as the study of special oxide heterostructures are designed for polarized spin injection, exchange bias effects and magnetic flux-line pinning phenomena are of central interest. [87]

⬡ Pulsed laser deposition has become a widespread technique for the fabrication of epitaxial thin films of multicomponent materials like doped lanthanum manganites and superconducting materials.

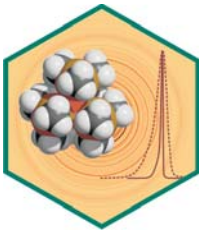

The X-RAY DIFFRACTION SERVICE GROUP (Dinnebier) provides X-ray diffraction measurements of single crystals and powders in the laboratory at room and low temperature. Research within the group is mainly concerned with the determination of crystal structures and microstructural properties (strain, domain size) of condensed matter from powder diffraction data. In addition, methodological development within this area is pursued. Special expertise in the field of solution and refinement of crystal structures from powder diffraction data can be provided. Scientific cooperation in the field of nonroutine structure determination (phase transitions, disorder, anisotropic peak broadening, etc.) from powders is offered. This includes the performance of experiments at synchrotron and neutron sources at ambient and non-ambient conditions. Materials currently under investigation include organometallic precursors, binary and ternary oxides, ionic conductors, electronic and magnetic materials, and rotator phases. [41]

⬡ Quasispherical molecule of tetrakistrimethylstannylsilane with underlying two-dimensional image plate powder diffraction pattern. The superimposed Bragg reflections demonstrate the difference in resolution between laboratory and synchrotron data.

Nanostructures

The design and fabrication of nanostructured materials with controlled electronic properties is an important field of research at the Institute. The first contribution in this section describes the fabrication of quantum dot arrays with perfectly tuned emission energies. It is shown that in the post-fabrication state the frequencies of single dots can still be tuned by in situ laser processing. Similarly the controlled design of optical transparency windows is possible with nanoscaled materials formed by sheets of materials with different dielectric properties as described in the following contribution. The ultrafast nonlinear transition dynamics and switching of such photonic crystals studied by the 'Ultrafast Nanooptics Group' is of interest for basic research and for applications, e.g., for optical telecommunication. Interfaces between different transition metal oxides, e.g., between a high-temperature superconductor and a colossal magnetoresistant manganite, as discussed in the third contribution, may give rise to devices with novel properties due to charge transfer and orbital reconstruction. Quantum dots can be considered as 'artificial atoms', i.e., their electronic structure is similar to that of an atom. As discussed in the next contribution quantum dot systems designed in a controlled way can be used to investigate fundamental physical processes like the role of Kondo correlations on electrical transport. The final article in this section goes a further step down from the nano to the atomic scale. In this case the distance of pairs of Co atoms on a Cu(100) surface is controlled and the magnetic interaction between the Co spins as function of their distance is determined with help of scanning tunneling spectroscopy.

Quantum dots with perfectly resonant emission energies

S. Kiravittaya, A. Rastelli*, L. Wang and O.G. Schmidt* (* also IFW Dresden)

The fabrication of nanoobjects with perfectly controlled properties is one of the biggest challenges in nanotechnology. Semiconductor quantum dots (QDs) are nanostructures, which confine charge carriers in all directions and behave to a large extent as artificial atoms. They could be employed as solid-state quantum emitters and possibly for quantum information processing. Self-assembled QDs are characterized by excellent structural properties, but their position on the substrate is random and the emission energies differ from one QD to another QD. While the former problem can be overcome by growing the QDs on patterned substrates [1], fabricating QDs with well-defined emission energies is still an open issue.

Here we first show, by micro-photoluminescence spectroscopy (μ-PL), that QDs treated by rapid thermal annealing are characterized by resolution limited sharp emission lines, indicating that high quality QDs can indeed be obtained by annealing even at high temperatures. We then use a focused laser beam both for characterization (at low power) and for post-fabrication processing (at high power) of QDs. We refer to the latter approach as an *in situ* process and show that by *in situ* laser processing we can engineer, within a broad range and resolution-limited accuracy, the emission of single QDs. This allows us to produce arrays of perfectly resonant QDs [2].

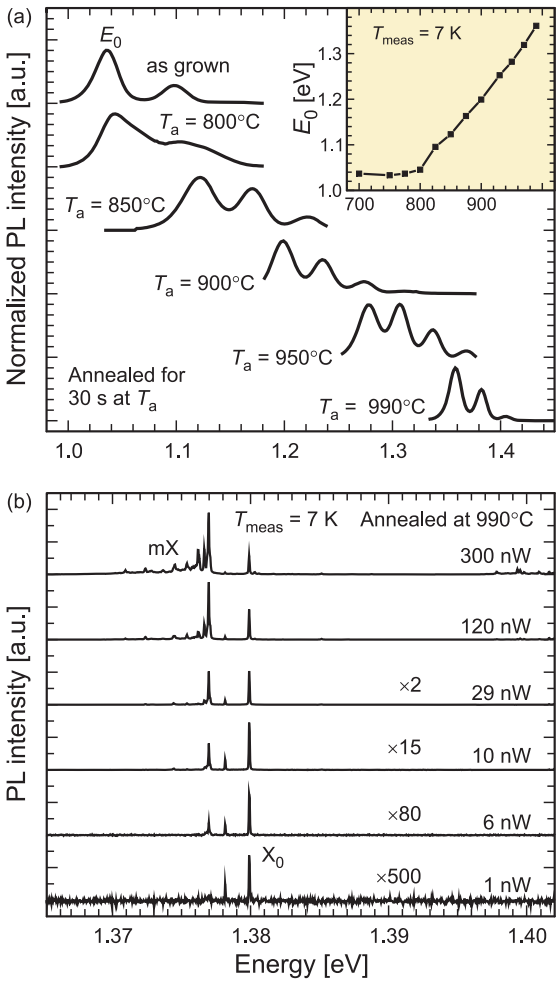

Figure 1: (a) Low temperature PL spectra of a sample with InAs/GaAs QDs treated for 30 s at the indicated annealing temperature T_a. E_0 indicates the ground state QD transition. The effect of the annealing on E_0 as a function of T_a is shown in the inset. (b) μ-PL spectra from a single QD contained in a sample annealed at 990°C as a function of excitation power (indicated on the right).

The samples studied here were fabricated by solid-source molecular beam epitaxy on GaAs(001) substrates. The following heterostructure was grown: 1 μm $Al_{0.7}Ga_{0.3}As$ sacrificial layer, 10 nm GaAs, 20 nm $Al_{0.3}Ga_{0.7}As$ cladding layer, 100 nm GaAs, 0.5 nm InAs QD layer, 100 nm GaAs, 20 nm $Al_{0.3}Ga_{0.7}As$, and 10 nm GaAs. For the InAs QD layer, the substrate rotation was stopped in order to have the inhomogeneity of the In rate across the sample. The QD density varies from about $4{\cdot}10^9$ cm^{-2} to zero moving from the wafer center towards the edge. This allows us to investigate the PL of QD ensemble as well as of single QD on the same sample.

Figure 1(a) illustrates the effect of annealing on the PL of the sample containing QDs. All spectra are normalized and vertically shifted for clarity. The top spectrum shows the emission of the as-grown sample. The peak labelled as E_0 originates from the ground state recombination of the QD ensemble. The peak at higher energy is attributed to excited state recombination. As expected, annealing at sufficiently high temperatures has the effect of blue-shifting the emission (see Fig. 1(a)). By increasing annealing temperature T_a, the ensemble emission can be controllably shifted, as shown in detail in the inset of Fig. 1(a), where the ground state QD peak position E_0, obtained at low excitation intensity, is plotted as a function of T_a. For $T_a < 800$°C there is a negligible change of E_0, while above 800°C E_0 increases. The emission blue-shift is accompanied by a monotonic decrease of the level separation between the excited states and E_0, indicating a decrease of the confinement. Both effects are due to thermally induced bulk In-Ga interdiffusion, which reduces the In content of the QDs and smoothes the confining potential.

The full-width-at-half-maximum of the E_0 peak first increases from 24 to 55 meV and then decreases monotonically down to 12 meV for the highest temperature used here (990°C). Even at such a high temperature, the PL data show the presence of excited states, indicating that the QDs preserve their three-dimensional carrier confinement nature. To confirm this statement we use μ-PL spectroscopy on a low-density area. Representative PL spectra of a single QD are shown in Fig. 1(b). At low excitation power the spectrum is dominated by a resolution-limited sharp line, labelled as X_0, which we attribute to neutral exciton recombination. When the power is increased other lines appear (generally labelled as multiexcitons, mX). This behavior is typical for QDs and suggests that the rapid thermal annealing does not degrade the optical properties of the QDs.

In spite of a substantial reduction of the inhomogeneous broadening of the QD ensemble, annealing produces a simultaneous shift of all the QDs in the processed sample. It is therefore evident that the only way to obtain QDs with identical emission energies is by processing each single QD independently. This can be done by means of a local heat source. Besides the lack of locality, it has also the disadvantage of being an *ex situ* method, in the sense that the processing is performed with an equipment independent from that used for the characterization. In practice, the samples have to be cooled to cryogenic temperature to check the result of the annealing. This would render it extremely difficult to fine tune the emission energy of a single QD to a given value. Both issues can be solved by using the laser of a μ-PL setup as local heat source.

In order to be able to heat a QD structure from cryogenic to elevated temperatures with moderate laser powers, it is necessary to reduce the thermal contact with the substrate. This is easily achieved by partially underetching the AlGaAs layer as shown in Fig. 2(a) for a microdisk structure standing on a thin post. The 200 nm protective SiO_x layer deposited after fabrication is also indicated. Figure 2(b) shows the evolution of the PL from a microdisk while the laser power is ramped up continuously within 100 s. At low power the microdisk temperature is the same as the temperature of the substrate (5 K).

With increasing power the emission of GaAs matrix is observed to red-shift (see dashed line). The same occurs for the disk optical modes (sharp lines), although the amount of the shift is much smaller. This behavior indicates a progressive heating of the microdisk. The GaAs substrate below the disk remains cold, as indicated by the vertical straight features in the PL intensity map. The red-shift of the GaAs and that of the modes are due mainly to bandgap shrinkage and increase of the effective refractive index of the material with increasing temperature, respectively. By knowing the temperature dependence of the optical properties of GaAs we can estimate the temperature reached by the structure at a certain laser power. The extracted temperature values are shown on the right axis of Fig. 2(b). These values indicate that it is possible to heat a disk from cryogenic to elevated temperatures with a few mW of laser power.

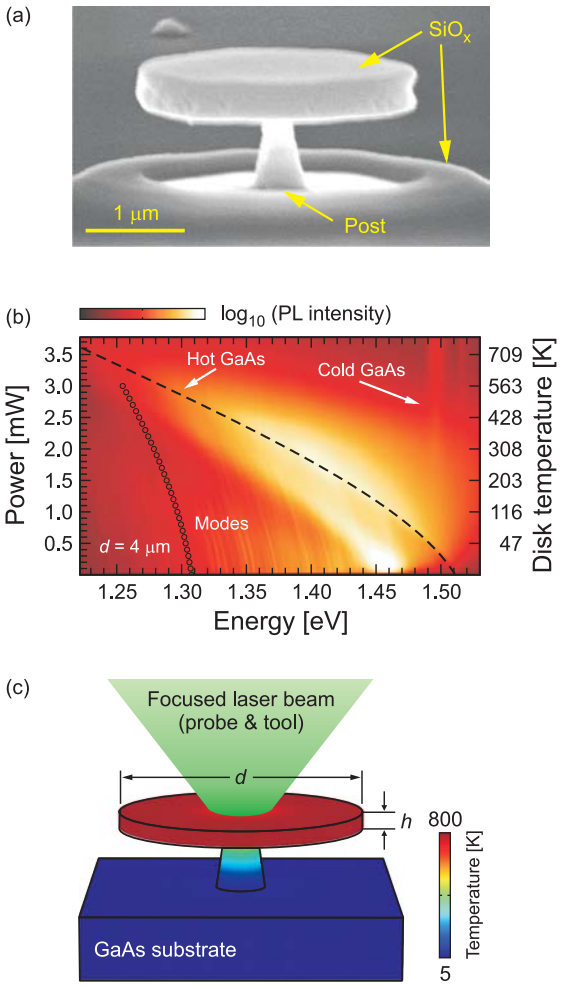

Figure 2: (a) Scanning electron microscopy image of a SiO_x coated GaAs microdisk containing InAs QDs. (b) PL intensity map as a function of energy and laser power. (c) Calculated temperature profile for a disk similar to that used for the measurement shown in (b).

To get a deeper insight in the laser-heating process, we model the microdisk as a disk of GaAs placed on top of a post with truncated cone shape. We assume the laser to have a Gaussian beam profile with full-width-at-half-

maximum of 1.5 μm. The power absorbed in the disk represents the heat source while the substrate is the thermal bath kept at cryogenic temperatures (5 K). The temperature profile calculated by solving the heat conduction equation by means of a finite element method is graphically displayed in Fig. 2(c) for a laser power of 4 mW. With this geometry the disk temperature is rather homogeneous across the disk area, with a slight drop on top of the post. This post is the channel through which the heat flows towards the substrate. Thus, its size critically affects the value of temperature reachable for a given laser power. This is confirmed by the experimental observation that disks with relatively large posts require several tens of mW to be appreciably heated.

Since the structure is heated inside the cryostat, it is sufficient to reduce the laser power back to a few ten nW to measure the effect of the thermal treatment. This allows us to controllably blue-shift the emission of selected QDs by applying different *in situ* heating steps followed by the measurement of the resulting spectrum.

Figure 3(a) demonstrates that *in situ* laser processing can indeed be used to bring into resonance spatially separated QDs. For this experiment we consider single QDs located in different square-shaped mesa structures and we take the positively charged trion X_T^+ of a QD, labelled as QDT, as our target. By laser heating for 7 s at increasingly high powers (up to a few mW) we gradually blue-shift the emission of two QDs, QD1 and QD2, until their X^+ transitions, X_1^+ and X_2^+, reach the same energy as X_T^+. Figure 3(b) shows a summary of the X_1^+ and X_2^+ positions as a function of processing step.

We can illustrate the mechanism leading to the blue-shift by assuming that the different QDs have the same homogeneous composition, but different sizes prior to processing. The interdiffusion occurring during the heat treatment smoothes the interfaces between QD and surrounding barrier, leading to shallower confinement potentials for electrons and holes (the insets of Fig. 3(b)). In reality different QDs are characterized by different atomic arrangements, since all the processes taking place during InAs deposition and subsequent GaAs-overgrowth can be described by statistics. This renders the structure, and hence the optical spectra of each QD unique (note, e.g., the X_0–X^+ separation in the 3 QDs shown in Fig. 3(a) prior to laser processing).

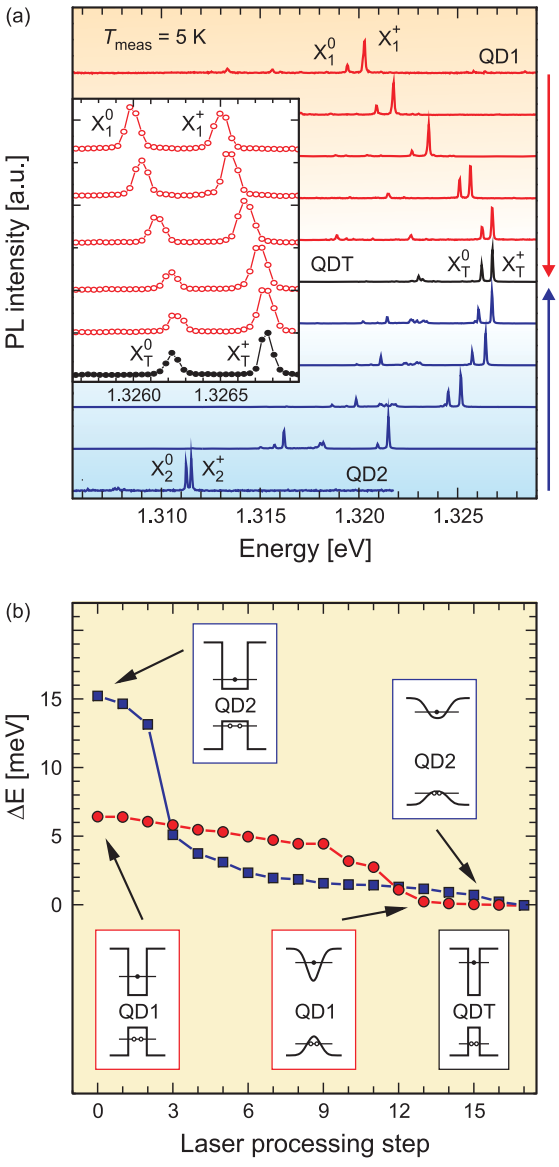

Figure 3: (a) PL spectra illustrating the *in situ* tuning of the positive trion X^+ emission of three spatially separated QDs into resonance. Inset: PL spectra showing the fine-tuning of the QD1 emission. (b) Shifts of the QDs shown in (a) as a function of heating step. Insets: Schematics of the band structure of the QDs prior to and after the laser processing.

In conclusion, we have demonstrated that *in situ* laser processing can be effectively employed as a post-fabrication tool to engineer the properties of single QDs. By applying this process to positioned QDs [1], arrays of ordered and perfectly resonant QDs may possibly be obtained. Since practically all material combinations are sensitive to heat treatment, the approach is obviously not limited to the system discussed here.

[1] *O.G. Schmidt (Editor).* Lateral Alignment of Epitaxial Quantum Dots. Springer Verlag, Berlin (2007).

[2] *Rastelli, A., A. Ulhaq, S. Kiravittaya, L. Wang, A. Zrenner and O.G. Schmidt.* Applied Physics Letters **90**, 073120 (2007).

Ultrafast nonlinear transmission dynamics of metal-dielectric photonic crystals

T. Höner zu Siederdissen, T. Ergin, J. Kuhl and M. Lippitz; H. Giessen (Universität Stuttgart)

One-dimensional metal-dielectric photonic crystals are stacks of periodically spaced thin metal films (a few nanometers thick) separated by a dielectric material. Such structures feature a transparency window in the visible region [1], whereas a single metal layer with the same total thickness constitutes a mirror with a high reflectivity. This unique feature allows exploitation of the nonlinear *transmissive* properties of metals. Recent experiments based on time-integrated *z*-scan measurements [2] and numerical calculations [3] suggest that the transmission window can be strongly suppressed by intense pulsed laser pumping. This makes such stacked metal-dielectric structures interesting for the development of ultrafast all-optical devices. A highly demanded application is an all-optical switch which could be transferred from a transmitting to a reflecting state with sub-picosecond response and recovery times. Such an optical packet switching device is needed for high-speed fibre-based optical telecommunications. The research is aimed at investigating whether the proposed effects in one-dimensional metal-dielectric photonic crystals are suitable for such applications.

We present, to our knowledge, the first time-resolved studies of metal-dielectric photonic crystals. Our samples consist of 5 layer pairs (on a glass substrate) of Ag and SiO_2 with thicknesses of 16 nm and 250 nm, respectively. Linear transmission spectra show a peak with 45% transmission at a wavelength of 830 nm (Fig. 4).

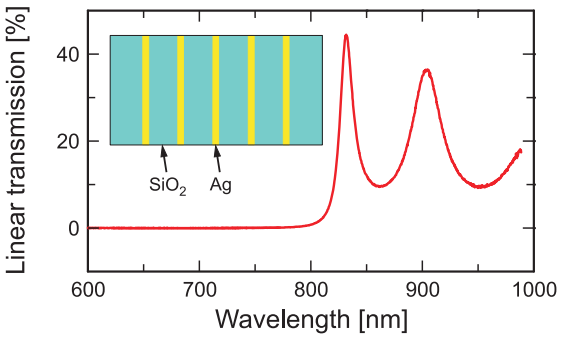

Figure 4: Linear transmission of a Bragg stack of alternating metal and dielectric layers. A progression of transmission peaks is found, starting at around 830 nm with 45% transmission. Inset: Layout of the structure on top of a glass substrate. SiO_2 thickness: 250 nm; Ag thickness: 16 nm.

We used pump-probe spectroscopy (Fig. 5) with sub-picosecond time resolution to experimentally investigate the ultrafast dynamics of the switching process. A Titanium:sapphire laser delivers 100 fs pulses at a repetition rate of 76 MHz and a wavelength close to the maximum transmission peak. The laser beam is split into two parts: Pump and probe, which are delayed with respect to each other by mechanically increasing the length of one beam path.

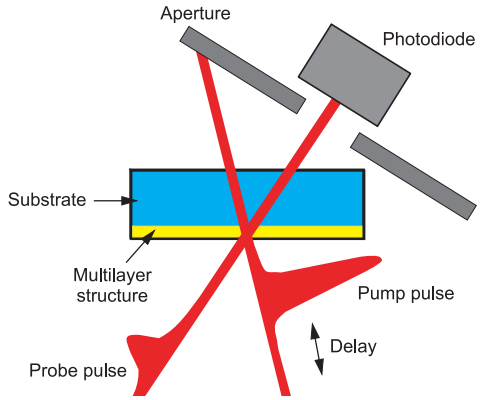

Figure 5: Pump-probe spectroscopy scheme: The transmission of the probe beam is measured with a photodiode as a function of the delay with respect to a much stronger pump beam.

Both beams are focused onto one spot on the sample surface. The transmitted probe beam is detected by a photo diode. The pump beam, whose intensity is about three orders of magnitude higher, is blocked by an aperture between the sample and the diode. This method allows a time-resolved measurement of the pump-induced transmission changes of the structure.

On a picosecond timescale, our results show (Fig. 6(a)) a fast decrease of the relative transmission $\Delta T/T$ (superimposed with a constant background signal) and an initial partial recovery with a time constant of about 500 fs. The magnitude of the transmission change is about $5{\cdot}10^{-5}$ at the highest pump intensity. On the millisecond timescale (Fig. 6(b)) a much larger relative transmission change is found, comparable to that of time-integrated z-scan measurements [2]. Two different effects seem to dominate on the different timescales. The absorbed pump pulse generates a hot electron gas which slightly modifies the dielectric properties of the silver layer, but cools down on a sub-picosecond timescale and produces only a weak transmission change. The increased lattice temperature then changes the dielectric material constants of both the metal and the dielectric. This detunes the optical cavities that are formed by the periodic stack of silver layers. The hot lattice gives a much stronger effect, but is limited in its decay time by heat conduction, which is slow compared to the pulse repetition rate of the laser. On a second time scale, this lattice temperature induced transmission change becomes extremely large, since the lattice temperature rise is accumulated over millions of intense laser excitation pulses. Numerical simulations that fully describe the coupling between the electron and lattice systems and the influence on the transmitted field are under way to confirm this interpretation.

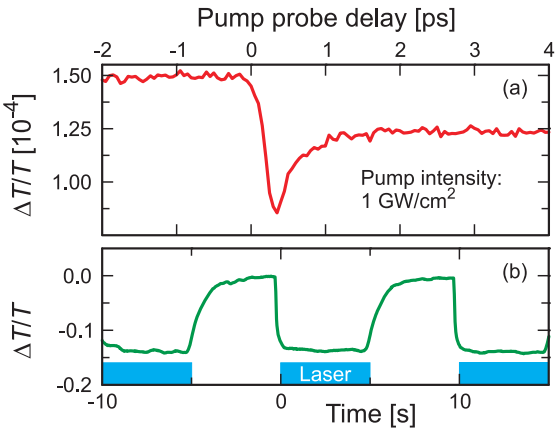

Figure 6: We measured the pump-induced change of the probe transmission (ΔT) normalized to the unperturbed case (T) on two timescales: (a) on the picosecond timescale the pump-pulse causes a fast decrease in the transmission followed by a slower recovery with an amplitude of about $5{\cdot}10^{-5}$ (b) on the millisecond timescale, the transmission change is much stronger (10^{-1}), but also much slower (≈ 700 ms).

In conclusion, we measured sub-picosecond transmission dynamics in metal-dielectric layered photonic crystals which might be used as all-optical switching devices. In the present stage of the experiments the sub-picosecond effect seems to be too small to be useful. Previously published strong effects, on the other hand, seem to be connected to thermal expansion and cooling by heat conduction, which is too slow for most applications.

[1] *Bloemer, N.J. and M. Scalora.* Applied Physics Letters **72**, 1676–1678 (1998).

[2] *Lepeshkin, N.N., A. Schweinsberg, G. Piredda, R.S. Bennink and R.W. Boyd.* Physical Review Letters **93**, 123902 (2004).

[3] *Scalora, M., N. Mattiucci, G. D'Aguanno, M.C. Larciprete and M.J. Bloemer.* Physical Review E **73**, 016603 (2006).

Orbital reconstruction and covalent bonding at an oxide interface

J. Chakhalian, H.-U. Habermeier, G. Cristiani, G. Khaliullin and B. Keimer;
J.W. Freeland and M. van Veenendaal (Argonne National Laboratory, USA)

Modern microelectronics relies to a large degree on the properties of interfaces between two different semiconductors. In a transistor, for instance, the electrical conductivity at the interface can be controlled very effectively by an external voltage. In order to optimize the operation of transistors and other microelectronic devices, knowledge of the electronic states near semiconductor interfaces has been accumulated over the past half-century. We have taken initial steps towards an understanding of the behavior of electrons at the interface between two complex materials exhibiting properties not known in ordinary semiconductors: A ferromagnetic manganese oxide and a superconducting copper oxide. Understanding and manipulating these properties at interfaces may open a path towards a new generation of electronic devices.

The large variety of phases (with often radically different physical properties) in transition metal oxides is due to the delicate sensitivity of the charge transfer and magnetic interaction between metal ions to the occupation of d-orbitals. Which linear combination of the five possible *d*-orbitals is occupied on a given transition metal site depends, in turn, on parameters such as electron density, ligand positions, magnetic order, and chemical bonding, which are generally different at the interface than in the bulk. Despite its pivotal role in determining the phase behavior and physical properties of oxides, almost no experimental information is available about the occupation of orbitals at oxide interfaces, and theoretical work has thus far hardly addressed this issue. We report the results of soft X-ray absorption (XAS) and soft X-ray linear dichroism (XLD) experiments on heterostructures of copper and manganese oxides tailored to probe the electronic structure and orbital occupation at the interface [1]. The cuprate-manganate interface is well-suited as a model system for this purpose, because nearly strain-free, atomically sharp heterostructures can be synthesized, and because the electronic properties of both materials have been studied extensively in the bulk.

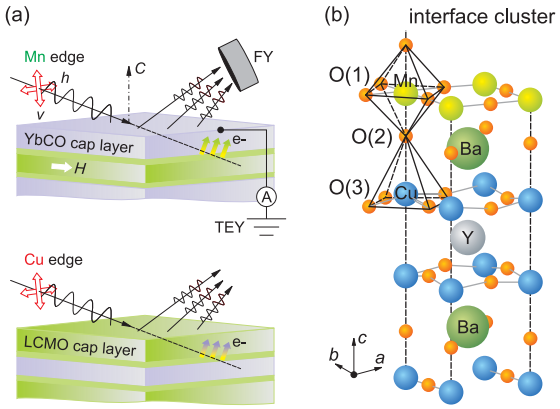

Figure 7: (a) Schematic of the experimental setup used to obtain the XAS and XLD data in TEY and FY modes. Data sensitive to interfacial Cu (Mn) atoms were taken in TEY mode with photon energies near the Cu (Mn) L-absorption edge, on samples with LCMO (YBCO) capping layers. (b) Atomic positions near the LCMO-YBCO interface. The $MnCuO_{10}$ cluster used for the exact-diagonalization calculations is highlighted.

The experiments were performed on epitaxial trilayers and superlattices of the high-temperature superconductor $(Y,Ca)Ba_2Cu_3O_7$ (YBCO) in *c*-axis orientation, combined with ferromagnetic metallic $La_{1-x}Ca_xMnO_3$ (LCMO) at a doping level $x = 1/3$. In order to discriminate the electronic structure at the interface from surface and bulk contributions, we have performed a systematic series of experiments on heterostructures with different capping layers, taking advantage of the element-specificity and shallow probing depth of resonant XAS and XLD in the total-electron-yield (TEY) mode (Fig. 7). For instance, the occupation of Cu *d*-orbitals on the YBCO side of the in-

terface was studied on heterostructures with LCMO capping layers, so that no surface Cu is present. If the photon energy is tuned to the Cu L-absorption edge, the capping layer does not influence the detected signal apart from an overall attenuation factor. Due to the low electron escape depth (a few nm), CuO_2 layers immediately adjacent to the first interface dominate the TEY signal; contributions from deeper layers are exponentially reduced. The converse procedure was used to probe the electronic structure of MnO_2 layers on the LCMO side of the interface. Control experiments in the bulk-sensitive fluorescence-yield (FY) mode were simultaneously carried out in both cases.

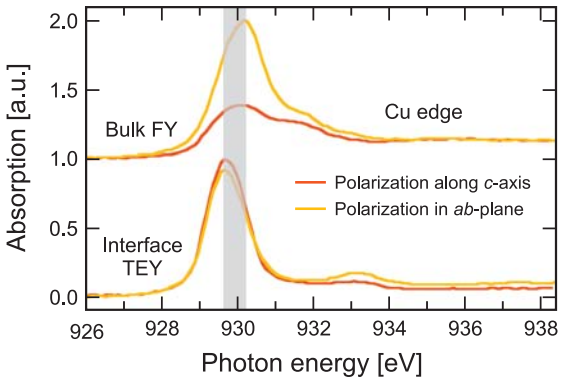

Figure 8: Normalized X-ray absorption spectra at the Cu L_3-absorption edge, taken in bulk-sensitive (FY, upper panel) and interface-sensitive (TEY, lower panel) detection modes with varying photon polarization.

Figure 8 shows normalized absorption spectra near the Cu L_3-edge in bulk- and interface-sensitive modes. The bulk-sensitive FY data are in excellent agreement with prior XAS data at the Cu L-edge of nearly optimally doped YBCO. The lineshape of the main absorption peak is a signature of the 'Zhang-Rice singlet', a bound state of charge carriers on oxygen and copper sites that keeps the Cu plane site in the nominal valence state 2+ as the hole density in the CuO_2 sheets is tuned by doping. The polarization dependence of the FY signal also contains important information about the electronic structure near the Fermi level of YBCO. In particular, the absorption for photon polarization parallel to the CuO_2 sheets greatly exceeds that for polarization along the *c*-axis. This implies that holes in the conduction band of YBCO predominantly occupy the planar Cu x^2–y^2 orbital, which hybridizes strongly with oxygen *p*-orbitals in the CuO_2 layers. Similar observations have been made in all other high-temperature superconductors investigated thus far, and together they have become one of the basic tenets of our current understanding of this class of materials.

The interface-sensitive data shown in Fig. 8 are strikingly different. One first notices that the interfacial absorption peak is shifted to lower energy with respect to the bulk by $\approx$0.4 eV, indicating a reduction of the Cu valence by $\approx 0.2e$ per copper ion near the interface. This shows that charge is transferred across the interface and that a charged double-layer is formed, as generally expected for heterostructures of materials with different work functions. Remarkably, however, numerous XAS experiments on YBCO and other bulk hole-doped high-temperature superconductors have shown that the position of the Cu L-absorption peak is independent of doping. This has been attributed to the Zhang-Rice singlet state, as a consequence of which the doped holes have predominantly oxygen character. The observed shift of the L-absorption peak in our interface-sensitive experiment thus cannot be attributed to a readjustment of the hole density alone and indicates a profound modification of the electronic structure of the CuO_2 layer adjacent to the interface.

In order to uncover the origin of the unexpected shift of the absorption peak and to obtain further information about the electronic states at the interface, we have varied the photon polarization in the interface-sensitive detection mode (Fig. 8). In marked contrast to the bulk-sensitive data, the strengths of the absorption signals for polarization perpendicular and parallel to the layers are almost equal.

This is a manifestation of an 'orbital reconstruction'. Whereas the holes are constrained to the Cu x^2–y^2 orbital in the bulk, at least some of them occupy the $3z^2$–r^2 orbital (which is completely occupied and electronically inert in the bulk) at the interface.

In principle, two distinct physical mechanisms could lead to such an orbital reconstruction. First, it is possible that the different crystal field environment of Cu ions at the interface could raise the energy of the $3z^2$–r^2 orbital above that of the x^2–y^2 orbital. However, this scenario is highly unlikely because of the large energy difference between $3z^2$–r^2 and x^2–y^2 derived bands in bulk YBCO. A reversal of this hierarchy would require a substantially shorter distance between the copper and apical oxygen ions (O(2) in Fig. 7(b)) compared to the in-plane Cu–O bond length, which is unrealistic. The second scenario is based on the observation that the Cu $3z^2$–r^2 orbital points directly towards the interface and can hybridize effectively with the Mn z^2–r^2 orbital via the apical oxygen ion, generating a covalent chemical bond bridging the interface. In this scenario, covalency results in the formation of extended 'molecular orbitals' consisting of atomic Cu and Mn $3z^2$–r^2 orbitals with an admixture of the p_z orbitals on the apical oxygen. With the aid of exact diagonalization calculations on a small cluster (Fig. 7(b)), we have confirmed that this scenario is indeed realistic.

In summary, our experiments show that the electronic structure of the CuO_2 layer, is modified by covalent bonds across the interface. These results suggest that the orbital rearrangement and strong hybridization are at least partially responsible for the unusual magnetic behavior previously observed at cuprate-manganate interfaces [2]. Further, the valence electrons of a large variety of transitions metal oxides whose properties in heterojunctions has been extensively investigated, reside in nearly degenerate *d*-orbitals and are hence subject to hybridization at interfaces. If this hybridization can be manipulated in a controlled fashion, it is conceivable that dense two-dimensional electron systems with controlled interactions and properties qualitatively beyond those attainable in semiconductor heterostructures can be created.

[1] *Chakhalian, J., J.W. Freeland, H.-U. Habermeier, G. Cristiani, G. Khaliullin, M. van Veenendaal and B. Keimer.* Science **318**, 1114–1117 (2007).

[2] *Chakhalian, J., J.W. Freeland, G. Srajer, J. Strempfer, G. Khaliullin, J.C. Cezar, T. Charlton, R. Dalgliesh, C. Bernhard, G. Cristiani, H.-U. Habermeier and B. Keimer.* Nature Physics **2**, 244–248 (2006).

Two quantum dot systems in lateral arrangement with strong electrostatic interaction: Tool for studying Kondo correlations in electrical transport

J. Weis, A. Hübel, K. Held and K. v. Klitzing

Electrons confined in a quantum dot possess a discrete single-particle energy spectrum. Due to this property, quantum dots are also denoted as 'artificial atoms'. Weakly coupled by tunnel barriers to a source and a drain lead, electrical transport through a quantum dot is dominated by the repulsive electron-electron interaction on the quantum dot site. Such a quantum dot system behaves as a single-electron transistor: By increasing the voltage applied to an adjacent gate electrode, the electron number on the quantum dot site is increased one by one, i.e., under a small source-drain bias voltage, the electrical conductance is repeatedly modulated between single-electron tunneling and Coulomb blockade regime ('Coulomb blockade oscillations').

In 1998, it was experimentally proven that, under certain conditions, such a quantum dot system shows Kondo physics [1] as it was already predicted in 1988 by mapping a single quantum dot system on the Anderson impurity model [2]: The presence of a spin-degeneracy on the quantum dot site induces at low temperature correlated electron tunneling between the quantum dot and the leads, forming overall a spin-singlet state. A highly conductive channel of transport is opened between the leads via the quantum dot, which even reaches the conductance $2e^2/h$ in the case of symmetric tunnel couplings to the leads – the value also found for a spin-degenerate one-dimensional channel. Increasing the temperature breaks the correlations, the Kondo effect is destroyed, and the Coulomb blockade effect is recovered.

The Anderson impurity model describes a spin-degenerate energy level at an impurity or a quantum dot site which is coupled through tunneling to a Fermi sea containing electrons of both spin orientations. In other words, it describes two separate electron subsystems labeled by a two-valued index which is usually identified with the spin quantum number (Fig. 9(a)). The two spin electron systems interact only on the impurity site through Coulomb interaction which suppresses double occupancies of the impurity.

In 2001, we pointed out that two electrostatically coupled quantum dots with separate leads (Fig. 9(b)) reflect a pseudo-spin representation of the Anderson impurity model [3]: This mapping is valid if (1) the quantum dot systems are energetically degenerated, i.e., occupying either dot costs the same energy, (2) the ground state of each quantum dot is not degenerate and excited states are energetically well separated. In case of a spin degeneracy in one or both quantum dot systems, spin and electrostatic (orbital) Kondo effect interplay.

Where do we expect to see these Kondo correlations? Two quantum dot systems with electrostatic interaction have a characteristic honeycomb-like charge stability diagram as a function of two gate voltages that shift the electrostatic potential of the quantum dots differently (see Fig. 9(c)).

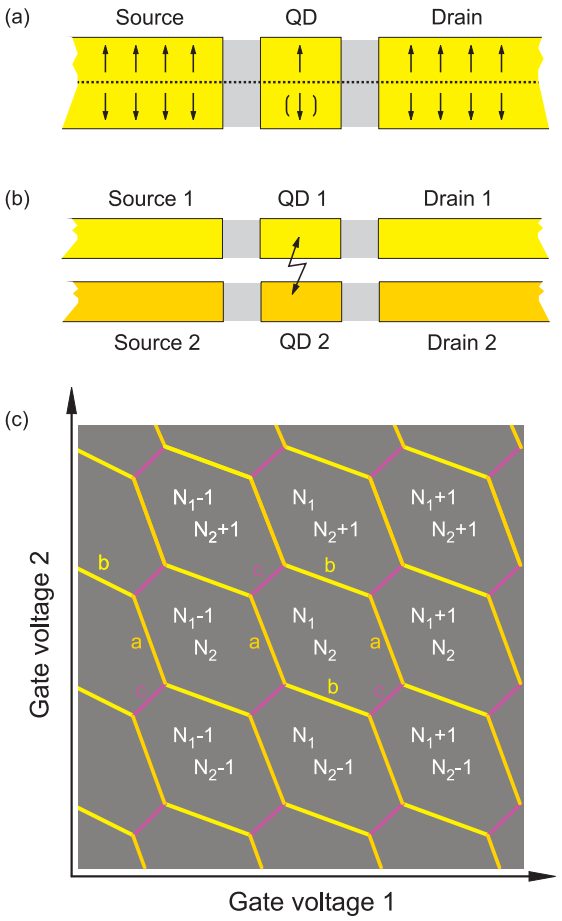

Figure 9: Possible realizations of the Anderson impurity model: (a) Single quantum dot system with spin-degeneracy, or (b) two electrostatically coupled quantum dot systems without spin-degeneracy. (c) Charge stability diagram vs. two gate voltages for arrangement (b). N_1 and N_2 denotes the number of electrons in the respective dot.

Along borderlines, labeled by **a** and **b**, where the electron number in one quantum dot changes by one whereas the electron number in the other remains unchanged, single-electron tunneling through the respective quantum dot is possible. Along borderlines, labeled by **c**, where the electron number in one dot is increased while in the other dot decreased, single-electron tunneling is not possible. However correlated electron tunneling is allowed switching between the two adjacent charge configurations.

Such borderlines **c** are only present if electrostatic interaction between the dots exists, otherwise the triple points at the ends of the borderline **c** merge. The borderlines **c** become longer with stronger interaction. Here we state the existence of a Kondo correlated state at low temperature leading to high conductance through both quantum dots.

To prove the presence of Kondo correlations in two electrostatically coupled quantum dot systems, we have investigated extensively two vertically stacked quantum dot systems realized in a $GaAs/Al_xGa_{1-x}As$ heterostructure ($x = 0.33$) containing two quantum wells with a two-dimensional electron system (2DES) in each well, separated by an insulating 40 nm thick $Al_xGa_{1-x}As$ barrier [4]. We obtained an interdot capacitance of about half the total capacitance C_Σ of a single quantum dot, i.e., the interaction energy is half the single-electron charging energy e^2/C_Σ of a single quantum dot. The electrical characterization measurements indeed indicate the existence of the Kondo correlation [4], including the expected logarithmic decay of the conductance on the **c**-line with temperature.

However, in the parameter regime of interest, we lack the independent control of the four tunnel barriers in the structure: One quantum dot was coupled to its source and drain whereas the second was only connected to its source, i.e., the electrical transport through only one quantum dot system was measurable. Therefore, the second dot could not be fully characterized, especially the strength of the tunnel coupling to the remaining lead was unknown.

To overcome the conceptional lack of in situ tunability in our vertically stacked arrangement – three voltage parameters for four tunnel barriers, we have now realized two quantum dot systems with strong capacitive interdot coupling in a *lateral* arrangement in a two-dimensional electron system buried 50 nm below the surface of a $GaAs/Al_{1-x}Ga_xAs$ heterostructure ($x = 0.33$). Strong electrostatic interaction between the dots is not trivially obtained in this geometry. This has been achieved by using a floating metal electrode covering both quantum dots.

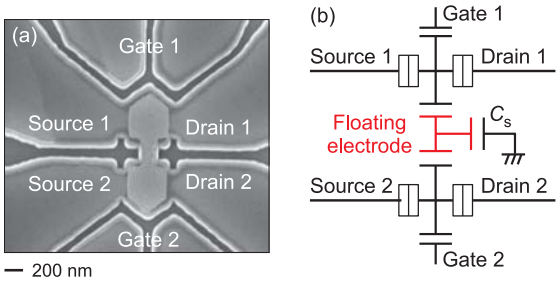

Figure 10: (a) Scanning electron microscope image of the etched heterostructure surface. The two-dimensional electron system is divided into different regions acting as quantum dots, leads and gates. A metal electrodes covers both quantum dot regions. (b) Capacitance circuit describing the arrangement. The stray capacitance C_S of the floating metal electrode has to be diminished.

The technique was already used by another group where the quantum dots were defined by electrostatic depletion via split-gates on the heterostructure surface [5], however with few success. In our approach, we defined our quantum dot systems by etching into the heterostructure, dividing the two-dimensional electron system into regions acting as quantum dots, leads and gates (Fig. 10(a)). In this way we could suppress capacitive coupling of the floating gate to gate electrodes in the surrounding, strengthening the capacitive interdot coupling (Fig. 10(b)). Also the shape of the floating electrode has been optimized to minimize the capacitive coupling to the leads [6]. Finally, in the weak tunnel coupling regime, a ratio of 0.35 between interdot capacitance and total capacitance of a single dot has been achieved in our new structure – less than in the vertically stacked arrangement (up to 0.5), however significant more than in previous lateral arrangements (< 0.2).

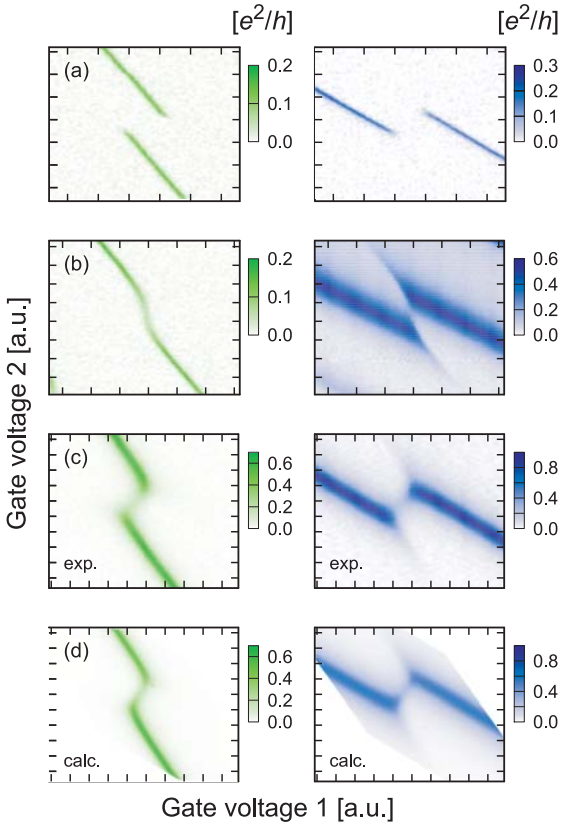

Figure 11: The conductance of quantum dot 1 (left) and 2 (right) as a function of two gate voltages measured around a ***c***-line of the charge stability diagram. From (a) to (b), the tunnel couplings to the leads of quantum dot 2 were increased. Between (a) and (c), the tunnel coupling of both quantum dots were simultaneously enhanced. (d) NRG calculation for case (c).

In Fig. 11 the conductances through the two quantum dots in a region around a **c**-line of the charge stability diagram are shown. The measurements were performed in a ^{3}He–^{4}He dilution refrigerator at base temperature of $T = 25$ mK. From Fig. 11(a) to (b), only the tunnel couplings to the leads of quantum dot 2 were increased, whereas between Fig. 11(a) and (c), the tunnel couplings of both quantum dots were simultaneously enhanced. Striking is that for weak tunnel coupling, no conductance is visible along the **c**-line, whereas with increasing the tunnel coupling, conductance appears.

This is expected since with increasing the tunnel coupling, correlated tunneling is enhanced. However, the position of the conductance peak does not follow exactly the **c**-line extracted from the observed single-electron tunneling peaks in Fig. 11(a). For the situation of different tunnel coupling of both dots (Fig. 11(b)), we could find an analytical expression for describing the position of conductance of quantum dot 1 by simply assuming that the strong tunnel coupled quantum dot 2 is only partially charged with the charge calculated by integrating over the part of a life-time broadened (= Lorentzian-shaped) energy level lying below the Fermi level of the leads. As the weakly tunnel coupled quantum dot 1 switches between well quantized charge states, the broadened energy level of dot 2 is shifted in energy between two values given by the electrostatic interdot coupling and the applied voltages. Having expressions for the total electrostatic energy of both situations, the gate voltage position of electrostatic degeneracy for switching the charge state of quantum dot 1 by an electron charge is found. It fits – except for a small offset – to the position for conductance in quantum dot 1 found in the experiment.

From these considerations for Fig. 11(b), it seems that simple single-electron tunneling happens through quantum dot 1 while charge-polarizing quantum dot 2. However the conductance heights and the temperature dependencies are different in the charge stability diagram at the **a**- and the **c**-line. For same tunnel coupling of both quantum dots (Fig. 11(c)), the picture of above does not hold. In any case, calculating the conductances through the dots is not that simple. This was done by using a numerical renormalization group (NRG) method, allowing for a numerical exact solution of the Anderson impurity model.

Using the parameters extracted from the experimental data in the regime of single electron tunneling of the respective quantum dot and the geometry of the honeycomb pattern, the observed conductance behavior of the electrostatically coupled quantum dot system could nicely be reproduced (an example is shown in Fig. 11(d)).

The comparison yields that the Kondo temperature of the system is below our working temperature, i.e., only the onset of the Kondo correlated state is visible in the experiment. Being limited by the base temperature of a ^{3}He–^{4}He dilution refrigerator, the relevant energies, especially the single-electron charging energies and the interaction energy between the quantum dots have to be enhanced, while keeping the tunability of the tunnel barriers. It requires mainly a reduction of the dot/lead capacitances. Whether underetching of the heterostructure in the tunnel barrier regions helps to improve remains to be clarified.

[1] *Reviewed by L.P. Kouwenhoven and L.I. Glazman.* Revival of the Kondo effect. Physics World, January, 33 (2001).

[2] *Anderson, P.W.* Physical Review **124**, 41–53 (1961).

[3] *Wilhelm, U., J. Schmid, J. Weis and K. v. Klitzing.* Physica E **9**, 625–630 (2001).

[4] *Wilhelm, U., J. Schmid, J. Weis and K. v. Klitzing.* Physica E **14**, 385–390 (2002).

[5] *Chan, I., R. Westervelt, K. Maranowski and A. Gossard.* Applied Physics Letters **80**, 1818–1820 (2002).

[6] *Hübel A., J. Weis, W. Dietsche and K. v. Klitzing.* Applied Physics Letters **91**, 102101 (2007).

Exchange interaction between single magnetic adatoms

P. Wahl, L. Diekhöner, M.A. Schneider and K. Kern; P. Simon (Université Joseph Fourier and CNRS, France); V.S. Stepanyuk and P. Bruno (MPI für Mikrostrukturphysik, Weinberg)

It is a vision of information technology to store data in the smallest available units – single atoms – thus enabling the development of novel mass storage devices with huge capacities but compact dimensions. At the same time this vision poses the physical limit on the information density of magnetic recording media. Both, for a realization of such a visionary device as well as to explore the limits of conventional mass storage media, it is crucial to understand the mutual interaction and dynamics of individual spins. This interaction can be due to direct coupling or indirect coupling mediated via a supporting substrate or host. Depending on the strength and sign of the exchange interaction, a nanostructure can be driven into ferromagnetic or antiferromagnetic behavior. However, until recently it was impossible to measure experimentally the magnetic interaction between individual atoms. We have exploited the Kondo effect as a local probe to determine the exchange interaction between individual cobalt adatoms on a metallic substrate as a function of their distance [1,2].

The Kondo effect originates from the screening of the spin of a magnetic impurity by the surrounding conduction band electrons and is characterized by a strong peak in the impurity's density of states near the Fermi level. In scanning tunneling spectroscopy (STS) spectra, it shows up as a feature which can be described by a Fano line shape. From a fit, the peak width Γ is obtained which is proportional to the characteristic energy scale – the Kondo temperature T_K – of the impurity system.

As a second impurity is brought into proximity, magnetic interactions between the impurities become important and may considerably modify the Kondo resonance. Here, we demonstrate that it is possible to determine the magnetic interaction between single magnetic atoms adsorbed on a noble metal surface by determining its influence on the Kondo spectrum. The results are compared to theoretical predictions of the magnetic interactions between single atoms [3]. The evolution of the Kondo line shape obtained by STS upon varying the interatomic distance between Co adatoms in dimer

and trimer configurations on a Cu(100) single crystal surface is compared to many body theory, which allows us to determine the magnetic coupling as function of the interatomic spacing. Dimers with well-defined interatomic separation have been fabricated by first forming cobalt carbonyl complexes. The CO ligands inhibit nucleation and island formation and facilitate the growth of one-dimensional structures. Once these structures are grown, the CO ligands can be removed by tip-induced dissociation of the molecules leaving only the cobalt atoms behind on the surface. The panels in Fig. 12(a) show different cobalt dimer configurations prepared as described above with interatomic distances between the neighboring cobalt atoms ranging from 2.56 Å to 8.1 Å together with the corresponding STS spectra. For the compact dimer the interaction between the spins is much stronger than the coupling to the substrate and the Kondo effect (at 6 K) is suppressed. For the next-nearest neighbor distance, however, a resonance is found at the Fermi energy. The resonance is considerably broader than that of a single cobalt adatom. By fitting the STS signal with a single Fano line shape, we extract that the energy width of the feature would correspond to a Kondo temperature $T_K = 181 \pm 13$ K. For distances larger than 5 Å the Kondo resonance has almost recovered the width and line shape of the resonance of a single cobalt adatom. The widths of the resonances are summarized in Fig. 12(b).

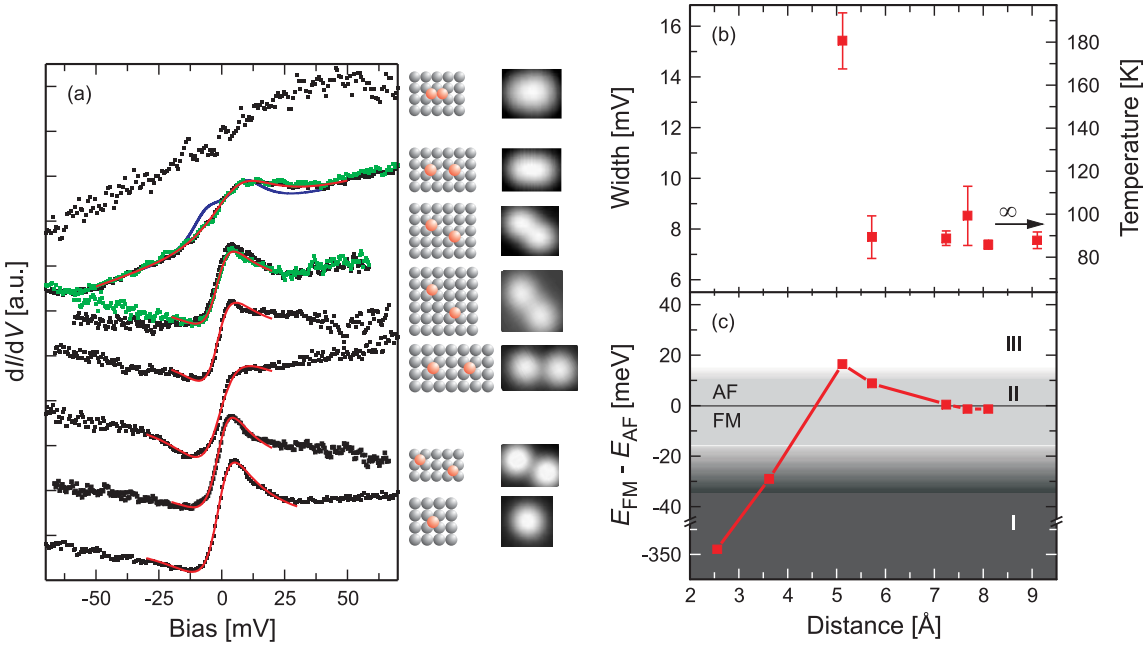

Figure 12: Kondo resonance of cobalt dimers on Cu(100) measured by scanning tunnelling spectroscopy at 6 K. As a consistency check, spectra taken on both ends of the dimers are shown (green and black dots) to be equivalent. (a) Model, topography and spectra for (from top to bottom) a compact dimer (2.56 Å), a dimer at 5.12 Å, at 5.72 Å, at 7.24 Å, at 7.68 Å, at 8.10 Å and for a single adatom at infinite distance (> 20 Å) are depicted. The spectra are shown together with fits of a Fano function (red solid line), for the dimer at 5.12 Å also a simulated curve with $J = 15$ meV and $\Gamma = 1.2\, T_K^0$ is plotted (blue solid line). For the dimer at 5.12 Å, a linear background had to be taken into account to obtain a reasonable fit for a Fano function. (spectra shifted vertically for clarity) (b) shows the width of the resonance as a function of distance and (c) KKR calculations for the exchange interaction between cobalt adatoms on Cu(100) [3]. The three distinct regimes discussed in the text are shaded in different greys.

Our data can be theoretically interpreted as a realization of a two-impurity Kondo problem. Depending on the relative strength of the exchange interaction compared to the single impurity Kondo temperature T_K^0, the dimers enter different regimes. For a strong ferromagnetic exchange interaction $|J| \gg T_K^0$ (marked as regime I in Fig. 12(c)) a correlated state with a new Kondo temperature $T_K^{dimer} \approx (T_K^0)^2/|J|$ will occur. This new Kondo scale is much lower than the temperature of the experiment and can therefore not be detected in our measurements. For intermediate exchange interaction J (regime II in Fig. 12(c)), the single impurity Kondo resonance is recovered.

Finally, for a sufficiently strong antiferromagnetic exchange interaction $J > J^\star \approx 2\,T_K^0$ (marked as regime III in Fig. 12(c)) between neighboring magnetic atoms, the Kondo resonance is split and a singlet state is formed between the impurities. This singlet state is characterized in the impurity density of states by peaks located at energies $\pm J/2$ [4]. We can show that the splitting can be described by a sum of two Fano resonances at $\pm J/2$ with a width Γ which is of the same order as the single impurity one. The resonances appear in the tunneling spectrum as only one broadened feature due to the width of the resonances, which is of the same size as the splitting. Thus the width of the resonance in this case provides a measure for the magnetic interaction between the adatoms.

Experimentally, we find that for the compact dimer (2.56 Å) the Kondo resonance disappears. This is consistent with previous experiments on Co dimers on Au(111) by Chen *et al.* [2] and the strong ferromagnetic coupling predicted by *ab initio* calculations [3]. The coupling introduces a Kondo scale $T_K^{dimer} \approx 2\,K$ for the nearest neighbor dimer, which is smaller than the temperature of the experiment. The spectrum on the next-nearest neighbor dimer (5.12 Å) shows a distinct Kondo resonance at the Fermi level, which is broadened compared to the spectrum of the isolated Co adatom. From the width of the resonance we can extract an antiferromagnetic coupling J of about 16 meV. The broadened spectrum can be rationalized by an antiferromagnetic coupling between the two Co adatoms. The relevant Kondo energy scale is $k_B T_K = 7.58$ meV for a Co atom on Cu(100).

The magnetic interactions are thus large enough to induce a singlet-triplet splitting but still small enough to prevent complete quenching of the Kondo effect as observed for the compact dimer. At larger interatomic distances the spectrum and T_K transforms back to the single adatom value, with the exception of an interatomic distance of 7.68 Å, where the resonance width has a local maximum as a function of distance. According to *ab initio* calculations [3], the interaction between two cobalt adatoms on Cu(100) is mainly due to RKKY interactions. When the adatoms are on next-nearest neighbor sites, Stepanuyk *et al.* predict an antiferromagnetic interaction of about 17 meV (Fig. 12(c)). This is in excellent agreement with the estimation we obtain assuming a split Kondo resonance. When the adatoms are further apart (5.72 Å), the calculations predict that the RKKY interaction is reduced to 8 meV, which is not large enough to split the Kondo resonance and therefore explains why the usual single impurity Kondo resonance is almost recovered.

Next to the cobalt dimers, we have studied linear trimers. The trimers have the adatoms on next-nearest neighbor sites as shown in Fig. 13(a) and (b) and have been prepared in a similar way as the dimers. The tunneling spectra change qualitatively on a trimer. As can be seen from Fig. 13(c), the spectra show a superposition of features – resulting in two maxima and a dip in between them.

A theoretical analysis within a slave boson mean field theory [5] reveals that the two zero-bias resonances are collective features putting the trimer in the correlated Kondo regime. The nearest neighbor spin interaction of the trimer is found to be comparable to that of the dimer.

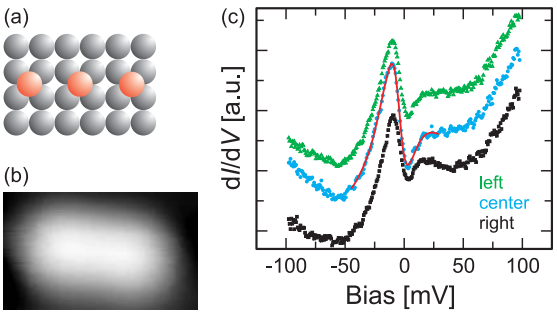

Figure 13: Kondo resonance of the Cobalt trimer on Cu(100) measured by scanning tunneling spectroscopy at 6 K. (a) Model of the trimer investigated, (b) STM topography (same scale as model). (c) Spectra taken on the left, right and center atom, the spectra are shifted vertically. The solid line is a fit to a double Fano resonance.

In conclusion, we have shown how the magnetic interaction between single magnetic atoms coupled to a substrate can be determined via the Kondo effect. Understanding and being able to measure the magnetic coupling on the single atom level is expected to play a key role in the design of magnetoelectronic devices. Magnetic nanostructures with specific properties can be tailored by controlling and manipulating the exchange interaction.

[1] *Wahl, P., P. Simon, L. Diekhöner, V.S. Stepanyuk, P. Bruno, M.A. Schneider and K. Kern.* Physical Review Letters **98**, 056601 (2007).

[2] *Chen, W., T. Jamneala, V. Madhavan and M.F. Crommie.* Physical Review B **60**, R8529–R8532 (1999).

[3] *Stepanyuk, V.S., A.N. Baranov, D.I. Bazhanov, W. Hergert and A.A. Katsnelson.* Surface Science **482-485,** 1045–1049 (2001).

[4] *Lopez, R., R. Aguado and G. Platero.* Physical Review Letters **89**, 136802 (2002).

[5] *Lazarovits, B., P. Simon, G. Zaránd and L. Szunyogh.* Physical Review Letters **95**, 077202 (2005).

Rational synthesis and structure of complex compounds

Complex chemical compounds are a central feature of the research performed in this Institute, both on their own merit with regard to their synthesis and structure and as a starting point for measurements and theoretical calculations of their physical properties. In this section, the focus is on the former aspect: Synthesis and structure. The past decades have seen a surge in the field of solid state synthesis aimed at a deeper understanding and rational control of such syntheses and of the structural and physical properties of the resulting compounds. Perhaps most surprising is the prominence of theoretical computations in this enterprise, showing by now the faint outlines of a new sub-discipline one might rightfully call theoretical solid state chemistry. In this section, one thus finds that, e.g., theoretical investigations of the energy landscape of chemical systems such as LiBr are combined with new techniques of experimental explorations, and analogies between oxomolybdates and rare earth cluster compounds are employed to open up a new field of systematic syntheses. Similarly, theoretical optimal control studies of phase transitions stand side by side with the fine-tuning of the growth conditions of superconducting crystals. Focusing more strongly on structural aspects, theoretical investigations of chemical bonding in Laves phases are correlated with their geometrical properties, and the full quantitative phase analysis of Sorel cements should allow an efficient quality control of such industrially important materials.

Theoretical and experimental exploration of the energy landscape of LiI and LiBr

Ž. Čančarević, I.V. Pentin, J.C. Schön, Y. Liebold-Ribeiro, A. Müller, D. Fischer and M. Jansen

Our approach towards synthesis planning in solid state chemistry is based on the so-called energy landscape concept. Here, each chemical compound that is capable to exist for a given period of time in a given (equilibrium) geometry is associated with a locally ergodic (minimum) region on the energy landscape over the configuration space. The prediction of the existence and stability of (meta)-stable phases in a chemical system is realized via a two-step process: Identification of structure candidates through global exploration of the classical empirical energy landscape, followed by a local optimization of the candidates on ab initio level employing a heuristic algorithm. From the computed energy/volume curves, one can then calculate the thermodynamically stable phases at a given pressure and the transition pressures among the phases. In order to gain insight into the kinetic stability of the structure candidates, one computes estimates of the energy and enthalpy barriers around the structures with the so-called threshold algorithm, yielding a tree graph representation of the chemical system.

In order to validate our predictions by experiments, we have employed the 'Low-Temperature-Deposition' technique developed by us, which allows to deposit the desired compound at very low temperature onto a substrate. After transferring the samples to a diffractometer the structure(s) of the compounds are analyzed as function of temperature.

To illustrate this approach, we present here the results of a theoretical and experimental study of the LiI and LiBr energy landscape. First, we determined the structure candidates, constructed the tree graph representation and computed the ab initio energy/volume curves for the hypothetical structures. Next, samples of LiI and LiBr were prepared as thick films evaporated from a self-made resistance heater (LiI: 430°C, LiBr: 440°C) and deposited onto a cooled sapphire substrate (LiI: –196°C, LiBr: –50°C) inside an ultrahigh vacuum chamber for a period of 3 to 5 hours. The X-ray powder patterns were obtained in reflection mode with an area-sensitive detector under high vacuum. The corresponding diffractogram was obtained by integration of the two-dimensional diffraction cones.

The resulting tree graph for the most important structure candidates of LiI is shown in Fig. 14 [1]. We find that the global minimum on the energy landscape is the rock salt structure type, with, e.g., the NiAs-, wurtzite and sphalerite structure types apparently being stable side minima.

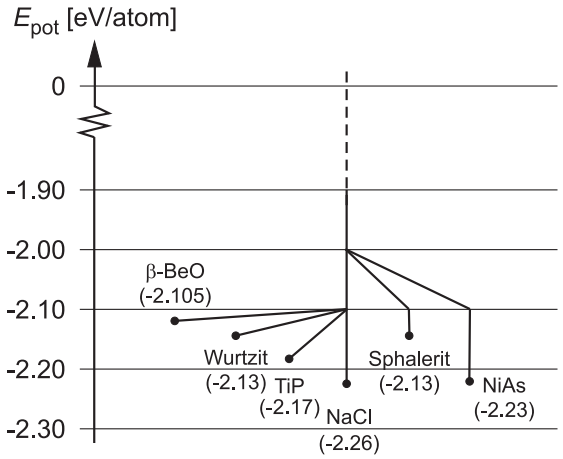

Figure 14: The six most important structure candidates for the LiI system determined by global optimization, together with the barrier structure shown in the form of a tree graph.

Figure 15 shows the stability region as function of pressure for LiBr (E(V)-curves) for intermediary positive and negative pressures in the general range from –10 to +10 GPa based on global explorations of the enthalpy landscapes of lithium bromide [2].

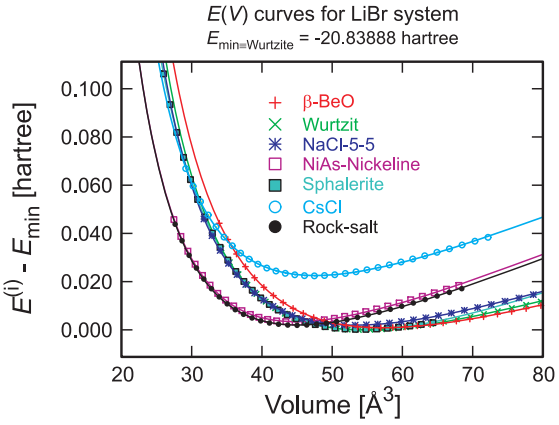

Figure 15: $E(V)$-curves for selected low energy structure candidates, discovered by global searches of the LiBr energy landscape, followed by a local optimization of each polymorph on ab initio level.

In agreement with these predictions a new, metastable polymorph of this compound (β-LiBr) has been synthesized. β-LiBr crystallizes in the wurtzite type of structure, $P6_3mc$, $a = 4.1509(5)$ Å and $c = 6.6502(2)$ Å. Single phase samples of β-LiBr were obtained at –50°C and a vapor pressure of $2.3 \cdot 10^{-4}$ mbar. Outside this set of experimental parameters, mixtures of α-LiBr (rock salt structure) and of β-LiBr were obtained. Figure 16 shows the X-ray patterns of LiBr (deposited at –50°C) analyzed under heating up to room temperature; such samples undergo a structural phase transition to the standard rock salt structure.

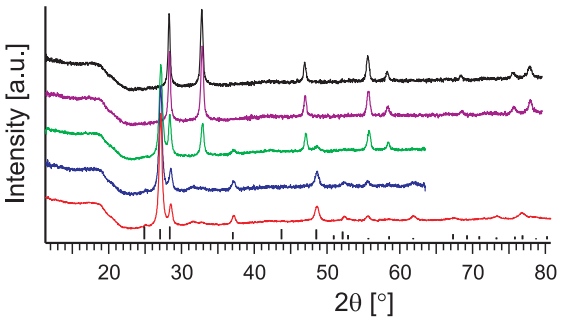

Figure 16: X-ray powder patterns of LiBr (deposited at –50°C), taken at –50°C, –30°C, –10°C, 10°C and room temperature (from bottom to top), line diagram: β-LiBr.

LiI deposited at –196°C shows already at this temperature weak broad Bragg reflections of the hexagonal wurtzite modification; (β-LiI) with $a = 4.514$ Å, $c = 7.311$ Å. Above 0°C LiI transforms irreversibly into the cubic rock salt modification. During that investigation it was shown that solid solutions $LiBr_{1-x}I_x$ $(0.25 \leq x \leq 0.8)$ can also be obtained as hexagonal wurtzite modifications [3]. Compared to β-LiI, these solid solutions are more stable and transform into the cubic phase at the significantly higher temperature of 80°C.

These observations were confirmed by a subsequent study of the energy landscapes of the LiBr–LiI system, where we showed that two solid solution phases exist in this system: A metastable and a stable one in the wurtzite and in the rock salt structure type, respectively [4].

Taken together, these experimental and theoretical results constitute further strong evidence for the feasibility of our energy landscape concept as an approach to rational solid state synthesis.

[1] *Čančarević, Ž., J.C. Schön, D. Fischer and M. Jansen.* Materials Science Forum **494**, 61–66 (2005).

[2] *Čančarević, Ž., J.C. Schön and M. Jansen.* Asian Journal of Chemistry (2007), accepted.

[3] *Fischer, D., A. Müller and M. Jansen.* Zeitschrift für anorganische und allgemeine Chemie **630**, 2697–2700 (2004).

[4] *Schön, J.C., I.V. Pentin and M. Jansen.* Journal of Physical Chemistry B **111**, 3943–3952 (2007).

Searched for and found: Analogies between reduced oxomolybdates and cluster compounds of rare earth metals

L. Kienle, Hj. Mattausch, V. Duppel, M.C. Schaloske and A. Simon

The concept of cluster condensation has proved valuable as an ordering scheme for structures of metal-rich compounds, and it frequently has opened new areas of research. Reduced oxomolybdates illustrate the value of the concept particularly well. In their structures discrete anions occur which are formed from n Mo_6O_{12} clusters linked via opposite edges of the Mo_6 octahedra. So far, monomeric and oligomeric entities with n ranging from 1 to 6 are known as well as the polymeric Mo_4O_6 chain, $n = \infty$. Oligomeric clusters occur in crystal structures which are composed of a single type of cluster only as well as different types in ordered or disordered arrays.

Rare earth metal halides (RE,X) containing discrete RE_6Z and $RE_{10}(Z)_2$ units have been known for a long time, which correspond to the initial members, $n = 1$ and 2, respectively, of the molybdenum cluster series. Due to the electron deficiency of the rare earth metals additional endohedral atoms or groups of atoms, Z, which (over-) compensate the lack of metal-metal bonding by strong RE–Z bonding are incorporated in the cluster centers. The polymeric chain RE_4Z, too, has been found repeatedly.

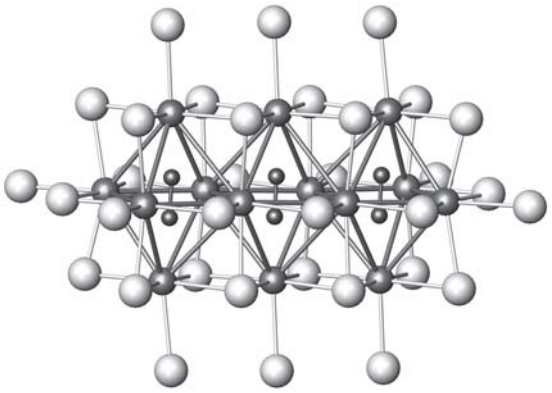

Figure 17: Trimeric cluster in $La_{14}(C_2)_3I_{20}$. Octahedra highlighted by thick lines.

Recently, we could characterize $RE_{14}(C_2)_3I_{20}$ (RE = La, Ce) as the first representatives for n = 3 (Fig. 17). Minute deviations from the optimized reaction temperatures lead to heterogeneous products which exhibit characteristic disorder phenomena in the crystals. The disorder is seen in single crystal X-ray analyses, and its nature becomes clear from investigations of the real structure in the electron microscope.

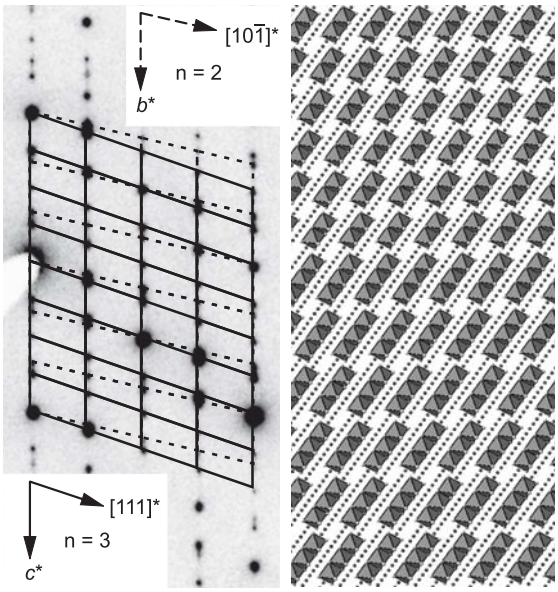

Figure 18: Left: Electron diffraction pattern, zone axis [–110] referring to n = 3, right: Scheme of an intergrowth of $La_{14}(C_2)_3I_{20}$ (n = 3) and $La_{10}(C_2)_2I_{15}$ (n = 2).

The heterogeneous character of a sample of $La_{14}(C_2)_3I_{20}$ prepared at 900°C shows up in the X-ray as well as the electron diffraction pattern of a selected single crystal. The observed reflections in the latter are shown in Fig. 18 and are interpreted in terms of coherently intergrown domains of layer-wise arranged $La_{14}(C_2)_3$ and $La_{10}(C_2)_2$ units. Structures of this type have not been detected before in cluster phases of rare earth metals. In the closely related oxomolybdates larger clusters, n > 3, also frequently occur. A systematic search for such larger clusters with rare earth metals finally was successful by focussing on crystals which attracted attention due to diffuse streaks in their electron diffraction pattern. In Fig. 19 simulated contrasts of a model structure composed of cluster layers with n = 2, 3 and 4 are shown. In the Scherzer focus the distances between the elongated light spots (parallelogram corners) are a measure of the cluster length.

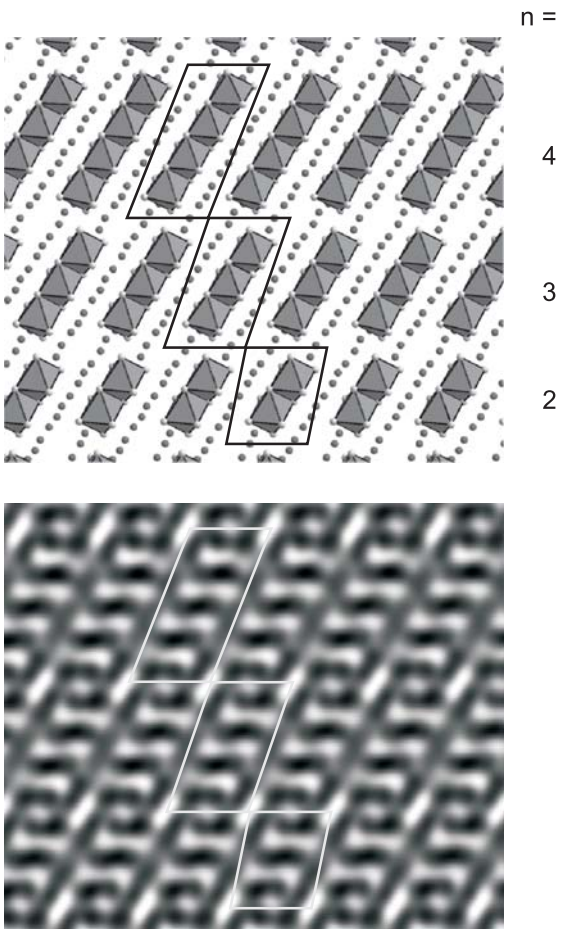

Figure 19: Structure model with n = 2, 3 and 4, together with simulated micrograph (zone axis: [–110] referring to n = 3, Δf = –55 nm, thickness: 3.5 nm).

Figure 20 presents the experimentally found contrasts seen in a disordered sample of average composition $Ce_{14}(C_2)_3I_{20}$. These can be associated with well-defined cluster sizes. Whereas Fig. 20(a) reproduces layered domains of clusters with n = 1, 2 and 3 which are well-known though observed for the first time in compounds of cerium, Fig. 20(b) contains the images of significantly larger clusters, n = 8, 10. Extended investigations of numerous crystals verify the existence of an entire spectrum of clusters with n > 3.

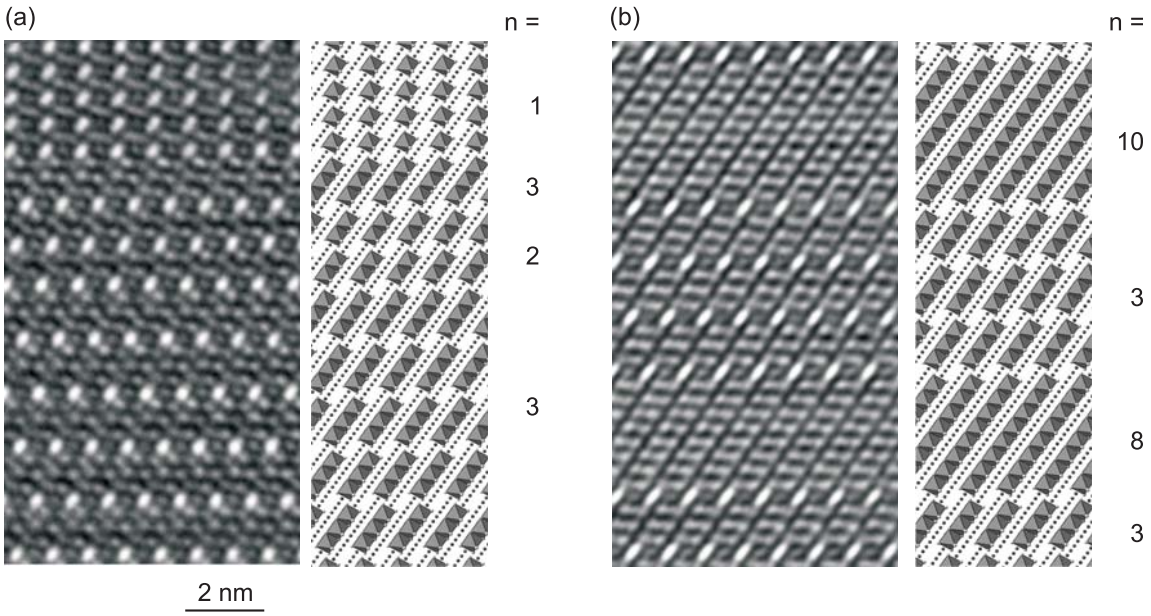

Figure 20: High resolution micrograph and structure schemes for (a) intergrowth of layers with n = 1, 2, 3 and (b) n = 3 and n = 8, 10 (zone axis: [–110] referring to n = 3).

The results described above establish surprising similarities in the structural chemistry of reduced oxomolybdates and carbide halides of rare earth metals. However, significant differences also exist. The cluster sizes observed with the compounds of rare earth metals exceed those of oxomolybdates known so far.

A more serious difference is due to the fact that in the oxomolybdates the clusters are anions and have to be interconnected in a definite way to provide space for the cations, e.g., in $In_{n+1}Mo_{4n+2}O_{6n+4}$. In contrast, the carbide halide clusters are neutral entities allowing for variable patterns of interconnection which result in three known homologous series, ($RE_{4n+2}Z_nX_{6n+4}$, $RE_{4n+2}Z_nX_{6n+6}$ and $RE_{4n+2}Z_nX_{5n+5}$) characterized by different kinds of bridging via X atoms. Representatives of all these series are known today in particular for n = 2 and, as final members, n = ∞. A wide-open field of systematic synthesis lies ahead.

Finite-time thermodynamics and the gas-liquid phase transition

M. Santoro, J.C. Schön and M. Jansen

One of the most interesting field in solid state chemistry is the prediction of new structures of solid compounds and the design of routes to their synthesis. This approach is based on the idea that such structure candidates correspond to locally ergodic regions on the energy/enthalpy landscape with sufficiently high barriers and low local free energy. Trying to analyze the metastability of these phases and the transitions among them leads us to apply the concepts of finite-time thermodynamics to the determination of the thermodynamically optimal paths across such barriers, e.g., in chemical reactions or in phase transitions.

For a given temperature and pressure, the phase with the lowest free energy is thermodynamically stable. However, when only a finite time is available for, e.g., a first order phase transition to take place, a given phase can often persist for a considerable time even at temperatures and pressures where it has become thermodynamically unstable. Accelerating such a process usually can be achieved by moving from the phase boundary in parameter space deeper into the region of the new phase. As a consequence, the transition in finite time takes place under non-equilibrium conditions. Thus, dissipation occurs and excess work is required.

Our goal was to solve the optimal control problem of achieving such a transition in an optimal fashion, in the sense that the excess work required was minimized by controlling the appropriate thermodynamic parameters. As a concrete example we chose the transition from the gaseous to the liquid phase [1].

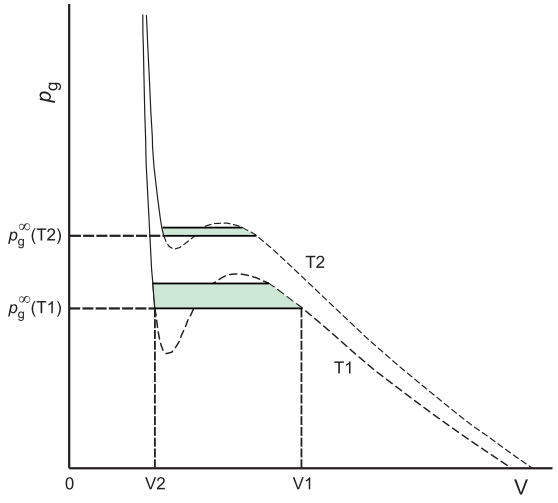

Figure 21: The shaded region represents the work, called *excess work*, needed to achieve a first-order phase transition by supersaturating the gas at standard conditions ($p_g^\infty(T^{\mathrm{boil}})$,$T^{\mathrm{boil}}$).

Since the main goal was the application of the principles of finite-time thermodynamics to first order phase transitions, we employed some simplifications in the description of the actual physical system, such as using classical nucleation theory when modeling the gas-liquid transition. We have defined a molecular transfer rate from the gas to the liquid phase in which both a nucleation and a growth term were present. The excess work is the work needed to achieve the transition at supersaturation, which is null if $p_g = p_g^\infty$, increases as a function of p_g/p_g^∞, and can be visualized by the shaded region in Fig. 21. Minimizing this excess work while moving the system from the gaseous to the liquid phase is equivalent to the following optimal control problem in the framework of finite-time thermodynamics and classical nucleation theory:

$$min[W_{\mathrm{exc}}(p_a(t_0), p_a(t_f)) + \int_{t_0}^{t_f} \frac{dW_{\mathrm{exc}}}{dt}(n_l(t), p_a(t), \dot{p_a}(t), t)dt], \quad (1)$$

subject to:

$$\dot{n_l}(t) = n_l^c J_{ss}^c + \frac{(4\pi)^{\frac{1}{3}}(3v_l)^{\frac{2}{3}}}{\sqrt{2\pi mkT}} n_l^{\frac{2}{3}}(p_a - p_g^\infty)(\int_0^t J_{ss}^c dt')^{\frac{1}{3}} \quad (2)$$

$$\dot{p_g}(t) = \dot{p_a}(t), \quad (3)$$

with $n_l(t_0) = n_l^0$, $n_l(t_f) = n_l^f$, $p_a(t) \in [p_g^\infty, \infty)$, $\dot{p_a}(t) \in (-\infty, \infty)$. Here, we assumed that the delay of equilibration of the internal pressure p_g to the applied external pressure p_a was essentially zero, i.e., $p_g(t) = p_a(t)$ for all $t \in [t_0, t_f]$.

Three different chemical systems were investigated as typical examples: Nitrogen, oxygen and water vapor. In all three cases, the optimal pressure trajectory $p_a^\star(t)$ could be divided in three pieces: A linear initial rise between $t = 0$ and $t = t_0$ from $p_g = p_g^\infty$ to the maximal pressure $p_a^\star(t_0)$, an extremely fast drop within a fraction of a second, followed by a very slow decrease to p_g^∞ for the remaining duration until $t = \tau$.

Our results show a large growth in the number of critical clusters in the first part of the total pressure path with essentially no nucleation along the subsequent optimal trajectory: After the initial burst of nucleation the transition proceeds via cluster growth.

Table 1:
The initial pressure $p_a^\star(t_0)$, $n_l^\star(t_0)$, $N^c(t_0)$, and the total excess work performed within time τ for nitrogen N_2.

τ [s]	$p_a^\star(t_0)$ [Pa]	$n_l^\star(t_0)$	$N^c(t_0)$	ΔW_{exc} [J]
10^0	228415	$6.11503 \cdot 10^{10}$	$5.01897 \cdot 10^8$	3.233
10^1	222330	$2.11668 \cdot 10^9$	$1.57272 \cdot 10^7$	3.221
10^2	216955	$7.34058 \cdot 10^7$	496830	3.205
10^3	212165	$2.54588 \cdot 10^6$	15782	3.194
10^4	207855	87563	499	3.187
10^5	203960	3006	16	3.180

Table 2:
Power laws of $n_l^\star(t_0)$, $n_l^c(t_0)$, N_l^c, $p_a^\star(t_0)$ and W_{exc} as a function of τ for nitrogen, oxygen and water vapor.

	Nitrogen	Oxygen	Water vapor
$n_l^\star(t_0)$	$6.11 \cdot 10^{10}\,\tau^{-1.46}$	$6.88 \cdot 10^{10}\,\tau^{-1.46}$	$2.91 \cdot 10^{11}\,\tau^{-1.46}$
$n_l^c(t_0)$	$118\,\tau^{0.04}$	$101\,\tau^{0.04}$	$119\,\tau^{0.04}$
N_l^c	$5.02 \cdot 10^8\,\tau^{-1.5}$	$6.59 \cdot 10^8\,\tau^{-1.5}$	$2.37 \cdot 10^9\,\tau^{-1.5}$
$p_a^\star(t_0)$	$228415\,\tau^{-0.0098}$	$259730\,\tau^{-0.0114}$	$217600\,\tau^{-0.0096}$
W_{exc}	$3.233\,\tau^{-0.001436}$	$5.43\,\tau^{-0.001566}$	$35.9\,\tau^{-0.002046}$

As function of the final time τ, the optimal pressure trajectories shift downward throughout. An important feature is that, in the interval $[t_0, \tau]$, we find a negative excess work due to the rapid drop in $p_a^\star(t)$. Moreover, while in the first stage of the process we do work $W_{exc}(p_a^\star(t_0))$ to supersaturate the gas up to $p_a^\star(t_0)$, in the second stage we regain most of the work spent. The total work for nitrogen, oxygen and water vapor decreases monotonically with τ, as we would expect (Tab. 1).

Essentially all relevant quantities such as the excess work and the initial pressure $p_a^\star(t_0)$ follow a power law as function of τ (Tab. 2). However, the actual value of $p_a^\star(t_0)$ is due to the complicated interplay of surface tension, boiling temperature and molecular volume specific to each system. We find, on the one hand, that for $T = T_{boil}$ ($p_g^\infty = 1$ atm) the oxygen system requires higher pressure values at $t = t_0$ than nitrogen and water vapor. On the other hand, water vapor requires a much greater amount of excess work to supersaturate the gas compared to oxygen and nitrogen, implying a greater change in volume throughout the phase transition for water vapor than for the other two gases.

This finite-time thermodynamics approach to the dynamics of phase transitions could be extremely useful, in our opinion, for applied and experimental work on controlling first order phase transitions, and it should enable us to develop efficient algorithms for the computational modeling of such transitions. Moreover, liquification of gases from the atmosphere constitutes a major enterprise, where even a few percent of energy savings would be noticeable. Thus, analyzing the methods currently employed in industry using techniques from finite-time thermodynamics could prove to be quite profitable also from an economic point of view.

[1] *Santoro, M., J.C. Schön and M. Jansen.* Physical Review E **76**, 061120 (2007).

Improved flux growth of pure/substituted $YBa_2Cu_4O_8$ single crystals

G.L. Sun and C.T. Lin

In the Y-Ba-Cu-O cuprates superconducting systems, three superconducting phases have been identified to date. They are generally formulated by $Y_2Ba_4Cu_{6+n}O_{14+n+\delta}$, where $n = 0, 1, 2$ represent the number of CuO_2 layers with single and/or double Cu–O chains. The superconducting transition temperatures T_c are 93 K, 20–93 K and 80 K for the $n = 0, 1$ and 2, namely, Y-123, Y-247 and Y-124, respectively. Among these the Y-247 is considered to be an intergrowth of Y-123 and Y-124. Y-124 has an extremely unique feature, for instance, greater thermodynamical and structural stability than the Y-123. However, the synthesis of the Y-124 compound comparing to Y-123, especially as a single crystal is rather more difficult. Owing to the limitation of the reaction kinetics of Y-124, synthesis of the compound required a suitable catalyst or a high O_2 pressure up to 3000 bar to enhance the reaction rate of formation. Furthermore, the study of the substitutions in Y-124, especially in single crystal was rarely reported due to the limited availability of the specimens. In previous studies we explored a new method using KOH as flux for growing single crystals in air or O_2 at temperatures as low as 550°C under ambient pressure [1]. Recently we have improved the flux growth method by increasing the temperature gradient and adding a small amount of B_2O_3 in the solution to obtain large and high quality Y-124 crystals. The crystals doped with Ca, Zn and Ni have been also successfully grown by this method. The influence of substitution on superconductivity was investigated.

For the growth of pure or doped Y-124 single crystals, the source materials used are the mixture of Y-123, CuO and CaO, ZnO or NiO. The KOH (60wt%) served as a solvent and an Al_2O_3 or ZrO_2 crucible was employed. The growth was then carried out in a resistive-heated vertical furnace with two heating zones, having a sharp temperature gradient of $\Delta T \approx 8$°C/cm at the heating temperature of around 750°C. The cooling rate of 1–4°C/h was applied during the growth and crystals were formed by a spontaneous nucleation in the KOH solution.

The growth of the Y-124 crystal involves several chemical reactions and processes, including synthesis, dissolution and crystallization. The crystals can form via the reaction:

$$YBa_2Cu_3O_{7-\delta} + CuO + \frac{\delta}{2}O_2 \rightarrow YBa_2Cu_4O_8 \quad (4)$$

Due to the limitation of reaction kinetics, some catalytic additives like alkali carbonate [2] were used to enhance the reaction rate, but the formation of the Y-124 phase still required a high temperature (over 800°C) and a long calcination (up to several days). Using KOH as solvent, we found that Y-124 can be synthesized via the reaction (1) in molten KOH at a temperature as low as 550°C, and a high fraction (>95%) of the Y-124 phase was achieved for a reaction time less than 4 h. The fact is that the high oxidation state, Cu^{3+}, can be stabilized by the O_2^-- and O_2^{2-}-ions in molten KOH and thus in favoring the formation of the Y-124 phase. These results suggest that molten KOH is very effective in accelerating the reaction to form Y-124 during the growth process. Our previous result showed the solubility of Y-124 estimated as high as 50wt% in 60wt% KOH solvent at 750°C. The analysis of TG/DTA (Thermal-gravimetric/Differential-thermal-analysis) indicated that the crystallization temperature of Y-124 could start at as low as 500°C and end at 750°C, provided no serious evaporation loss or complete exhaust of the molten KOH occurred in the temperature range. Therefore the use of a ccrucible lid with small holes can prevent a fast loss of the investigated KOH in a longer activation time of the flux and then the ability to grow large crystals.

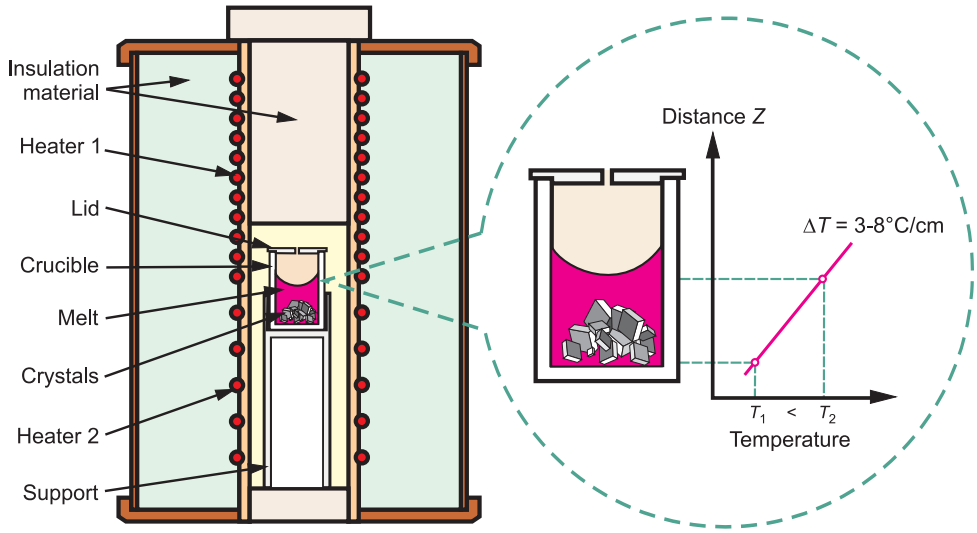

Figure 22: The schematic of the double-heating zone apparatus designed with a sharp temperature gradient, ΔT, ranging from 3–8°C/cm between 550°C and 750°C for the crystallization temperature.

In order to grow large single crystals, it is important to reduce a high number of spontaneous nuclei during the cooling procedure. By the application of a sharp temperature gradient along the crucible, the crystals preferentially grow at the bottom of crucible. Figure 22 shows a two-heating-zone apparatus, specially designed with a sharp temperature gradient distribution from 8°C/cm to 3°C/cm at the growing or cooling temperature from 750°C to 550°C. Using other approach, an amount of 0.5–1.0wt% of B_2O_3 was added in the solution to restrain a high number of nuclei and improve the size of crystals. After the growth the crystals and the residual flux were removed from the crucible and rinsed with methanol. All the as-grown crystals exhibit the rectangular or square platelet habits. The crystal surface is shiny and black-metallic. The dimension of the as-grown crystals is measured up to $1.2\times0.5\times0.3\,mm^3$, which is one order of magnitude larger than our earlier results. Typical crystals are shown in Fig. 23(a). Figure 23(b) gives the XRD pattern, showing the high quality of the as-grown crystal samples without any impurity phases observed.

The study of the influence of substitution on superconductivity in Y-124 is of great interest, since the compound is stoichiometric with a fixed oxygen content in the double Cu–O chain. This is unlike Y-123 with a single Cu–O chain, where a small variation of oxygen (δ) can strongly influence on its superconductivity.

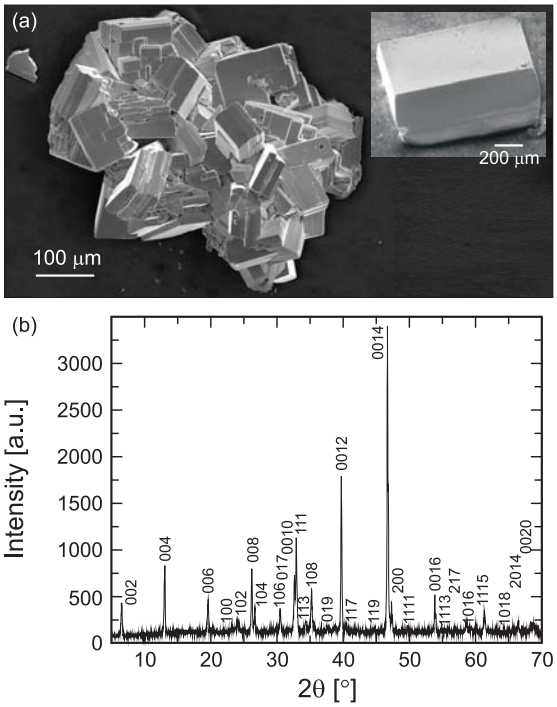

Figure 23: (a) Typical clouded Y-124 single crystals grown by a spontaneous nucleation. Inset is a separated large crystal. (b) The XRD patterns showing the high quality of Y-124 crystal powders; no secondary phases are observed.

The study of the doping in YBCO has established that Ca preferentially occupies the Y site, whereas Zn and Ni possibly reside in the Cu(2) site of the Cu–O_2 plane. The site occupancies of Ca, Zn and Ni in Y-123 and Y-124 are known to be similar.

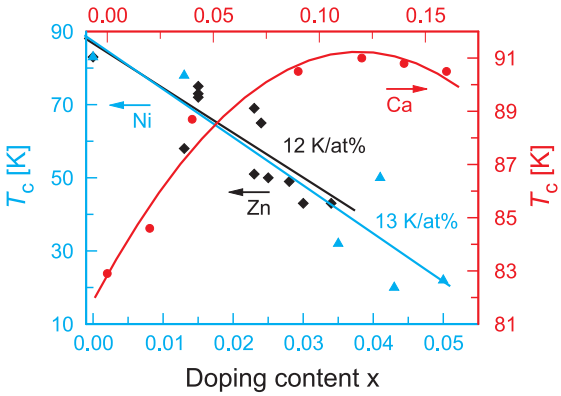

Figure 24: The plot of T_c values versus with dopant concentration for $Y_{1-x}Ca_xBa_2Cu_4O_8$ with x = 0, 0.02, 0.04, 0.09, 0.12, 0.14 and 0.16, for $YBa_2(Cu_{1-x}Zn_x)_4O_8$ with x = 0, 0.015, 0.013, 0.023, 0.024, 0.025, 0.028 and 0.034, and for $YBa_2(Cu_{1-x}Ni_x)_4O_8$ with x = 0, 0.013, 0.035, 0.041, 0.043 and 0.050, respectively.

The substitution of Y^{3+} by Ca^{2+} in fully oxygenated Y-123 superconductors leads to the formation of an overdoped state accompanied by a substantial decrease in T_c. Characterizing the superconductivity of our flux-grown $Y_{1-x}Ca_xBa_2Cu_4O_8$ single crystals, we observe that the value of T_c increases with increasing Ca content, and reaches a maximum of 91 K at x = 0.12. T_c slightly decreases with a further increase of the substitution level to x = 0.16. The results are plotted in Fig. 24, showing a dome shape of under-, optimal- and over-doped regimes. The pure Y-124 compound is known to be in the under-doped state. For the as-grown Y-124, therefore, the increase in T_c with doped Ca could be attributed to the introduction of holes by the non-isovalent substitutions of Ca^{2+} for Y^{3+}, whereas the occurrence of an overdoped regime results in a decease in T_c. Our results are in agreement with those reported on polycrystalline samples of Y-124.

The suppression of T_c in YBCO doped with transition metals is an electronic effect, where the number of free charge carriers decreases with increasing concentration of the substitution atoms. To characterize the influence of transition metal substitution on superconductivity of $YBa_2(Cu_{1-x}M_x)_4O_8$ (M = transition metals) single crystals are grown by KOH flux, where various doping concentrations of Zn and Ni were applied during the growth. The doping content of Zn with $0 \leq x \leq 0.034$ and Ni with $0 \leq x \leq 0.05$ was determined in the final crystal form. Figure 24 is the plot of the T_c values with suppressed rates at 12/at% for the Zn- and 13/at% for the Ni-doped Y-124, respectively. Both dopings show nearly the same suppression rates, but the T_c is lowered from 83 K for the pure compound to ≈ 40 K and ≈ 20 K for the Zn- and Ni-doped Y-124 single crystals, respectively. Nevertheless, these suppression rates are much lower than those previously reported, 18/at% for Zn- and 24/at% for Ni-doped, respectively. This may be due to some difference in the quality of the crystals grown by different synthesis methods. Crystals obtained via low temperature flux growth the obtained crystals show high quality with a sharp transition temperature T_c, while those grown under high pressure and temperature contain of inclusions, thermal strains or inhomogeneous composition, leading to a broad transition or depressing the T_c value.

To summarize, using KOH as flux, the growth of Y-124 single crystals can be easily carried out under ambient pressure at low temperature. The reaction dynamics can be accelerated to form the phase within 4 hours. Large crystal can be obtained by adding B_2O_3 in solution and applying a large temperature gradient. The doping experiments with other 3*d*-metals like Fe and Co are underway. More elaborate physical investigations of these doped crystals will be beneficial for understanding the effect of impurities on superconductivity.

[1] *Song, Y.T., J.B. Peng, X. Wang, G.L. Sun and C.T. Lin.* Journal of Crystal Growth **300**, 263–266 (2007).

[2] *Cava, R.J., J.J. Krajewski, W.F. Peck Jr, B. Batlogg, L.W. Rupp Jr, R.M. Fleming, A.C.W.P. James and P. Marsh.* Nature **338**, 328–330 (1989).

Geometry and bonding in Laves phases

A. Simon; A. Ormeci and Y. Grin (MPI für Chemische Physik fester Stoffe, Dresden)

Laves phases comprise a large group of intermetallic compounds with general composition MN_2 and multicomponent derivatives. Early on, a geometric rule for stability as well as electronic rules for the occurrence of certain structural variations, e.g., cubic versus hexagonal variants, had been developed. The geometric rule identified a critical radius ratio $r_M/r_N = \sqrt{\frac{3}{2}} = 1.225$ as a necessary condition in case of the absence of strong chemical bonding, witnessed by the, at that time, only known alkali metal phase KNa_2. In a Pearson diagram (Fig. 25) this ideal radius ratio is identified as the condition of strain-free M–N and M–M contacts with respect to the atomic radii r_M and r_N of the elements. The distribution of actual structures, however, does not take too much notice of such strain-free contacts.

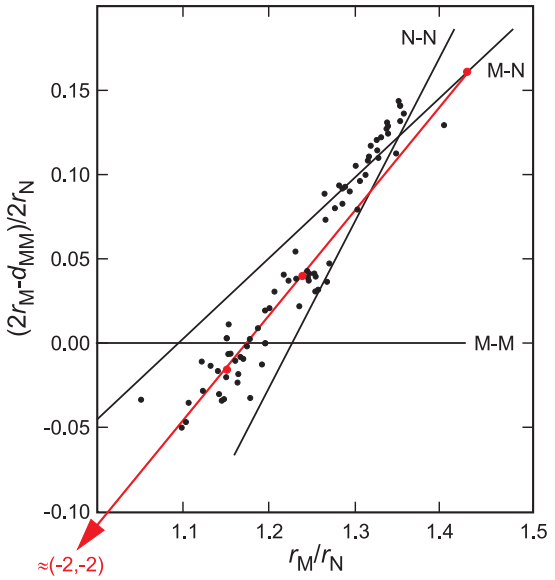

Figure 25: Pearson strain parameter diagram for Laves phases MN_2. Black lines for strain-free N–N, N–M and M–M contacts. Red line through points for CsK_2, KNa_2 and $CsNa_2$ (from left to right) represents a Vegard-type fit, which has its origin at (-2,-2) according to the composition M:N = 1:2.

The discovery of additional Laves phases of the alkali metals, CsK_2 and $CsNa_2$ has disclosed a Vegard-type condition for the interatomic distances, $d_{ij} = F_{ij}(r_M + 2r_N)$, where F_{ij} for different types of atoms is defined by geometry. Atomic sizes are taken from the elements. Their adjustment to the coordination in *fcc* yields r_M and r_N, respectively. By including an adjustment of the latter to the coordination in Laves phases a general relation has been derived, $(2r_M - d_{MM})/2r_N = 0.6450\, r_M/r_N - 0.7670$ with d_{MM} being the shortest distance between the M atoms [1]. The equation describes topologically close-packed structures of atoms with different sizes as the purely geometrical feature of the structural pattern of Laves phases, and it is closely obeyed by numerous phases containing only similar elements (Fig. 26). Deviations from the relationship are also included in Fig. 26. They should reflect chemical bonding effects due to heteropolarity or covalence.

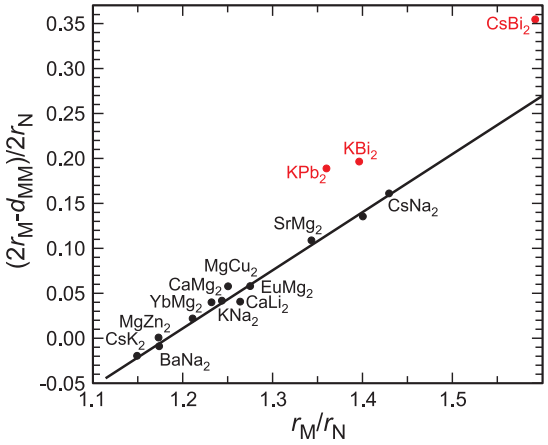

Figure 26: Distribution of phases along the calculated line for Laves phases. Clear deviations marked in red.

In order to visualize differences in the bonding of Laves phases, we analyzed several representatives with regard to the electron localizability. The chemical bonding analysis based on first-principles electronic structure methods was performed within the framework of the electron localizability indicator (ELI) formalism [2]. In this study the full-potential non-orthogonal local orbital method (FPLO) with recently im-

plemented ELI (ELF) module [2] is used. Here we present the first results of a project which was partly realized within the inter-institutional MPG initiative 'Nature of Laves Phases'.

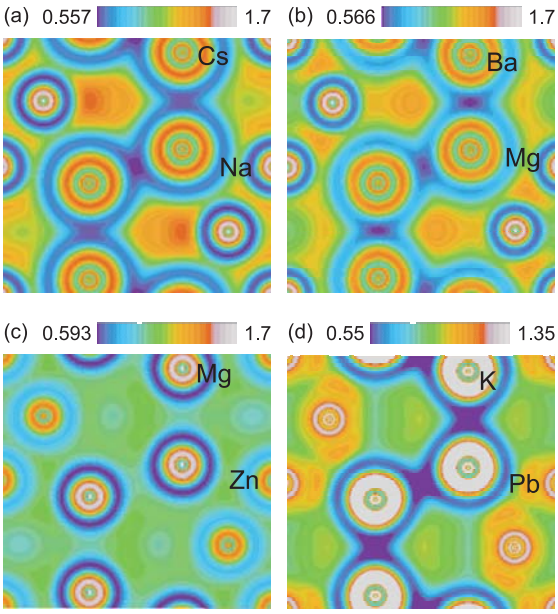

Figure 27: Electron localizability indicator in the crystal structures of Laves phases $CsNa_2$ (a), $BaMg_2$ (b), $MgZn_2$ (c) and KPb_2 (d). ELI distributions in the (11–20) planes are shown together with the colour scale for ELI values of each compound.

Figure 27 shows the distribution of the electron localizability indicator in the diagonal plane of the unit cell of four selected Laves phases with the $MgZn_2$ type of crystal structure. Despite the differences in the chemical composition, the total picture is similar for the compounds presented: The ELI maxima are localized mainly in the vicinity of the N atoms and there are no maxima between the M atoms. More detailed analysis reveals the subtle differences between the presented compounds. In the Laves phases formed solely from alkali metals, KNa_2, $CsNa_2$ and CsK_2, two sets of attractors in the valence region were observed (Fig. 27(a)). Topological analysis shows that these have polysynaptic basins. The bonding in these compounds may be viewed as consisting of three-centre and four-centre bonds between the non-capped N atoms in the Kagomé layers and inside each N_4 tetrahedron. The M atoms act simply as electron donors. This analysis suggests that already in the formation of Laves phases with the lowest valence electron concentration (VEC) chemical bonding together with geometrical factors plays a role in the stabilization of the structural pattern. Increasing VEC we come to $BaMg_2$ and $SrMg_2$ (Fig. 27(b)). There are three sets of ELI attractors, all are close but shifted off the centre of the N–N contacts. All three stand for the mixed multi-center M–N bonding. Two sets are located in the plane of the Kagome layer. The first of them (in front of the edges of capped triangles) represents the six-centre M_4Mg_2 bonds, the second (in front of the edges of non-capped triangles) reveals the four-centre M_2Mg_2 bonds. The third set is located in front of the edges of the bipyramides closer to the apex atoms representing the five-centre bonds M_3Mg_2.

Introducing the transition metals leads to more complex ELI topologies in the Laves phases. The prototypes $MgZn_2$ (Fig. 27(c)) and $MgCu_2$ may be given as examples. In these compounds several ELI attractors were observed around the N atoms. One of them is located inside the N_4 tetrahedron (four-centre bonds similar to the alkali-metal-only Laves phases), while other sets represent various N–M multi-center bonds, like in $BaMg_2$ and $SrMg_2$. Maximization of the electronegativity difference between the components in the case of KPb_2 ($MgZn_2$ type), as well as KBi_2 and $CsBi_2$ ($MgCu_2$ type), provides a bonding situation which is rather unexpected within the traditional picture of this class of compounds. The M-atoms act as electron donors, and a single set of ELI valence attractors is observed. All of them are located in the last shell of the N-atoms (six attractors per N-atom).

Now the corresponding basins are monosynaptic implying a closed-shell-like configuration. A deformation of the last shell in direction to the neighboring N atoms indicates the N–N bonding interaction [4]. This feature provides evidence for a charge transfer from M to N resulting in a formation of N^{x-} anions.

The structure of strongly heteropolar KPb_2 is dominated by a polyanionic framework of corner-condensed Pb_4 tetrahedra known as discrete units from more cation-rich NaPb = $Na_4^+Pb_4^{4-}$. The step from an intermetallic phase to a normal valence compound can be even more pronounced. In $KBi_{1.2}Pb_{0.8}$ the $Bi_{2.4}Pb_{1.6}^{2-}$ tetrahedron becomes nearly valence isoelectronic with elemental phosphorus P_4, and the Laves-type structure distorts into discrete tetrahedral units [5].

In this short survey we show different classes of Laves phases whose bonding situations range from exclusively multi-center bonds between N atoms via an intermediate situation of two-centre bonds in the N partial structure to the formation of N^{x-} anions. No apparent connection is found between the bonding situation common to the members of a class and the location of these members in the near neighbor diagrams except for the last-mentioned salt-like phases.

[1] *Simon, A.* Angewandte Chemie International Edition **22**, 95–113 (1983).

[2] *Kohout, M.* International Journal of Quantum Chemistry **97**, 651–658 (2004).

[3] *Ormeci, A., H. Rosner, F.R. Wagner, M. Kohout and Y. Grin.* Journal of Physical Chemistry A **110**, 1100–1105 (2006).

[4] *Kohout, M., F.R. Wagner and Y. Grin.* Theoretical Chemistry Accounts **108**, 150–156 (2002).

[5] *Ponou, S., N. Müller, T.F. Fässler and U. Häussermann.* Inorganic Chemistry **44**, 7423–7430 (2005).

The crystal structure determination of $Mg_3(OH)_5Cl{\cdot}4H_2O$ (F5-phase) from laboratory powder diffraction data and its impact to the analysis of problematic magnesia floors

K. Sugimoto and R.E. Dinnebier; T. Schlecht (Ostfildern, Germany)

In 1867, the French physicist Stanislas Sorel discovered that high quality cement is formed by mixing magnesium oxide with an aqueous solution of magnesium chloride. These so called Sorel cements have a remarkable capacity to bond with and contain other organic and inorganic materials. Many properties of this magnesia cement are superior to those of Portland cement, namely the high fire resistance, low thermal conductivity, high resistance to abrasion etc. The main application for these cements are grindstones, tiles, artificial stone (cast stone), cast floors, and even artificial ivory (e.g., for billiard-balls). On the down side, magnesia cements shows a poor resistance to prolonged exposure to water, making them unsuitable for construction applications or for toxic and hazardous waste immobilization.

During the binding process, ternary magnesium oxychloride phases are formed, which are of key importance for the properties of the cement. A detailed knowledge of the ternary phase diagram $MgO–MgCl_2–H_2O$ is therefore necessary to understand the properties of these cements and to perform any type of qualitative or quantitative phase analysis. So far, four magnesium oxychloride phases are known in this phase diagram: $2Mg(OH)_2{\cdot}MgCl_2{\cdot}5H_2O$ (F2-form), $3Mg(OH)_2{\cdot}MgCl_2{\cdot}8H_2O$ (F3-form), $5Mg(OH)_2{\cdot}MgCl_2{\cdot}8H_2O$ (F5-form), and $9Mg(OH)_2{\cdot}MgCl_2{\cdot}6H_2O$ (F9-form). The only two phases found at a temperature below 100°C and thus occurring in Sorel cements are the F3- and the F5-phases. The crystal structure of the F3-phase was solved from powder diffraction data in 1953, while that of the F5-phase is unknown. Depending on the production and the setting process, the aging, and environmental influences, with time a typical floor not only consists of the original phases but also of degradation products, of which the most important is a magnesium chlorocarbonate phase (chlorartinite).

The formation of the latter can be explained by the degradation of the F5-phase to the F3-phase according to: $Mg_3(OH)_5Cl{\cdot}4H_2O$ (F5) $\rightarrow$ $Mg_2(OH)_3Cl{\cdot}4H_2O$ (F3) + $Mg(OH)_2$ and consecutively by carbon dioxide of the air to chlorartinite $Mg_2(OH)_3Cl{\cdot}4H_2O$ (F3) + CO_2 $\rightarrow$ $Mg_2CO_3(OH)Cl{\cdot}2H_2O + 3H_2O$. The massive occurrence of chlorartinite serves as an indicator for problematic floors. We recently succeeded in solving the crystal structure of chlorartinite [1]. The zeolite-like channel structure of chlorartinite acts as a buffer for excess $MgCl_2$ in solution, making it very vulnerable for changes in temperature or humidity [2]. Excess $MgCl_2$ in solution leads to the occurrence of $MgCl_2{\cdot}6H_2O$ (Bischofite) or its lower hydrates $MgCl_2{\cdot}4H_2O$, $MgCl_2{\cdot}2H_2O$, or $MgCl_2{\cdot}H_2O$. The crystal structures of the latter three could recently be determined from synchrotron powder diffraction data as function of temperature [3].

In a typical Sorel cement, about 2/3 of the cement consist of inert filler materials, with quartz sand as the dominant phase. Depending on impurities of binder and filler and on the pigments used, a whole list of minerals (most of them having known crystal structures) are found, e.g., calcite, aragonite, hematite, magnesite, feldspar, talcum, muscovite, etc. It is known that the binder of a perfect floor, prepared with high quality materials (e.g., high magnesium oxide reactivity) in equilibrium conditions, consists exclusively of F5-phase. Once the F5-phase is transformed at later stages to the F3-phase and subsequently to chlorartinite, the mechanical strength decreases considerably. In general, the use of inferior components and/or excess water leads to various problems such as the occurrence of cracks in expanding or contracting floors, decoloring, crumbling floors etc. To investigate these phenomena, it is crucial to know the mineralogical composition of these floors quantitatively. Although wet chemical analysis provides some insight in the distribution of elements, the mineralogical composition is much more meaningful. In order to control the production or to evaluate structural damage in the construction business, a full quantitative phase analysis (QPA) using the Rietveld method is necessary, for which the knowledge of the crystal structures of the components is essential.

The only major constituent with an unknown crystal structure is the F5-phase. Since single crystals of a suitable quality for single crystal analysis were difficult to grow, we decided to investigate its crystal structure from high resolution laboratory powder diffraction data. Using this structure in a practical application, a full quantitative phase analysis of two problematic unintentionally bleached magnesia floor was performed, revealing possible causes for the technical failure.

The crystal structure of $Mg_3(OH)_5Cl{\cdot}4H_2O$ (F5-phase) was solved from a high resolution X-ray powder diffraction pattern of a synthetic binder, employing the global optimization method of simulated annealing (SA) as implemented in the program TOPAS. The crystal structure of the F5-phase consists of infinite triple chains of almost regular MgO_6 octahedra running along the *b*-axis and intercalated disordered chlorine ions and water molecules (or hydroxyl groups) (Fig. 28). The octahedron in the middle of the triple chain shares 6 out of 12 edges and all 6 corners with four neighboring octahedra. The outer octahedra share 4 edges, 3 corners with two, and 2 corners with one neighboring octahedron. Thus, one can distinguish between OH^- and OH_2 by applying Pauling's rules. The protruding corners of the octahedron must be occupied by H_2O, while the corners shared by three octahedra can only be occupied by OH^-. The corners shared by just two ocathedra can be occupied by H_2O or OH^-. For reasons of charge neutrality, two alternatives remain. If the channels are occupied by disordered chlorine ions and hydroxyl groups, a hydroxyl group sits statistically on every fourth corner shared by two octahedra. Alternatively, if the channels

(similar to those in the F3-phase) are occupied by chlorine ions and water molecules, corners shared by two octahedra are occupied alternately by water molecules and hydroxyl groups. The triple chains thus are formed by one $Mg(OH)_6$ and two $Mg(OH)_3(OH_2)_3$ or $Mg(OH)_4(OH_2)_2$ octahedra. Additionally, hydrogen bonds increase the stability of the crystal structure.

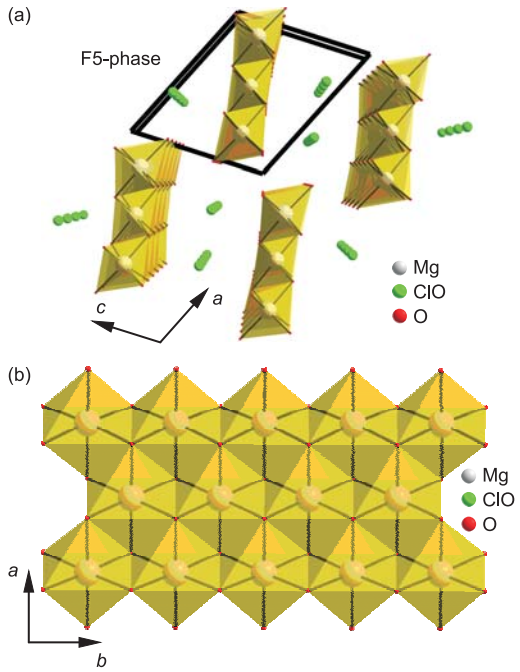

Figure 28: Perspective view of the crystal structure (a) and of the triple chain with one $Mg(OH)_6$ and two $Mg(OH)_4(OH_2)_2$ octahedra (b) as building units of $Mg_3(OH)_5Cl{\cdot}4H_2O$ (F5-phase) at $T = 295$ K in a central projection (camera distance of 35 cm) down to the crystallographic *b*-axis. Oxygen positions are in red, chlorine positions are in light green and magnesium position are in yellow.

With the structure determination of the F5-phase, the crystal structures of all significant binder phases occurring during or after the formation process of Sorel cements are finally known. These phases are: Periclase, brucite, bischofite and its lower hydrates, F3, F5, and chlorartinite. The mineralogical composition of a Sorel cement can now be determined routinely to high precision using quantitative phase analysis (QPA) by the Rietveld method. Such an analysis can be used to determine the quality of a magnesia floor and to determine the causes of cracks and decoloring effects caused by late crystallization. For a practical test, two magnesia floors (colored with iron oxide pigments) which were exhibiting unwanted bleached spots were selected. Floor **(1)**: Industrial quality magnesia floor MA C50 in anthracite color installed in a production plant in southern Germany in 2006. Light grey spots of diameter 10–200 cm occurred 4–8 weeks after installation of the floor without obvious causes. Floor **(2)**: Industrial quality magnesia floor MA C50 in yellow color installed in 2007 in a showroom of a manufacturer of magnesia screeds. White spots occurred within few minutes after pouring and fast removing water on the floor for cleaning purposes (Fig. 29).

Figure 29: Core drill samples of a yellow magnesia floor from southern Germany. The yellow colour was achieved by mixing iron oxides into the MgO powder. Left: Correctly colored sample. Right: Bleached sample.

For the analysis of the magnesia floors, four samples were taken. Sample **(1a)**: interior of floor **(1)**; sample **(1b)**: decolored surface of floor **(1)**; sample **(2a)**: correctly colored surface of floor **(2)**; sample **(2b)**: decolored surface of floor **(2)**. In the case of sample **(1)**, there is a huge difference between the mineralogical compositions of the surface (Fig. 30(a)) and of the interior of the floor (Fig. 30(b)). While the interior shows the expected composition of an equilibrated magnesia floor with F5 as the only binding phase, the surface is characterized by a thin layer of calcium carbonate in different crystalline forms and the decomposition products of the F5-phase, namely the F3-phase and chlorartinite. This can be taken as evidence that

the floor had been correctly laid but that the surface had been quite likely exposed to excessive water during the curing process of the floor.

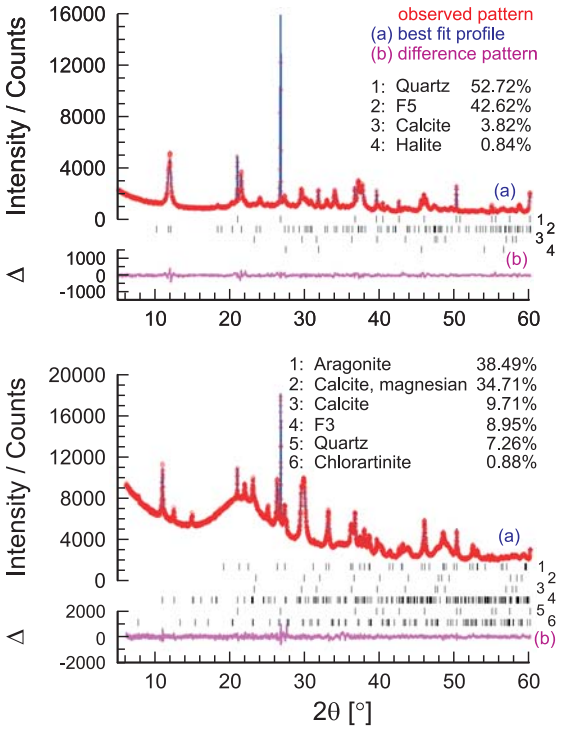

Figure 30: Rietveld plot of a sample taken from the interior (a) and from the surface (b) of a black magnesia floor at $T = 295$ K from southern Germany.

The F5-phase transformed to the F3-phase and subsequently to chlorartinite while calcium ions (the amount of reactive calcium within natural magnesium oxide and magnesium chloride varies for different batches and is usually quantitatively analyzed by the manufacturers of the Sorel cement) were transported to the surface and reacted with CO_2 from air to form different polymorphs of calcium carbonate. The situation for sample **(2)** is entirely different, pointing to a problem with the starting materials. The samples from the correctly colored and from the decolored surface, both reveal an substantial amount of gypsum (8% for **(2a)** and 28% for **2(b)**). It can be assumed that gypsum as an undesired component was already present in the raw material before the floor was laid. Due to its good solubility, the concentration of gypsum in water is enriched in the liquid water during the drying process and brought to the surface by capillary action. When the water evaporates, a thin film of gypsum (and bassanite) is deposited on the surface of the floor. Depending on the local concentration, severe bleaching occurs (Fig. 31).

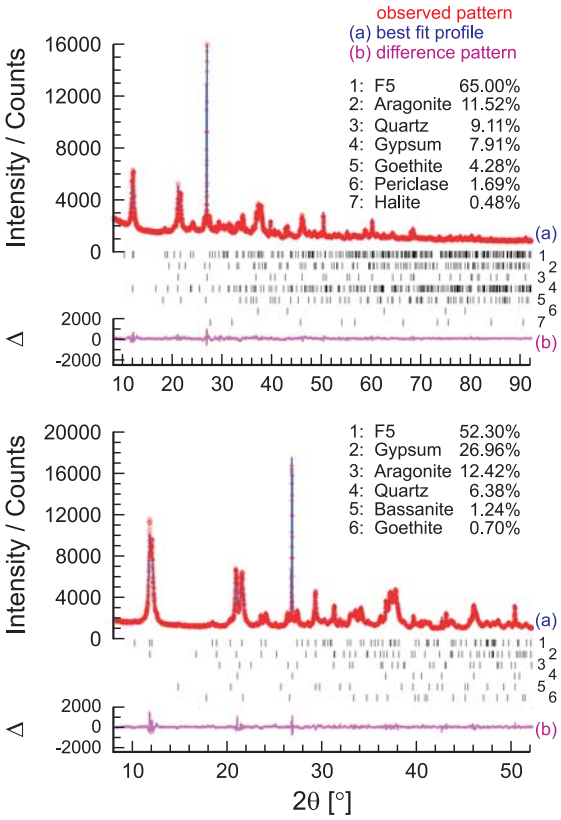

Figure 31: Rietveld plot of samples taken from the surfaces (a) of a correctly colored and (b) of a bleached yellow magnesia floor.

From Figs. 30 and 31 it is evident that the peak overlap between the F5-phase and the components responsible for damages by bleaching is severe, making the knowledge of the crystal structure of the F5-phase a prerequisite for a successful QPA. Together with the finally available crystal structure of the F5-phase, such a full quantitative phase analysis will allow an efficient quality control of Sorel cements.

[1] *Sugimoto, K., R.E. Dinnebier and T. Schlecht.* Journal of Applied Crystallography **39**, 739–744 (2006).

[2] *Sugimoto, K., R.E. Dinnebier and T. Schlecht.* Powder Diffraction **22**, 64–67 (2007).

[3] *Sugimoto, K., R.E. Dinnebier and H.C. Hanson.* Acta Crystallographica B **63**, 235-242 (2007).

Ion conduction

Transport of charge using ions as charge carriers is, besides its fundamental significance, of great importance in technical applications and devices such as chemical sensors, batteries, and fuel cells. Central issues in this field are on the one hand the development and fine-tuning of new compounds and on the other hand the multi-scale design and engineering of complex possibly hierarchical materials that can serve as efficient electrodes, conducting media or storage media. Work in this area, both on a fundamental and applied level encompassing synthesis, measurement and simulation, is a major field of research at the Institute. The three short reports presented in this section touch upon a variety of aspects involved: The use of amorphous compounds as electrode materials, the fine-tuning of ion conduction via nanosized multilayer heterostructures, and finally the development of a hierarchical network design for high-power performance in Li-based devices for energy storage and transformation.

Enhanced potential of amorphous electrode materials: Case study of RuO_2

O. Delmer, P. Balaya, L. Kienle and J. Maier

Amorphous materials are ubiquitous. Yet, their thermodynamics is still a challenge. This is particularly true for the chemical potential of the constituents of the amorphous phase. Appropriate electrochemical cells can provide a straightforward way to measure such quantities as they may convert the chemical potential into an electrical potential. Moreover, kinetically stable amorphicity can, as we show, play a beneficial role in significantly enhancing the cell voltage of batteries. As a case study, we investigate the open circuit voltage of amorphous RuO_2 in a Li cell. An excess potential of 0.6 V is observed in comparison with crystalline RuO_2 of 60 nm and 10 μm grain size [1]. As the amorphous nature stays unchanged upon lithiation and delithiation and as the electrode potential behaves reversible, the possibility of enhancing the electrode potentials by using metastable structures is indeed enticing.

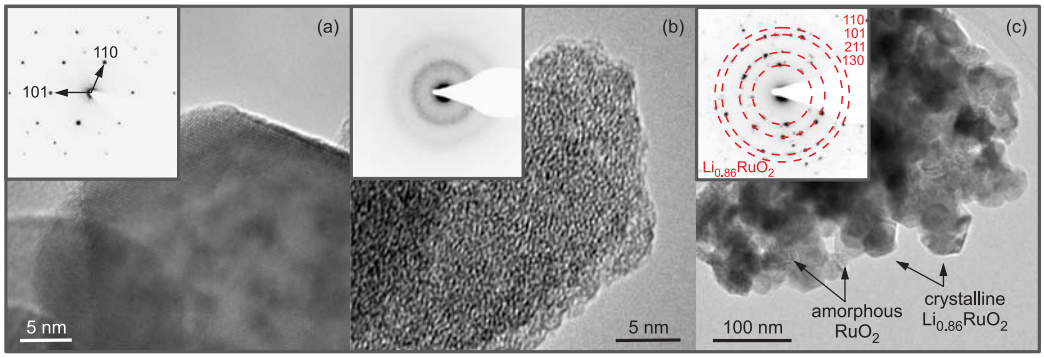

Figure 32: (a) High resolution transmission electron microscopy (HRTEM) micrograph of initial RuO_2; (b) HRTEM micrograph along with selected area electron diffraction (SAED) pattern of RuO_2 obtained by a deep discharge/charge cycle; (c) SAED pattern of the crystalline compound $Li_{0.86}RuO_2$ formed by Li insertion into amorphous RuO_2 and the corresponding HRTEM observations showing the coexistence of crystalline $Li_{0.86}RuO_2$ and amorphous RuO_2.

Amorphous RuO_2 can be easily prepared electrochemically from crystalline RuO_2 by a deep discharge/charge cycle of the pseudo-thermodynamic $(Li_x)RuO_2/LiPF_6$ + DMC + EC/Li cell.

The development of the cell voltage with time under constant current conditions shows a significantly higher cell voltage for the amorphous a-RuO_2. A clear evaluation can be made within the plateau regime where Li-saturated a-RuO_2 is in phase equilibrium with $LiRuO_2$ (more exactly $Li_{0.86}RuO_2$). It is worthy of note that $LiRuO_2$ is always crystalline (see Fig. 32(c)).

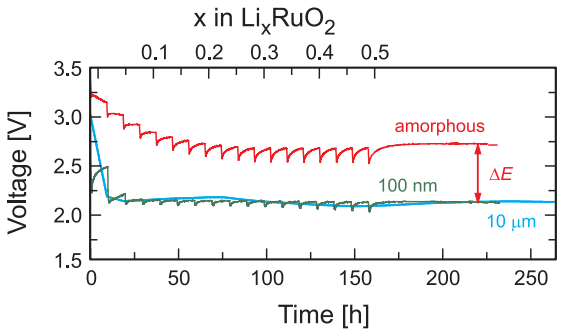

Figure 33: Time dependence of the RuO_2/Li cells with different particle sizes, measured by periodically providing current pulses.

As seen in Fig. 33 the current was after a constant discharging periodically interrupted to enable recording of the equilibration at a given composition.

The surprisingly high excess contribution of 580 mV (corresponding to an excess free enthalpy of –56 $kJmol^{-1}$) in the case of the amorphous material cannot be due to the surface contribution, but can be quantitatively understood by the loss of long range order. To show this, we approximate the measured difference in the cell voltage (ΔE) between the crystalline and amorphous state (–56 $kJmol^{-1}$) by the free enthalpy of transition from crystalline to the molten state but at the operation temperature ($\Delta_m G(T)$). Assuming enthalpy and entropy of melting to be temperature independent, we derive

$$-F \times \Delta E \approx \Delta_m G(T) \equiv \left(1 - \frac{T}{T_m}\right) \Delta H_m(T_m) \quad (5)$$

which for $T \ll T_m$ is roughly the heat of melting (F: Faraday constant).

As the melting enthalpy of RuO_2 is not available in the literature (sublimation temperature: 1200°C), we consider the melting enthalpies for isostructural TiO_2 ($T_m = 1850$°C) and VO_2 ($T_m = 1967$°C). These quantities amount to 65 $kJmol^{-1}$ and 57 $kJmol^{-1}$ [2], respectively, which indeed match our excess value of 55.9 $kJmol^{-1}$. Considering the correction ($1–T/T_m$) with $T_m \approx 2 \cdot 10^3$ K, the agreement with TiO_2 is almost perfect; in view of the approximations, however, this perfect agreement is probably just accidental.

It is very instructive to consider the value of 600 mV from the standpoint of capillary pressure of small crystalline particles. There, the excess value would stem from the Gibbs-Kelvin term, which is proportional to the ratio of the effective surface tension to the effective radius of the corresponding Wulff-shaped crystal. This would also result in a positive excess value but for nm-sized particles in values that are smaller by one order of magnitude than the value found for the amorphous material. Conversely, a value of 600 mV would be reached if the effective particle size was on the order of the interatomic distance. Bearing in mind that relevant surface tensions are on the order of melting energies, this alternative viewpoint leads to the same conclusion, namely that the enhanced chemical potential of Li in the amorphous oxide can be fully understood by the loss of long-range order.

[1] *Delmer, O., P. Balaya, L. Kienle and J. Maier.* Advanced Materials **20**, 501–505 (2008).

[2] *Barin, I.* Thermochemical data of pure compounds, WILEY-VCH, Weinheim, Germany (1989).

In-depth defect chemical analysis of mesoscopic ion conduction in nanosized CaF_2/BaF_2 multilayer heterostructures

X.X. Guo, I. Matei, J. Jamnik, J.-S. Lee and J. Maier

Ion conduction in nanometer-scale ionic systems is not only of significance for tailoring properties of devices such as chemical sensors, batteries, and fuel cells, but also of great importance from a fundamental point of view [1]. Upon introducing interfaces redistribution of ions occurs in the space-charge regions; an increased proportion of interfaces resulting from size reduction can modify not only the magnitude but also the type of conductivity. Most striking are mesoscopic situations occurring when the space-charge zones overlap [2].

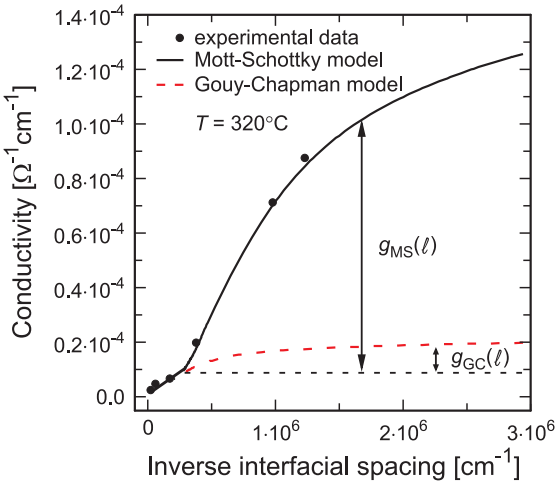

Figure 34: Calculated lateral conductivities based on the Mott-Schottky model with the mechanism of F^- transfer from one to the other phase as depicted in Fig. 35. The calculated results based on the Gouy-Chapman model are shown for comparison. $g_{MS}(\ell)$ and $g_{GC}(\ell)$ are nanosize factors in the case of Mott-Schottky and Gouy-Chapman models, respectively.

A master example in this context has been provided by the preparation of molecular-beam epitaxy (MBE)-grown CaF_2/BaF_2 multilayer heterostructures. This system which is characterized by accumulation layers of carriers forms the counterpart to nanocrystalline $SrTiO_3$ ceramics in which mesoscopic depletion governs the overall behavior [3,4]. The parallel conductivity of the heterolayers has already been explained by space charges. Yet, the striking anomalous upward-bending that occurred in the regime where space charges overlap (see Fig. 34) could not be satisfactorily interpreted. Here we report on the successful modeling including measurement and interpretation of the conductivity perpendicular to the interfaces. The approach succeeds by employing a realistic impurity distribution in a Mott-Schottky model. Measurement of conductivities perpendicular to the interfaces were achieved by using Nb-doped $SrTiO_3(100)$ substrates, which enabled growth of exclusively [111]-oriented heterolayers and exhibited negligible resistance during all the measurement.

Figure 34 shows a fit to the experimental data of the results calculated using the Mott-Schottky model with the mechanism of F^- transfer from BaF_2 to CaF_2 as depicted in Fig. 35. For the calculation, the presence of frozen donor impurities is taken into account by using a linear profile close to the interface. It can be seen that the quantitative features of the experimental data for all the layer thicknesses can be reproduced.

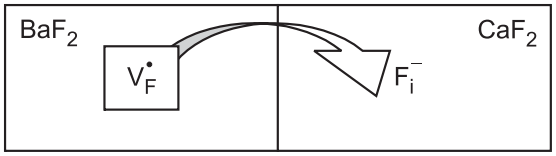

Figure 35: Schematic representation of the conduction mechanism of F^- transfer from BaF_2 to CaF_2.

It is worth being mentioned that the striking effect of upward-bending is not the result of assuming a special impurity profile. The additional enhancement due to overlap is given by the nanosize factor $g_{MS}(\ell)$, which can also be numerically calculated and approximately equals $2\lambda^\star/\ell$, where $\lambda^\star$ and ℓ are the effective space-charge thickness and the interfacial

spacing, respectively. The space charge potential that we derive from the ℓ-dependence agrees well with the one determined from the T-dependence.

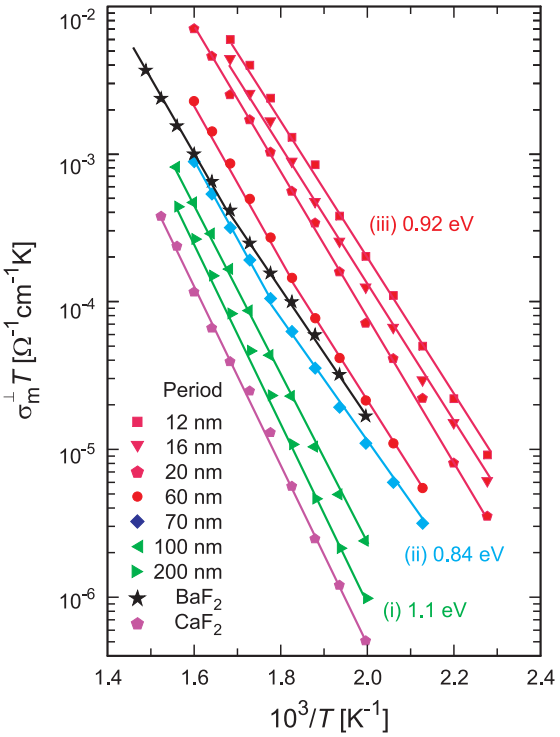

Figure 36: Perpendicular ionic conductivity of the heterolayers with various periods ranging from 12 nm to 200 nm compared to the homogenous CaF_2 and BaF_2 films of 400 nm thickness. The overall thickness is approximately the same for all the samples ($\approx$ 400 nm). The different colours refer to different size regimes.

In contrast to the parallel conductivities determined by the conduction parts along the interfaces, the conductivities perpendicular to the interfaces reflect the more resistive bulk. This should prove useful in terms of a mechanistic interpretation. Measured conductivities perpendicular to the interfaces are shown in Fig. 36. As regards the activation energies, the progressive increase of the conductivities with decreasing layer thickness can be classified into three regimes: (i) For $\ell > 50$ nm, CaF_2 bulk is decisive. (ii) For 30 nm $< \ell <$ 50 nm, fluoride interstitials in both materials dominate the overall conduction. (iii) For $\ell < 30$ nm, fluoride interstitials in CaF_2 play an important role due to a close-to-interface situation. These results are in good agreement with the thickness dependence of resistance calculated on the basis of carrier concentration profiles derived from the parallel conductivities.

As we now have an extremely accurate understanding of the behavior on the phenomenological level, we are prepared for the next step of the analysis, namely the explanation of the detailed reason for the sign (direction) and magnitude (space charge potential) of the F^- transfer required as a consequence of contact equilibrium. For that purpose information about the individual defect formation parameters in both CaF_2 and BaF_2 is required for whose elucidation we need assistance from atomistic simulation.

[1] *Maier, J.* Nature Materials **4**, 805–815 (2005).

[2] *Maier, J.* Physical Chemistry of Ionic Materials Ions and Electrons in Solids, Wiley, Chichester (2004).

[3] *Balaya, P., J. Jamnik, J. Fleig and J. Maier.* Applied Physics Letters **88**, 062109 (2006).

[4] *Sata, N., K. Eberl, K. Eberman and J. Maier.* Nature **408**, 946–949 (2000).

Hierarchical mixed conducting networks for rapid lithium storage

Y.-S. Hu, Y.-G. Guo and J. Maier

Storage and transformation of energy by electrochemical means is one of the basic themes of future energy research. In this context Li-based batteries are in the focus of interest owing to significant energy densities (per mass). As to an increase of power density and storage capacity at high currents the use of nanosized particles is advantageous. There are several ways in which size affects performance: Most striking are effects in which local transport or storage parameters are influenced by the presence of interfaces or even by confinement [1]. Beyond that there is the possibility of reduction of transport path lengths. This is particularly important as regards the relaxation time of Li-storage in electrodes. Unlike the electrical case in which both conductances and capacitances scale with $1/L$ (L: thickness), hence leaving the relaxation time ($R{\cdot}C$) invariant, in the storage case the chemical capacitance scales with L leading to a waiting time that is proportional to L^2. Given a diffusion coefficient below $10^{-10}\,\mathrm{cm^2/s}$, which is typical for room temperature, a sample of 1 mm thickness needs many years to be filled with Li, i. e. with Li^+ and e^-. This waiting time is reduced to less than a second for nanometer dimensions, however. Some materials even may appear not to be electroactive at all just because of sluggish diffusion. Recently we showed that rutile which was believed not to be able to store lithium can take up substantial amounts of Li if present in nanosize [2]. On a nanoscale it is fine-structured analogously: Electrolyte penetrates the mesopores which are now also metallized. The use of such a hierarchical structure is very beneficial for quick infiltration.

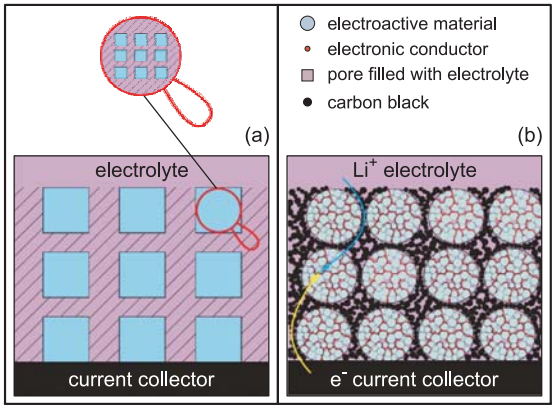

Figure 37: 'Self-similar' mixed conducting 3D networks on nanoscale and microscale level.

As Li-diffusion requires ambipolar transport of Li^+ and e^-, it does not suffice to let the liquid electrolyte penetrate but also the electronic availability has to be guaranteed. Figure 37 shows our solution to this problem. The material to be inserted is, on a macroscopic scale, embedded in a mixed conducting matrix (here simply electrolyte plus carbon admixture). Then, on the nanoscopic level deliberate metallization of the nanopores is necessary which we achieved via RuO_2 precipitation.

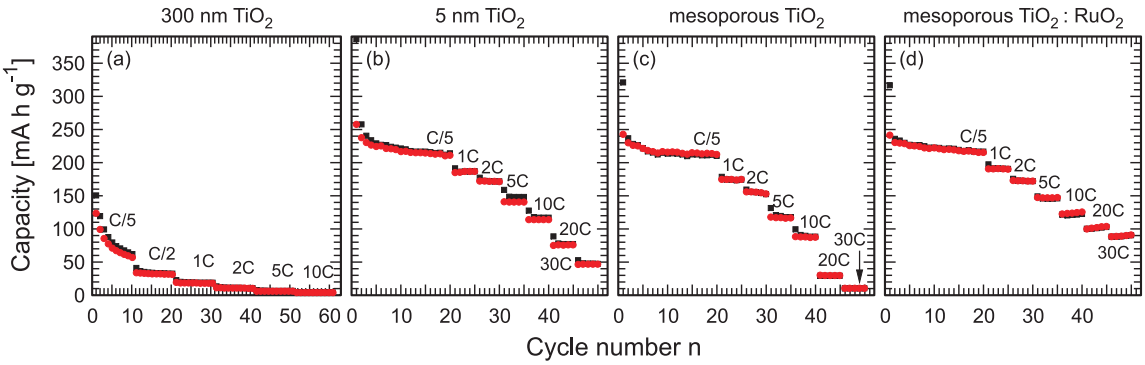

Figure 38: Anatase: cycling and rate performance: (a) Micro-TiO_2; (b) 5 nm-TiO_2; (c) Mesoporous TiO_2; (d) Mesoporous $TiO_2 : RuO_2$.

The metallization is not necessary if a conductive electrode such as carbon is used, i.e., hierarchical mesoporous carbon structures lead to an excellent performance even at high currents [3]. If, however, electrically insulating oxides are used this point proves crucial.

Figure 38(a), (b), (c) shows the beneficial effect of sheer size reduction for anatase at low rates. But it also shows how rapidly the performance decays at high rates where the availability of the electrons becomes a problem. Our solution [2], however, now provides a huge capacity increase at very high rates as seen from Fig. 38(d).

Similarly striking are our results for $LiFePO_4$ [4]. Addition of only a few percent of RuO_2 leads to a substantial capacity even at rates high enough to achieve discharge of the full theoretical capacity within a few minutes. In this case RuO_2 – obviously due to its very good wetting properties with respect to oxidic electrodes – complements the insufficient carbon network. We believe that the simple design is optimal to achieve high power performance in electrode materials with sluggish transport properties.

[1] *Maier, J.* Nature Materials **4**, 805–815 (2005).

[2] *Hu, Y.-S., L. Kienle, Y.-G. Guo and J. Maier.* Advanced Matererials **18**, 1421-1426 (2006).

[3] *Hu, Y.-S., P. Adelhelm, B. Smarsly, S. Hore, M. Antonietti and J. Maier.* Advanced Functional Materials **17**, 1873–1878 (2007).

[4] *Hu, Y.-S., Y.-G. Guo, R. Dominko, M. Gaberscek, J. Jamnik and J. Maier.* Advanced Materials **19**, 1963–1966 (2007).

Organic and carbon-based materials

Organic and carbon-based materials have been a mainstay of chemistry since the 19th century. Considering the fact that only a few types of atoms are at the heart of this branch of chemistry, it is perhaps surprising that recent years have seen great success in the development of new classes of materials in this field. This holds true even in areas such as semi- and superconductors or mechanically strong materials, where one had become accustomed to encountering only classical inorganic compounds. Research efforts in many groups at the Institute are devoted to the synthesis, analysis and application of materials such as carbon nanotubes, graphene, fullerenes, organic-inorganic hybrid compounds, just to name a few. In this section, a few examples are presented. Three are drawn from the area of thin films and surfaces: An in-depth study of the growth of graphene on SiC-surfaces, the demonstration of genuine metal-organic coordination interactions in supramolecular networks on metal surfaces, and the development of thin-film low-voltage organic transistors and circuits. The other studies deal with various properties and applications of carbon nanotubes, such as their use for the purpose of microwave attenuation, the construction of transparent conducting films and transistors, and their potential employment as a platform for spatially localized single molecule detection with the aid of Raman spectroscopy.

Evolution and structure of graphene layers on SiC(0001)

C. Riedl and U. Starke; J. Bernhardt, M. Franke and K. Heinz (Universität Erlangen)

The physics of graphene attracts tremendous interest due to its unconventional two-dimensional electron gas and electron transport properties [1]. Micron-sized flakes of single layer graphene could be prepared recently by micromechanical cleavage of graphite [1]. For practical electronic applications the epitaxial growth of graphene on SiC surfaces by thermal composition of the topmost SiC layers is a very promising approach [2]. Graphene properties appear when on top of a first carbon buffer layer with a $(6\sqrt{3}\times6\sqrt{3})R30^\circ$ superlattice a second carbon layer has grown. However, it is unclear, under which preparation conditions homogeneous large-area graphene layers can be obtained, and what the atomic structure of the interface and the graphene layer is. The present research report describes the structure of the graphene-SiC(0001) interface and the evolution of graphene layers on top of it [3].

Samples were cut from 4H-SiC(0001) wafers and hydrogen etched in order to obtain atomically flat and chemically passivated terraces. In ultrahigh vacuum (UHV) the samples were then prepared by Si deposition and annealing. The surfaces were characterized using low-energy electron diffraction (LEED) and scanning tunneling microscopy (STM). Three different procedures were applied for graphitization: (a) after annealing the sample at 800° in Si-flux and retrieving the Si-rich (3×3) reconstruction, the C-rich $(6\sqrt{3}\times6\sqrt{3})R30^\circ$ reconstruction can be obtained by annealing without further Si addition to about 1250°. (b) As a second method the $(\sqrt{3}\times\sqrt{3})R30^\circ$ Si-adatom reconstruction phase can be obtained directly by annealing the sample at 950° under simultaneous Si deposition. By heating of this surface without further Si deposition graphitization can be realized. (c) Finally, annealing of the hydrogen etched sam-

ple immediately leads to the $(6\sqrt{3}\times6\sqrt{3})$R30° phase. In each case graphene layers develop at higher temperatures. As deduced from the LEED images in Fig. 39 all three preparation procedures lead to a $(6\sqrt{3}\times6\sqrt{3})$R30° periodicity. Yet, a detailed inspection of the spots in the vicinity of the $\frac{1}{3}$ diffraction order (see enlargements) reveals a more complex scenario.

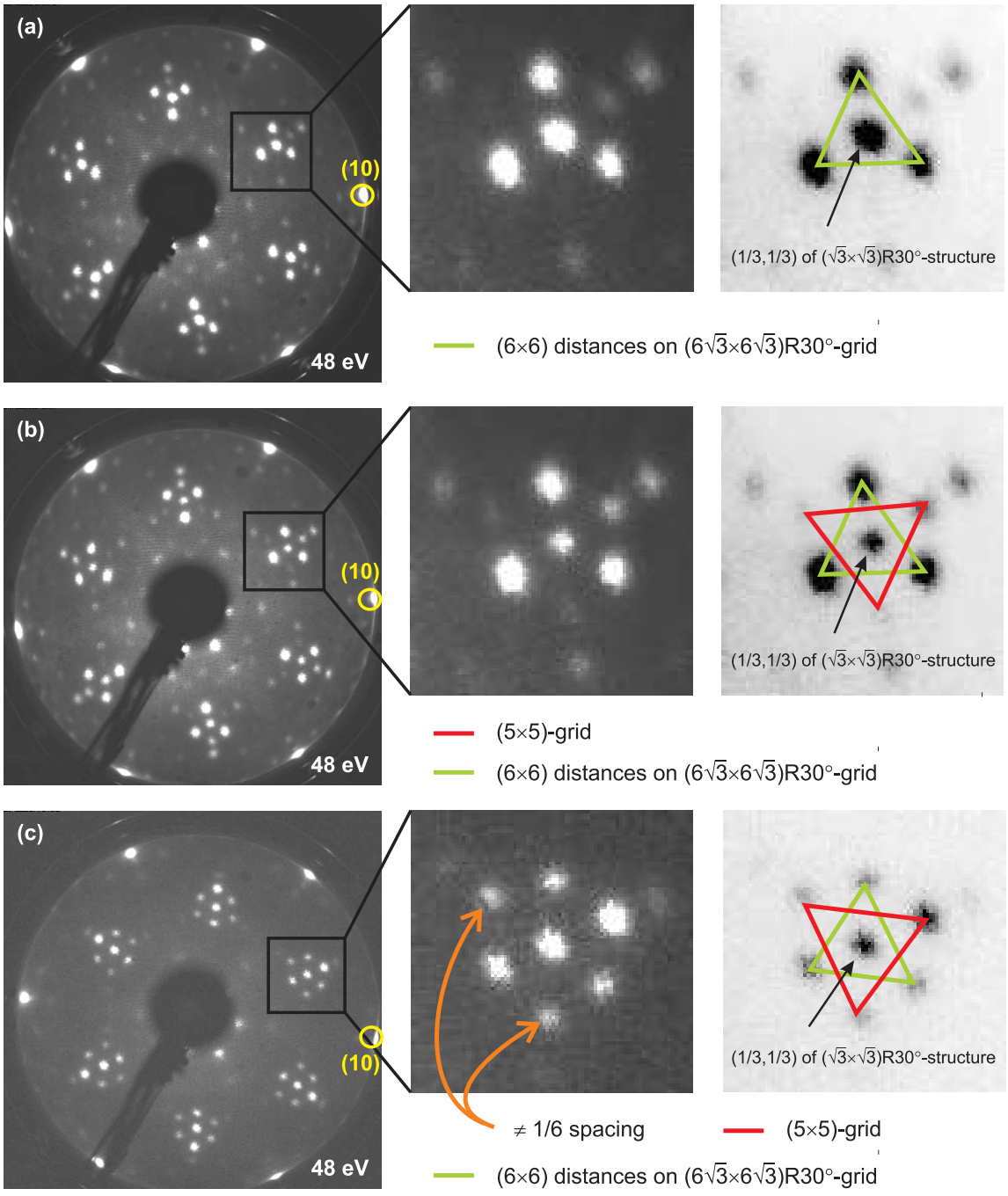

Figure 39: LEED patterns of mixed $(\sqrt{3}\times\sqrt{3})$R30° and $(6\sqrt{3}\times6\sqrt{3})$R30° reconstruction of 4H-SiC(0001) for three different preparation procedures labeled a, b and c as described in the text, after annealing at a temperature of about 1200°. Spots on a $(6\sqrt{3}\times6\sqrt{3})$R30° grid as well as on a (5×5) grid can be observed exhibiting different relative intensities.

The spot indicated by the arrow in the reverse contrast image is a $(\frac{1}{3},\frac{1}{3})$-spot which results from the $(\sqrt{3}\times\sqrt{3})$R30° phase still present on the surface at this stage. The spot actually disappears with increasing temperature as the corresponding $(\sqrt{3}\times\sqrt{3})$R30° domains disappear, too. The spots on the triangle marked in green have distances of $\frac{1}{6}$ of the substrate's reciprocal surface unit vector. However, since the $(\frac{1}{3},\frac{1}{3})$ position in the center of the triangle is part of a (6×6) grid on the SiC(0001) surface, it is clear that the spots on the green triangle are shifted with respect to the (6×6) grid and belong to a true $(6\sqrt{3}\times6\sqrt{3})$R30° grid which proves that the surface is not of (6×6) periodicity as it is often assumed from the (6×6) corrugations that can be observed in STM (see below). However, some of the diffraction spots in the LEED pattern are not precisely positioned on the $(6\sqrt{3}\times6\sqrt{3})$R30° grid, namely the spots indicated by the triangles marked in red in panels (b) and (c). These spots have a larger distance than the spots on the green triangle and do not belong to the $(6\sqrt{3}\times6\sqrt{3})$R30° grid. They rather have to be attributed to a (5×5) grid as was confirmed from LEED data at different energies. Apparently, the detailed preparation procedure for the $(6\sqrt{3}\times6\sqrt{3})$R30° phase can strongly influence their quality and atomic structure.

The role of the (5×5) periodicity in the different preparation procedures can be elucidated using STM. Figure 40(a) shows a filled state STM image of the $(6\sqrt{3}\times6\sqrt{3})$R30° reconstruction exhibiting two different periodicities, a (6×6) honeycomb structure on the left side and a (5×5) structure on the right side of the panel. The (5×5) structure is characterized by clusters with a varying number of atoms as also previously reported. We observe this structure for all three preparation procedures independent of the annealing temperature of the $(6\sqrt{3}\times6\sqrt{3})$R30° reconstruction. Only the number and fraction of (5×5) domains is larger for the ex situ prepared sample (procedure c), in full agreement with the stronger intensity level of the (5×5) LEED spots.

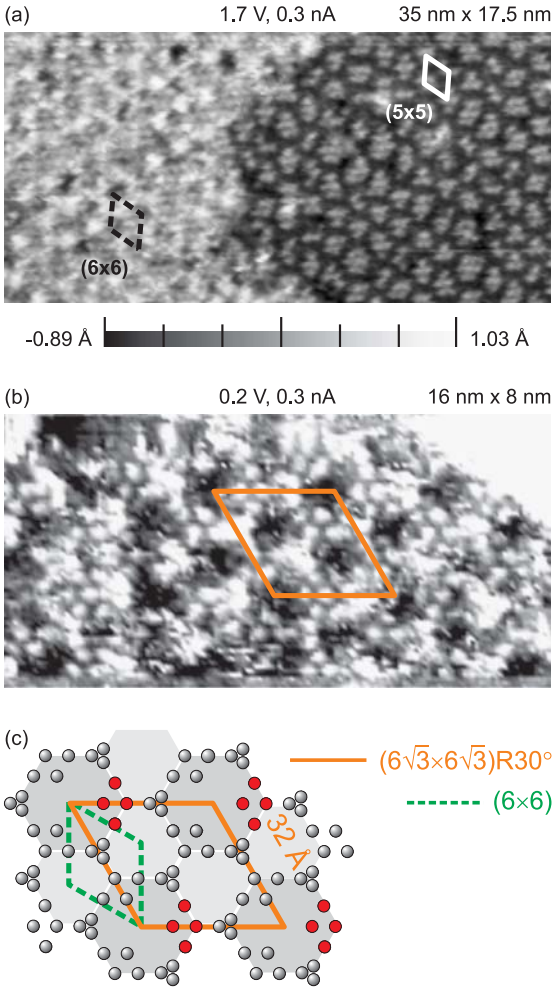

Figure 40: (a) STM image of the $(6\sqrt{3}\times6\sqrt{3})$R30° on 4H-SiC(0001) with coexisting (6×6) corrugations (left side) and (5×5) corrugations (right side). (b) STM image at $U_{tip} = 0.2$ V of an area with (6×6) corrugation with two rings of adatoms of two different sizes resolved thus defining the $(6\sqrt{3}\times6\sqrt{3})$R30° unit cell. (c) Sketch of the atoms or atomic clusters together with the corresponding unit cells.

A closer inspection of the (6×6) corrugated patches (see also Fig. 41(a)) demonstrates the complexity of the reconstruction. Different apparent features can be seen that lack an obvious long-range order. Yet, the structural appearance of the surface strongly depends on the tunneling voltage. The (6×6) periodicity is mainly pronounced at high tunneling bias whereas at low bias it is difficult to observe a clear long range periodicity. Using such small tunneling voltages, however, one can partially

resolve the true $(6\sqrt{3}\times6\sqrt{3})$R30° structure. As shown in Fig. 40(b), a tunneling voltage down to 0.2 V reveals two types of rings with slightly different sizes which form a unit cell of $(6\sqrt{3}\times6\sqrt{3})$R30° periodicity. Three atomic bumps within the rings are only present in the larger rings. Each bump is part of a diamond of four atoms which, in the same orientation, is repeated only with the $(6\sqrt{3}\times6\sqrt{3})$R30° periodicity. This is elucidated in panel (c) by a sketch of the rings with their different size and the three additional atoms (or atomic clusters) with the (6×6) and the $(6\sqrt{3}\times6\sqrt{3})$R30° unit cells indicated. With this real space arrangement the periodicity of the LEED patterns can be explained which is not possible assuming a (6×6) structure only. These findings invalidate other models that rule out the $(6\sqrt{3}\times6\sqrt{3})$R30° structure as an inherent surface reconstruction of SiC(0001) [3]. The proposed coexistence of a (6×6) and an incommensurate $(\sqrt{2.1}\times\sqrt{2.1})$R30° phase is not in agreement with the interpretation of our LEED and STM results. The interpretation as a Moiré pattern of graphite and the SiC substrate is inconsistent with both band structure measurements and the STM images (Fig. 41(b)), and a recently proposed model suggesting a self-organized 'carbon nanomesh' with (6×6) periodicity is also in contradiction to the band structure measurements and the bias dependence of our STM images. Nevertheless, the fact that this complex phase is only partially understood by now shows the need for a structure determination, e.g., by means of quantitative LEED.

The development of graphene layer(s) requires further annealing at even higher temperatures. However, even when starting from a surface with the apparently best $(6\sqrt{3}\times6\sqrt{3})$R30° structure (from procedure a), many steps and terraces with different configuration are observed. Contrast changes obviously indicate a different number of graphene layers [3]. However, graphene layers can also be directly identified as shown in Fig. 41 where the sample was annealed to around 1300°. For two different tip conditions we compare images of the same surface area with two different terraces. The first tip condition allows for atomic resolution of the $(6\sqrt{3}\times6\sqrt{3})$R30° reconstruction, the second one seems to allow only for a reduced quality at a first glance. However, scaling down the scanning area leads to atomic resolution of the graphene on top of the $(6\sqrt{3}\times6\sqrt{3})$R30° surface reconstruction, but only on the region with the reduced contrast. The unit cell size of about 2.5Å clearly corresponds to graphite, and since we observe only one of the two carbon atoms in the graphene unit cell we can identify this surface region as (at least) bilayer graphene, since the Bernal stacking of two graphene sheets leads to the observation of such a diamond-shaped lattice.

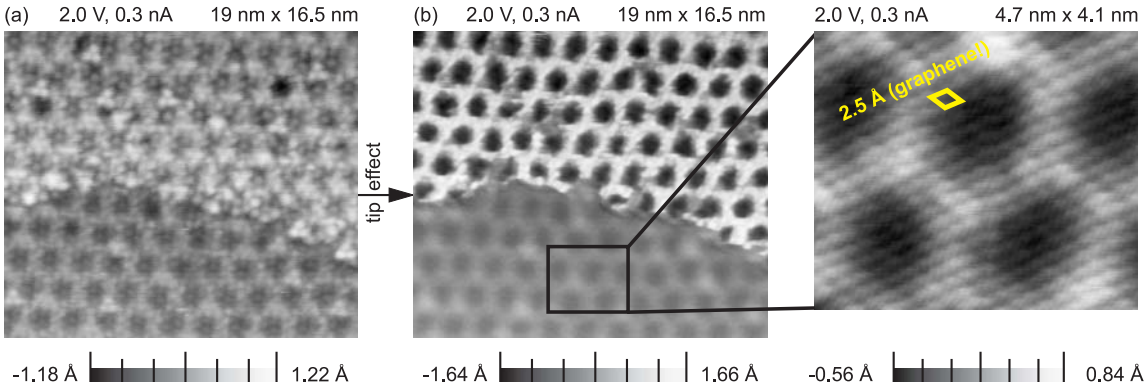

Figure 41: Atomically resolved STM images of the $(6\sqrt{3}\times6\sqrt{3})$R30° reconstruction on 4H-SiC(0001) showing (6×6) corrugations with two different contrasts for two different tip conditions shown in panel (a) and panel (b). Only for the tip condition in panel (b) graphene on top of the $(6\sqrt{3}\times6\sqrt{3})$R30° reconstruction can be resolved (lower part of the STM image). The annealing temperature was around 1300°.

The crucial point that should be emphasized is that the visibility of the graphene layers strongly depends on the actual tip condition thus complicating the determination of the number of graphene layers by means of STM. In the upper part of Fig. 41 the higher contrast in the STM image represents a lower coverage with graphene, possibly no graphene layer at all. However, it cannot be ruled out that a single graphene layer might possibly be identified using a different bias voltage.

The controlled, homogeneous preparation of a certain number of graphene layers remains a problem. And in this context it would be desirable to find an easy and exact way for the determination of the number of graphene layers that can be used in the home laboratory and, in particular, continuously during the preparation procedure. We can show that LEED intensity spectra, which can be obtained in the same UHV chamber, have the potential to be used as fingerprints and so offer a solution to this problem [3]. When graphene layers are growing on top of the pure $(6\sqrt{3}\times6\sqrt{3})$R30° structure (above 1300°) a LEED spot with a distance that is related to that of bulk graphite shows an increasing intensity. Simultaneously, the diffuse background in the LEED patterns continuously increases, while STM still shows a good quality $(6\sqrt{3}\times6\sqrt{3})$R30° reconstruction. The graphite related spot is positioned next to the $(\frac{2}{3},\frac{2}{3})$ spot of the substrate with a $1/(6\sqrt{3})$ distance. It has to be pointed out that this LEED spot already belongs to the $(6\sqrt{3}\times6\sqrt{3})$R30° reconstruction and can also be observed before any graphene layers are grown. This spot shows significant changes in the peak shape and peak position of its intensity spectra that have the potential to be used to identify the graphene thickness [3]. The upcoming task is to exactly correlate the LEED $I(E)$-spectra characteristics with a certain number of graphene layers. For this purpose we are currently acquiring the LEED fingerprints in an in situ combined experiment with the band structure from angle-resolved photoelectron spectroscopy (ARPES), where the identification of the number of layers seems possible. In parallel, we attempt a direct structural correlation by a quantitative LEED analysis, which may not resolve the complete surface structure but might give partial insight into the structural development of the surface before and during the graphitization process, and thus help to define more precise preparation conditions.

[1] *Geim, A.K. and K.S. Novoselov.* Nature Materials **6**, 183–191 (2007).

[2] *Berger, C., Z. Song, X. Li, X. Wu, N. Brown, C. Naud, D. Mayou, T. Li, J. Hass, A.N. Marchenkov, E.H. Conrad, P.N. First and W.A. de Heer.* Science **312**, 1191–1196 (2006).

[3] *Riedl, C., U. Starke, J. Bernhardt, M. Franke and K. Heinz.* Physical Review B **76**, 245406 (2007).

Metal-organic coordination interactions in supramolecular networks on Cu(100)

S.L. Tait, G. Costantini, Y. Wang, N. Lin and K. Kern; A. Baraldi (Trieste University); F. Esch (Laboratorio TASC INFM-CNR, Trieste); L. Petaccia and S. Lizzit (Sincrotrone Trieste, Italy)

Supramolecular self-assembly is a strategy of growing interest for efficient and uniform patterning of surfaces with periodic nanometer-scale structures [1]. Effective assembly requires intercomponent interactions that provide structural stability, but are also sufficiently labile to allow error correction during growth. Metal-organic mixtures at surfaces have been demonstrated to form highly ordered, two-dimensional (2D) networks at metal surfaces [2]. It has been postulated that these architectures are mediated by metal–organic coordination, analogous to that which occurs in 3D solution-based chemistry. However, conclusive evidence for genuine metal–organic coordination in these networks at surfaces has been lacking.

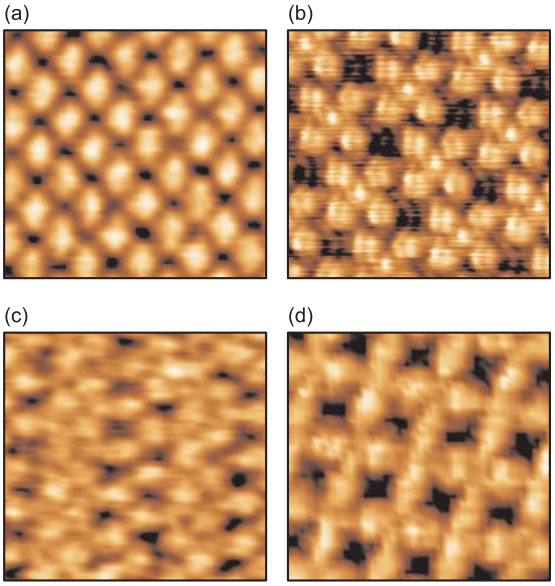

Figure 42: STM images of TPA–Fe coordination networks at Cu(100). (a) Pure TPA layer forming a dense 3×3 structure. (b) Fe:TPA in 1:4 ratio, forming coordination units consisting of four TPA molecules coordinated around each Fe center. (c) and (d) show structures which occur at higher Fe:TPA ratios. Scan area $5\,\text{nm} \times 5\,\text{nm}$ for each panel. STM results by Lingenfelder *et al.* [2].

Using the X-ray photoelectron spectroscopy (XPS) capabilities at the ELETTRA SuperESCA beamline, we demonstrate that a genuine coordination interaction does exist in these systems, evidenced as distinct shifts in the O 1*s* and Fe 3*p* core level spectra [3]. The XPS experiments were correlated with high-resolution scanning tunneling microscopy (STM) measurements. Mixtures of terephthalic acid (TPA) with Fe atoms, sequentially evaporated onto Cu(100) in UHV and annealed at 410 K, form highly ordered networks, as demonstrated by STM [2]. Several network structures can be produced, depending on the Fe:TPA number ratio, χ. In Fig. 42 are highly ordered pure TPA structures ($\chi = 0$) which have a 3×3 periodicity relative to the substrate lattice (a), Fe–TPA 'cloverleaf' structure for $\chi = 0.25$ with 6×6 periodicity (b), and other two-dimensional coordination structures with $\chi = 0.66$ (c) and $\chi = 1.0$ (d).

X-ray photoelectron spectra resolve electron core level energy shifts due to changes in the local chemical environment of specific species. Figure 43(a) displays five O 1*s* spectra from a single sample with an initial TPA deposition (bottom curve) and subsequent, step-wise Fe depositions. The curves are labeled by the estimated Fe:TPA number ratio, χ. The spectrum for the pure TPA sample ($\chi = 0$) exhibits a single feature for O in the carboxylic functional groups. All of the carboxylic groups of the TPA molecules have deprotonated, therefore the O atoms are in an identical chemical environment. Based on STM measurements (Fig. 42(a)), it is believed that these are involved in hydrogen bonding interactions with neighboring molecules to stabilize a well-ordered 3×3 layer.

With increasing Fe (moving up in Fig. 43(a)), a second O 1*s* feature appears corresponding to molecules which have formed coordination bonds with Fe atoms. The total O 1*s* area is constant but the area fraction in the 'coordinated' peak increases linearly with χ.

Evidence for Fe–TPA coordination is also clear from the behavior of the corresponding Fe 3*p* spectra presented in Fig. 43(b) (low intensity due to low absolute coverage of Fe). The Fe 3*p* feature for a pure metal film (not shown) is fit well by a double peak feature at 52.8 eV and 52.0 eV (marked in Fig. 43(b)). In the TPA–Fe experiment we observe an Fe 3*p* feature at 2.1 eV higher binding energy, attributed to Fe atoms involved in coordination bonding with the organic ligands. With increasing Fe coverage, this feature increases in intensity, but does not move in energy, demonstrating a well-defined oxidation state for the coordinated Fe atoms. The magnitude of the observed chemical shift of the Fe core level energy is consistent with that observed for iron oxides in a +2 oxidation state. However, this similarity in the core-level shift does not necessarily imply an identical chemical environment, due to the presence of the metallic substrate.

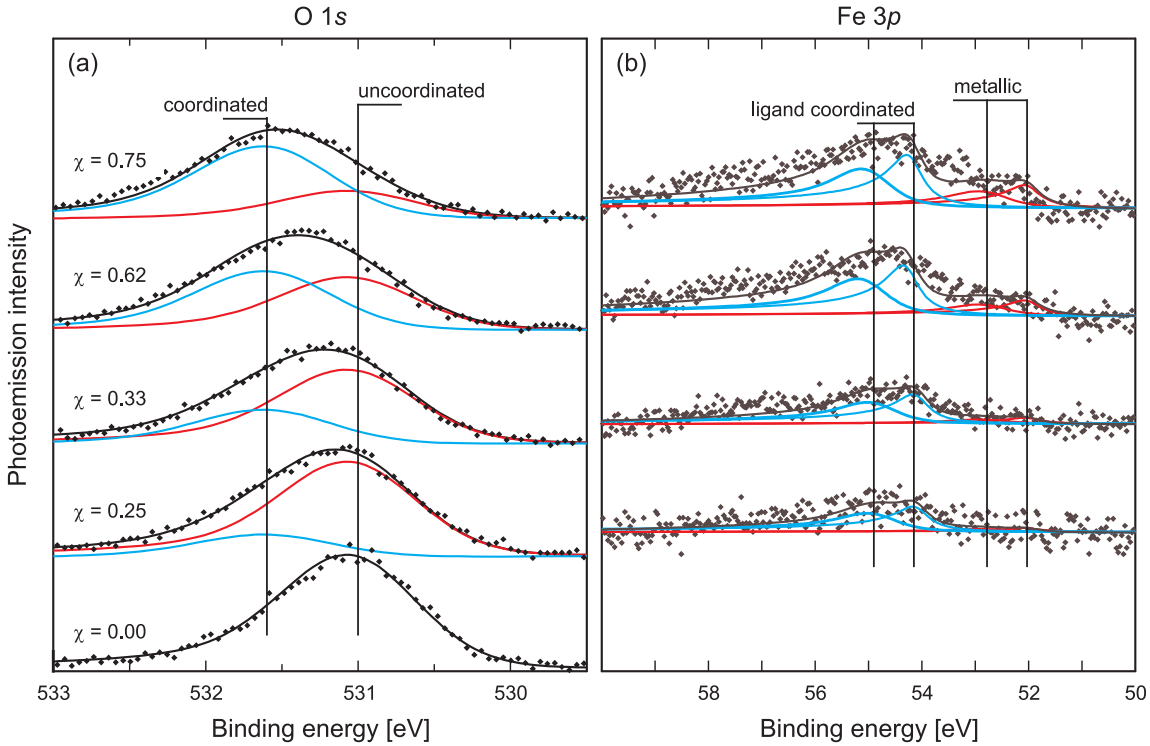

Figure 43: XPS spectra demonstrating genuine Fe–TPA coordination interactions at Cu(100), evident in (a) O 1*s* and (b) Fe 3*p* core level spectra. Spectra are shown for several values of the Fe:TPA number ratio, χ, increasing moving up the figure. Features in each panel are observed for coordinated (blue, 531.6 eV, 54.9 eV, 54.1 eV) and uncoordinated (red, 531.0 eV, 52.8 eV, 52.0 eV) components. Modified from [3].

These XPS results provide chemical resolution of the interactions which stabilize the highly ordered nanometer-scale networks observed by STM. The measurements clearly demonstrate that the mixing of TPA and Fe on the Cu(100) surface has a strong impact on the Fe electronic core levels, indicating a significant electronic interaction between the Fe centers and the TPA molecules. Electron core level binding energy shifts in the O 1*s* peaks with increasing Fe exposure show that these interactions occur through Fe–O coordination at the deprotonated carboxylate groups, consistent with STM results. These results demonstrate that in Fe–TPA supramolecular assemblies at Cu(100), genuine coordination bonding with a specific chemical state exists, analogous to the interactions stabilizing solution-based coordination architectures.

[1] *Barth, J.V., G. Costantini and K. Kern.* Nature **437**, 671–679 (2005).

[2] *Lingenfelder, M.A., H. Spillman, A. Dmitriev, S. Stepanow, N. Lin, J.V. Barth and K. Kern.* Chemistry – A European Journal **10**, 1913–1919 (2004).

[3] *Tait, S.L., Y. Wang, G. Costantini, N. Lin, A. Baraldi, F. Esch, L. Petaccia, S. Lizzit and K. Kern.* Journal of the American Chemical Society **130**, 2108–2113 (2008).

Low-voltage organic transistors and circuits with improved stability

H. Klauk, U. Zschieschang, R.T. Weitz, F. Ante and D. Kälblein

Flexible thin-film transistors based on room-temperature-processable organic semiconductors first emerged in the late 1980s as somewhat of a laboratory curiosity. The subject of an ever-growing world-wide research effort for 20 years, organic transistors are now beginning to make their way into consumer products. First to market will be the Readius, a digital mobile device with a 5-inch foldable active-matrix display enabled by 76800 pentacene transistors (see Fig. 44(a)). The Readius, which is scheduled to go into mass production in 2008, is expected to be followed by an A5-size flexible electronic newspaper device that utilizes more than one million polymer transistors (see Fig. 44(b)). Both devices have been developed and will be manufactured in Europe.

Next-generation flexible devices based on organic thin-film transistors will likely feature increasingly larger displays with higher resolution, brighter colors, and more and more additional functions. This will translate into increasing power consumption, and much like today's mobile phones and laptop computers, future flexible-display devices will either suffer from limited battery life or will require larger, heavier, more expensive battery packs.

One reason for this is that the transistors that drive each of the many pixels in an active-matrix display typically require operating voltages in the range of 10 V to 20 V. To alleviate the power problem we are developing organic transistors that can be operated with much lower voltages of only 2 V to 3 V. The key innovation to enable low-voltage thin-film transistor operation is a very thin gate dielectric that is based on a combination of an oxygen-plasma-grown aluminum oxide layer and a solution-processed molecular self-assembled monolayer. Both layers are prepared at room temperature, so that the transistors are suitable for flexible polymeric substrates.

Figure 44: Left: The first consumer product that employs organic transistors is the Readius developed by Polymer Vision and expected to become available in 2008 (www.polymervision.com). Right: Plastic Logic is developing an electronic newspaper device enabled by more than one million polymer transistors on a flexible substrate (www.plasticlogic.com).

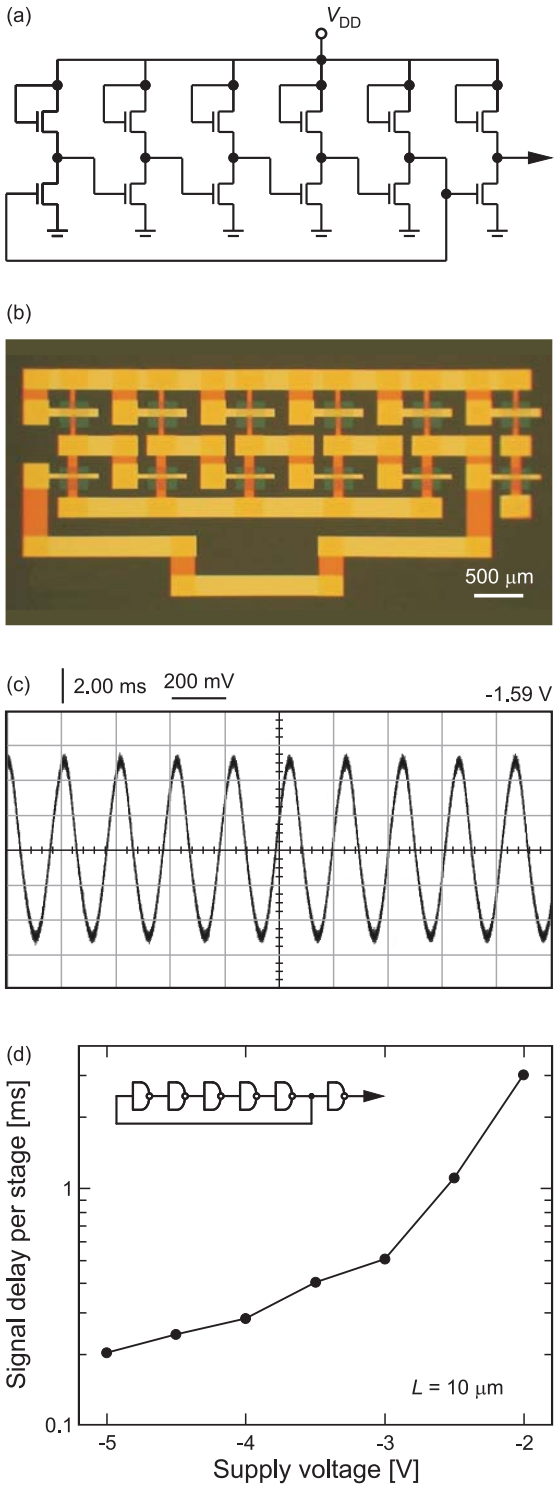

Figure 45: Characteristics of a low-voltage pentacene 5-stage ring oscillator. The drive TFTs have a channel length of 10 μm and a channel width of 100 μm, the load TFTs have a channel length and width of 50 μm.

The total dielectric thickness is only about 6 nm, so that a gate voltage of only 2 V to 3 V is sufficient to induce a carrier channel in the organic semiconductor. Most importantly, owing to the high quality of the self-assembled monolayer, the leakage currents through these ultrathin gate dielectrics are very small, less than $10\mu A/cm^2$ at 3 V. Consequently, organic transistors with ultrathin gate dielectrics based on self-assembled monolayers are well-suited for low-voltage flexible electronic applications [1]. Figure 45 summarizes our recent results on organic integrated circuits based on low-voltage pentacene transistors. Our inverters show sharp switching with rail-to-rail output swings and negligible hysteresis. Ring oscillators operate with supply voltages between 2 V and 5 V and with a minimum signal propagation delay of 200 μs per stage [2].

A commonly encountered problem with organic transistors is their limited stability when operated or stored in air. This limited stability is most likely caused by the diffusion of oxidizing species, such as water, oxygen, or ozone into the organic films. In principle, this problem can be eliminated by encapsulating the transistors, but from a manufacturing cost perspective it is more desirable to develop organic semiconductors that are less sensitive to oxidation. A promising strategy to the development of air-stable organic semiconductors is the synthesis of conjugated compounds with a larger ionization potential, i.e., with a smaller conjugated core. However, a smaller conjugated core will also lead to poor molecular ordering in thin films, and this will reduce the carrier mobility of the semiconductor. One solution is the synthesis of molecules that consist of several small conjugated cores separated by vinyl groups. Such molecules have a larger ionization potential and thus better stability compared with molecules with just one large conjugated core, but they facilitate a similar degree of molecular ordering and thus are expected to provide similar carrier mobility [3].

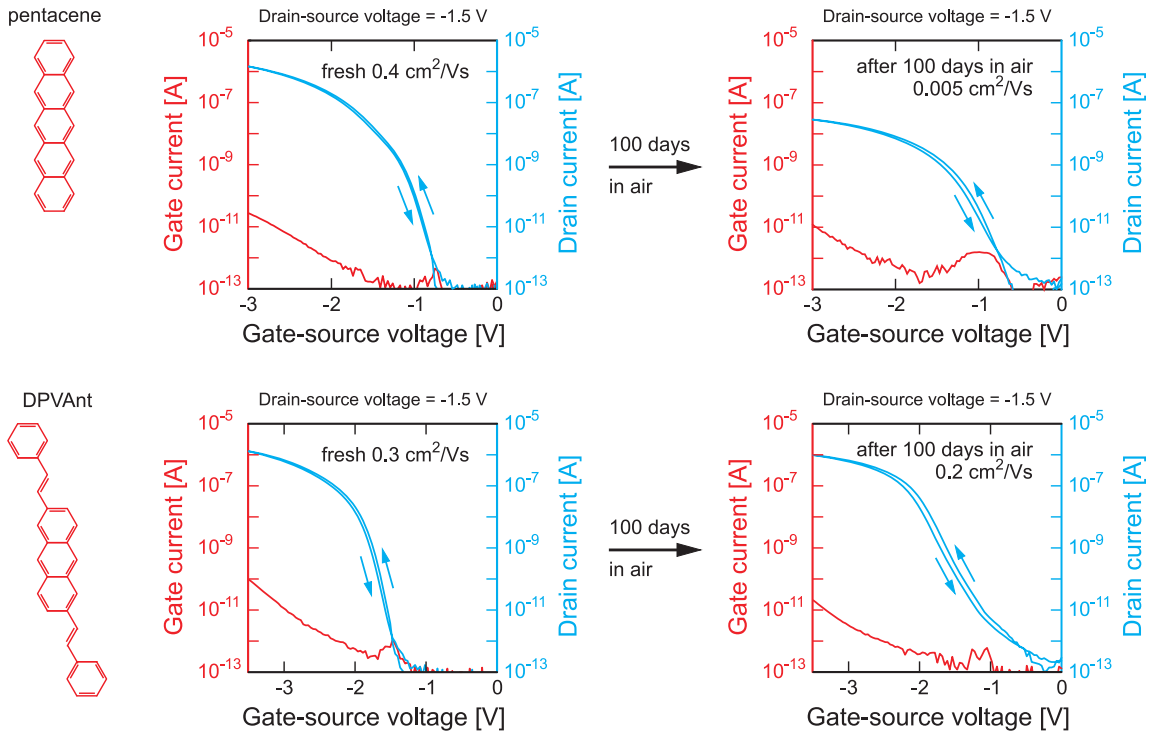

Figure 46: Compared with pentacene transistors (a), transistors using the newly synthesized di(phenylvinyl)anthracene have similar carrier mobility, but show much less rapid degradation when exposed to air (b). This is due to the molecular structure in which three smaller conjugated cores are separated by vinyl groups.

An example for this new approach is shown in Fig. 46. As can be seen from Fig. 46(a), the mobility of a transistor based on pentacene (a commercially available semiconductor with a single large conjugated core) degrades rapidly when the transistor is exposed to air. After 100 days in air the mobility has decreased from 0.4 cm^2/Vs to 0.005 cm^2/Vs. On the other hand, when pentacene is replaced by di(phenylvinyl)anthracene (a newly synthesized compound with three smaller conjugated cores separated by vinyl groups), the initial mobility is essentially the same as for the pentacene transistor (0.3 cm^2/Vs), but the mobility degrades much less rapidly compared with the pentacene transistor (from 0.3 cm^2/Vs to 0.2 cm^2/Vs after 100 days in air).

[1] *Klauk, H., U. Zschieschang, J. Pflaum and M. Halik.* Nature **445**, 745–748 (2007).

[2] *Klauk, H., U. Zschieschang and M. Halik.* Journal of Applied Physics **102**, 074514 (2007).

[3] *Klauk, H., U. Zschieschang, R.T. Weitz, H. Meng, F. Sun, G. Nunes, D.E. Keys, C.R. Fincher and Z. Xiang.* Advanced Materials **19**, 3382–3384 (2007).

Conducting films and composites based on carbon nanotubes

S. Roth, B. Hornbostel, V. Skakalova and U. Dettlaff

Carbon nanotubes are often referred to as the most exciting material of the 21st century, due to the extraordinary properties theoretically predicted for individual nanotubes. They should be perfect electrical conductors, excellent thermal conductors, mechanically very strong and chemically fairly inert. Some of these properties can be experimentally verified for individual tubes. In most technological applications, however, one does not use individual tubes but arrays of tubes, such as bucky paper, or tubes incorporated in polymers, metals, or ceramic matrices. One hopes that these nanotube-based composites combine the properties of nanotubes and matrix, e.g., electrical conductivity of nanotubes and plastic processibility of polymers.

Electrical properties. Figure 47 shows how the electrical conductivity of polycarbonate changes when nanotubes are added. The conductivity is plotted on a semi-logarithmic scale vs. the nanotube concentration [1]. At very low concentrations the conductivity is dominated by the properties of the matrix and at high concentrations by the properties of the nanotubes. There is a critical concentration at which the conductivity changes abruptly. This occurs when the nanotubes begin to touch each other and form continuous conduction paths. This concentration is called percolation threshold. The high concentration value in the plot is still much lower than expected for ideal conductivity of individual tubes. This is due to the fact that in a network the major contribution to the electrical resistance is not from the tubes but from the contacts between tubes.

Percolation has been treated from the theoretical point of view in many papers. Computer simulations show that in a three-dimensional sample filled with spherical conductive particles the percolation threshold is at about 20 vol.%. If the particles are not spherical but long and thin the threshold can be lowered appreciably. In a rough approximation it is inversely proportional to the aspect ratio, i.e., to the ratio between nanotube length and nanotube diameter.

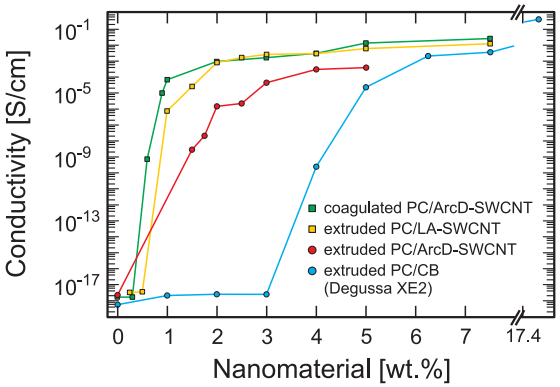

Figure 47: Electric properties of polycarbonate filled with various types of carbon nanotubes [1].

The typical diameter of a single-walled nanotube is about 1 or 2 nm. While tubes can be made up to several millimeters long, in most composites the length is about 1 μm, and then the aspect ratio is about 1000. This reasoning would lead to a percolation threshold much below 1% for nanotubes in polymers. In practice, often values of several percent are found. This can be due to the fact that many nanotube samples do not contain pure nanotubes but as much as 50 or even 70% of non-tubular carbonaceous by-products. In addition, long nanotubes might break when they are incorporated in the polymer matrix. Furthermore, nanotubes tend to form bundles, so that the effective aspect ratio is much lower than calculated from individual tubes.

One of the uses of polymers made conductive by filling with nanotubes is microwave attenuation, e.g., for avoidance of electromagnetic interference between computer components or between a mobile phone and the navigation system of an airplane. Figure 48 shows the microwave attenuation of various nanotube/polycarbonate samples. We see more or

less constant attenuation in the whole frequency range from 100 MHz to 1 GHz [2]. For sample III the attention is about 30 dB, already pretty close to the technological requirements (80 dB for a 3 mm thick plate).

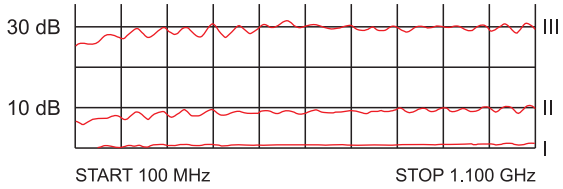

Figure 48: Attenuation of electromagnetic waves by polycarbonate filled with nanotubes [2].

Transparent conducting films. Another important application are transparent conducting films. Such films are needed for cover layers of solar cells or light emitting devices. Figure 49 shows a photograph of a conductive film through which we can look on an ohmmeter (the meter reads 10.9 kΩ). Figure 50 shows a systematic study of the surface conductivity of thin films and their transparency for visible light.

Figure 49: Transparent conducting film based on carbon nanotubes.

Electrical conductors absorb electromagnetic waves and a delicate compromise has to be found if a material is supposed to be conductive and transparent at the same time. At present, the benchmark material is indium-tin-oxide (ITO). This material usually has a surface resistance of about 10 Ω/square at a transparence of 90%. Films coated or filled with carbon nanotubes do not yet meet these values. The conductivity still has to be improved even for highest quality nanotubes. It is expected that this can be achieved by chemical modification of the nanotubes, which should lead to a better compatibility with the matrix and to lower the contact resistance between the tubes.

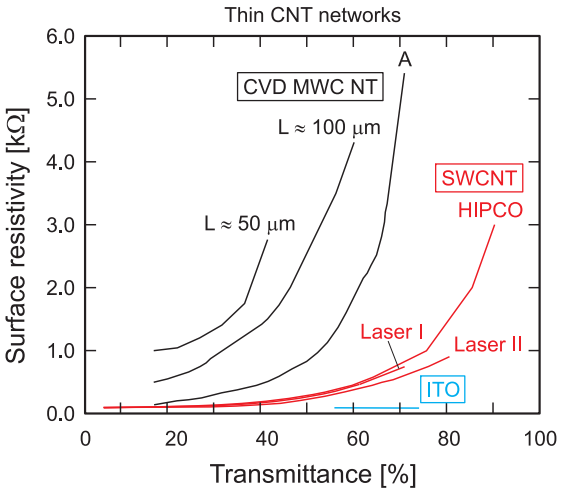

Figure 50: Surface resistivity of carbon nanotube coated films as a function of optical transmittance. L: Length of nanotubes.

Transparent transistors. Figure 51 shows a transparent transistor based on two separated transparent carbon nanotube films. A transparent polymer film (from an overhead transparency) is coated with a nanotube layer. This layer serves as the gate of the transistor. It is separated from a second nanotube layer by a thin insulating parylene sheet.

Figure 51: Transparent resistor based on two transparent and conducting carbon nanotube films [3].

In the second nanotube layer the nanotube concentration is adjusted in such a way that its overall behavior is semiconducting. Changing the

gate voltage from –20 V to +20 V switches the transistor from the 'on' state to the 'off' state. The on-of-ratio is about 20 [3]. (Depending on the diameter and the helicity, the nanotubes are metallic or semiconducting, and usually nanotube samples contain a mixture of both. In a semiconducting film the concentration of metallic nanotubes is below the percolation threshold and the semiconducting nanotubes complete the network to form long-distance conduction paths, so that the overall behavior of this particular network is like a random array of semiconductors connected by short metal leads.)

Mechanical properties, thermal conductivity. As the above data show, changing the electrical properties of polymers by adding nanotubes has been quite successful. Much less spectacular are the efforts to change the mechanical properties. One would expect carbon nanotubes to be even more efficient than carbon fibers as re-inforcing material for polymers. But contrary to our expectations of an order of magnitude effect, only changes of a few percent are seen. This disappointing result is probably caused by the lack of load transfer between the nanotubes and the matrix: The polymer molecules just slide along the nanotube surface. Improvement can perhaps be obtained by chemical modification of the nanotubes so that they are better anchored to the matrix.

Individual carbon nanotubes are not only perfect electrical but also excellent thermal conductors. The good thermal conductivity is due to the strong covalent chemical bonds between the carbon atoms forming the tube. Our experiments have shown, that in matrices with low thermal conductivity, as in rubber, for example, addition of carbon nanotubes does, indeed, improve the thermal conductivity. But if the matrix has a fairly high thermal conductivity, like polycarbonate, the effect of nanotube addition is only marginal [4].

Investigations of nanotube composites with ceramic matrices or metal matrices are currently being performed out in close cooperation with the Fraunhofer TEG (Technische Entwicklungsgruppe).

[1] *Hornbostel, B.* Dissertation, Stuttgart (2008).

[2] *Hornbostel, B., U. Leute, P. Pötschke, J. Kotz, D. Kornfeld and S. Roth.* Physica E (2008), in print.

[3] *Artukovic E., M. Kaempgen, D.S. Hecht, S. Roth and G. Grüner.* Nano Letters **5**, 757-760 (2005).

[4] *Roth, S., B. Hornbostel and V. Skakalova.* NanoS 03.07, 14–17 (2007).

Metal nanoparticle-decorated carbon nanotubes as platform for surface-enhanced Raman scattering studies

M. Burghard, T. Assmus, K. Balasubramanian and K. Kern;
M. Scolari, N. Fu, A. Myalitsin and A. Mews (Universität Siegen)

The surface-enhancement of Raman scattering arising from locally enhanced electric fields in the vicinity of metallic nanostructures has attracted strong scientific interest for several decades. By now, the possibility of single molecule detection with the aid of surface-enhanced Raman spectroscopy (SERS) is well-documented. The strong electromagnetic fields enabling such ultrahigh sensitivity originate from the excitation of surface plasmons in the metallic nanostructures. In most studies, the near-field of colloidal metal particles has been exploited, although specifically designed metallic nanostructure arrays gain increasing importance as substrates [1]. However, such experiments are often hampered by the poorly defined position and orientation of the molecules, which might even change during the measurements.

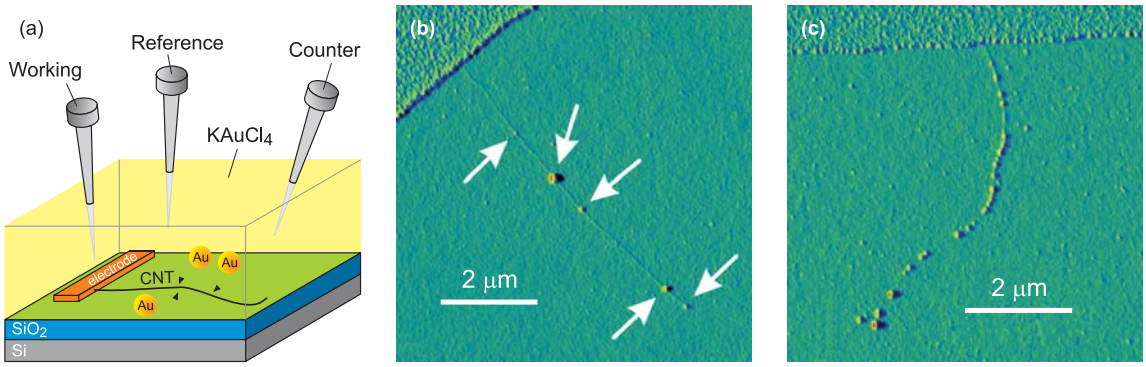

Figure 52: (a) Sketch of the setup used for electrodeposition of gold nanoparticles onto individual carbon nanotubes contacted by an electrode line. (b,c) AFM images of two gold particle-decorated single-wall carbon nanotubes. Depending on the electrodeposition parameters, a low density of particles (b) or a dense particle arrangement (c) can be obtained. The gold particles present on the nanotube in panel (b) are highlighted by arrows. The features on the upper left corner in panel (b) and on the upper edge of panel (c) are the electrodes needed for applying a potential to the nanotubes.

We have devised a new SERS configuration, comprised of gold nanoparticles attached onto single-wall carbon nanotubes (SWCNTs), which alleviates these complications [2,3]. In these hybrids, the position of the nanoparticles is stable even under strong laser illumination. It thus becomes possible to directly compare the Raman response of the same 'macromolecule' (i.e., carbon nanotube) with and without a gold particle on top. Although the detailed structure of the particles remains difficult to access, scanning force microscopy provides valuable information such as the precise size and approximate shape of the particles.

In order to decorate individual SWCNTs with metallic nanoparticles, an electrodeposition approach was used (Fig. 52). It involves the electrochemical reduction of $[AuCl_4]^-$ ions, which yields gold particles whose density can be controlled by the electrochemical parameters (mainly the magnitude and duration of the applied potential), as shown by Fig. 52(b,c). The deposited particles have sizes of several tens of nanometers. A particular advantage of the electrodeposition method is the resulting intimate contact between the particles and the underlying nanotube, which is difficult to achieve by other means.

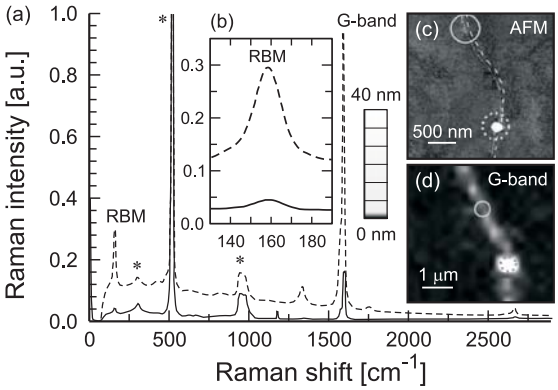

Figure 53: (a) Raman spectra recorded at two positions along an individual semiconducting single-wall carbon nanotube ($\lambda_{exc} = 568$ nm). The Raman intensity in the spectrum of the tube section covered by a ≈ 40 nm-sized gold particle (broken line) is approximately 4 times larger than in the bare tube spectrum (solid line). Peaks originating from the Si/SiO_2 substrate are marked by an asterisk. (b) Magnified view of the low-energy range containing the radial breathing mode (RBM). (c) AFM image of the nanotube, with the two circles marking the investigated bare (upper circle) and the particle-decorated (lower circle) tube section. (d) Corresponding G-band Raman image of the examined tube segment.

Raman spectra acquired with a confocal microscope from an individual semiconducting SWCNT decorated by a low density of gold particles are depicted in Fig. 53. In the lower energy range, the radial breathing mode (RBM)

occurs ($\approx 160\,\mathrm{cm}^{-1}$), which comprises the in-phase movement of carbon atoms in the radial direction. Moreover, the G-band involving C–C stretch vibrations can be discerned below $1600\,\mathrm{cm}^{-1}$. It is apparent that the peak intensity in the Raman spectrum recorded over the gold particle is considerably larger (by a factor of 4) than in the spectrum of the bare tube section. In order to compare this enhancement to the case of SERS on small molecules, the very rapid decay of the surface plasmons from the gold particle surface has to be taken into account. It is reasonable to assume that only a few percent of the nanotube section within the diffraction limited laser spot ($d \approx 500\,\mathrm{nm}$) is enhanced by the particle. On this basis, a local (effective) enhancement factor of approximately two orders of magnitude is estimated, in good agreement with theory [4].

In Fig. 54, the G-band intensity measured at three different positions along another SWCNT is displayed for four different excitation wavelengths. The spectra collected from the bare nanotube section (position 1) exhibit considerably higher Raman intensity upon excitation with 568 nm, as compared to smaller (488 nm and 514 nm) and larger (647 nm) wavelengths. This dependence is brought about by the resonance enhancement effect, which occurs when the absorbed or scattered photon is in resonance with an optical transition between the van Hove singularities of the tube. Furthermore, for an excitation with 568 nm, the gold particle with a diameter of 70 nm (position 3) causes a stronger enhancement than the one with a diameter of 35 nm (position 2). This difference can be explained by the fact that only for the larger particle the plasmon resonance is sufficiently broadened towards lower energies, thus ensuring resonance with the longer excitation wavelength. Taken together, these findings confirm in an illustrative manner that maximum Raman enhancement requires combined optical resonance with both the nanotube and the metal particle. It has been found that under these conditions also the photoluminescence signal of the particles reaches its maximum [3].

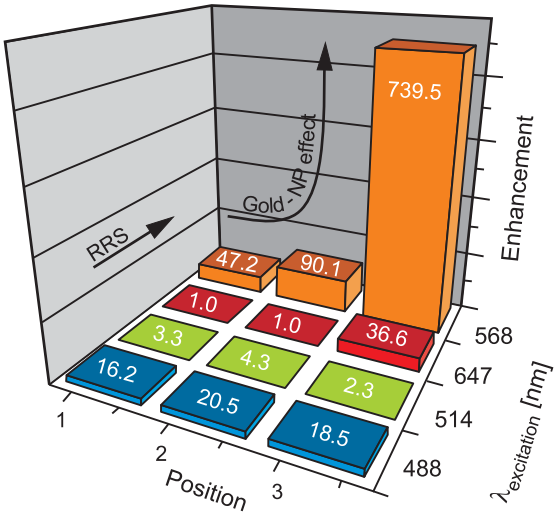

Figure 54: Bar diagram comparing the Raman intensities detected at three different positions along an individual single-wall carbon nanotube using four different laser wavelengths. Position 1 is the bare nanotube, while at positions 2 and 3 the nanotube bears two particles which differ in size (position 2: 35 nm, position 3: 70 nm). The intensity enhancement observed for $\lambda_{exc} = 568\,\mathrm{nm}$ is due to resonant excitation of the nanotube (resonance Raman spectroscopy, RRS), while the most prominent signal reflects simultaneous resonance with the surface plasmon of the 70 nm particle.

Occasionally, also dimers consisting of closely spaced gold particles are encountered on the decorated SWCNTs. At these locations, larger effective enhancement factors of up to four orders of magnitude were observed. The stronger enhancement in comparison to the single particle case can be attributed to the enhanced electric field inside the cavity between the particles. In fact, electromagnetic theory predicts that the field enhancement in the center of particle dimers with an interparticle distance of a few nanometers is several orders of magnitude larger than at the surface of individual particles [4]. The cavity effect also leads to an altered behavior in polarization dependent Raman measurements, as a consequence of the preferential orientation of the near-field distribution of the dimers. Future investigations could address the influence of the cavity size and the orientation of the dimer axis with respect to the long axis

of the tube. Moreover, the use of particles composed of alternative metals like silver may lead to a sizeable contribution of charge transfer to the Raman enhancement.

[1] *Tan, R.Z., A. Agarwal, N. Balasubramanian, D.L. Kwong, Y. Jiang, E. Widjaja and A. Garland.* Sensors and Actuators A **139**, 36–41 (2007).

[2] *Assmus, T., K. Balasubramanian, M. Burghard, K. Kern, M. Scolari, N. Fu, A. Myalitsin and M. Mews.* Applied Physics Letters **90**, 173109 (2007).

[3] *Scolari, M., A. Mews, N. Fu, A. Myalitsin, T. Assmus, K. Balasubramanian, M. Burghard and K. Kern.* J. of Physical Chemistry C **112**, 391–396 (2008).

[4] *Xu, H.X., J. Aizpurua, M. Käll and P. Apell.* Physical Review E **62**, 4318–4324 (2000).

Superconductivity

One of the central themes of ongoing research at the Institute is the competition of superconductivity with other structural phases in high-T_c superconductors. Spin dynamics of superconducting $YBa_2Cu_3O_{6.45}$ probed by neutron scattering indicates the coexistence of liquid-crystalline nematic order with superconductivity in underdoped cuprates. The observation of a pressure-induced phase transition in the double-chain superconductor $YBa_2Cu_4O_8$ suggests that the T_c maximum under pressure may be caused by a structural instability. The renormalized mean-field analysis in the two-dimensional Hubbard model illustrates that antiferromagnetism and *d*-wave superconductivity suppresses each other, leaving only a small region in parameter space where both orders can coexist. The use of recently discovered triplet superconductors, e.g., Sr_2RuO_4, in Josephson junctions is expected to produce new phase sensitive devices. This prospects stimulated interest in analyzing the novel Josephson effects in triplet superconductor – ferromagnet – triplet superconductor junctions. Finally the pressure effects on the superconducting transition in the novel layered superconductors nH-CaAlSi have been explored by combining experiments and ab initio calculations of their electron-phonon properties.

Electronic nematic state in high-temperature superconductors

V. Hinkov, D. Haug, C.T. Lin and B. Keimer;
B. Fauqué, P. Bourges and Y. Sidis (LLB, CEA-Saclay, France);
A. Ivanov (ILL, Grenoble, France); C. Bernhard (University of Fribourg, Switzerland)

Liquid crystals are states of matter without static crystalline order that break the rotational symmetry of free space while at least partially preserving its translational symmetry. Highly correlated electronic phases with symmetry properties analogous to those of conventional liquid crystals have been theoretically predicted [1] and recently discovered in semiconductor heterostructures and in the layered bulk transition metal oxide $Sr_3Ru_2O_7$ [2]. In both cases, however, these phases are stable only at milli-Kelvin temperatures and in high magnetic fields, and have thus far only been probed by transport measurements. The microscopic mechanisms underlying the formation of electronic liquid crystals therefore remain largely unexplored by experiments. Here we use inelastic neutron scattering to investigate the role the spin degrees of freedom in the formation of electronic liquid crystal states in the underdoped high-temperature superconductor $YBa_2Cu_3O_{6.45}$ [3].

In the cuprate family, $(La,Nd)_{2-x}Sr_xCuO_4$, the two-dimensional electron system in the CuO_2 layers exhibits a state with uniaxial spin and charge order, which was termed ‘stripes’. When this order is static, both the translational and the rotational symmetry (C4 symmetry) of the crystal lattice are broken. However, also more exotic states are conceivable, e.g., the system could break rotational symmetry while preserving translational symmetry. In analogy to conventional liquid crystals, this is called electronic nematic order.

In general, when a system exhibits some sort of symmetry breaking, a weak aligning field is sufficient to induce a macroscopically observable

effect. For instance, weak electric fields can align the nematic director in conventional liquid crystals. In $YBa_2Cu_3O_{6+x}$, a slight orthorhombicity, induced by one-dimensional CuO chains lying in between the CuO_2 bilayers, can serve as aligning field for symmetry-broken electronic phases.

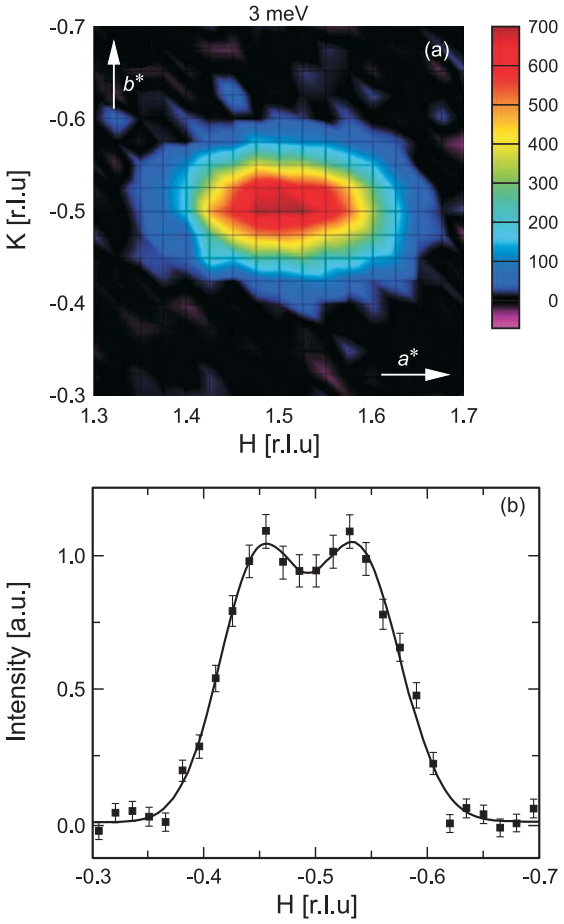

Figure 55: Geometry of the spin excitations around $\boldsymbol{Q}_{AF}$ in the *ab* plane at $T = 5$ K. (a) Intensity map of the spin-excitation spectrum at $E = 3$ meV. (b) Scan along $a^\star$ through $\boldsymbol{Q}_{AF}$ with enhanced resolution as compared to $a^\star$, revealing two incommensurate peaks.

First indications for nematic order in $YBa_2Cu_3O_{6+x}$ came from measurements of the in-plane *ab* anisotropy of the electrical resistivity, which shows a large temperature and doping dependence [4]. A determination of the spin susceptibility by magnetic neutron scattering has the potential to elucidate the role of the omnipresent spin-excitations and contribute to the understanding of the underlying microscopic mechanism. Our sample is an array of co-aligned twin-free single crystals with a superconducting transition temperature $T_c = 35$ K. In Fig. 55(a) we show the in-plane distribution of the imaginary part of the spin susceptibility χ'' at a fixed energy $E = 3$ meV. As previously reported, the magnetic intensity is concentrated around the in-plane wavevector $\boldsymbol{Q}_{AF} = (0.5, 0.5)$ in reciprocal lattice units, in reminiscence of the antiferromagnetic state of undoped $YBa_2Cu_3O_6$. A cut through the spectrum with improved instrumental resolution reveals two incommensurate peaks displaced from $\boldsymbol{Q}_{AF}$ along $a^\star$ by the incommensurability δ, Fig. 55(b).

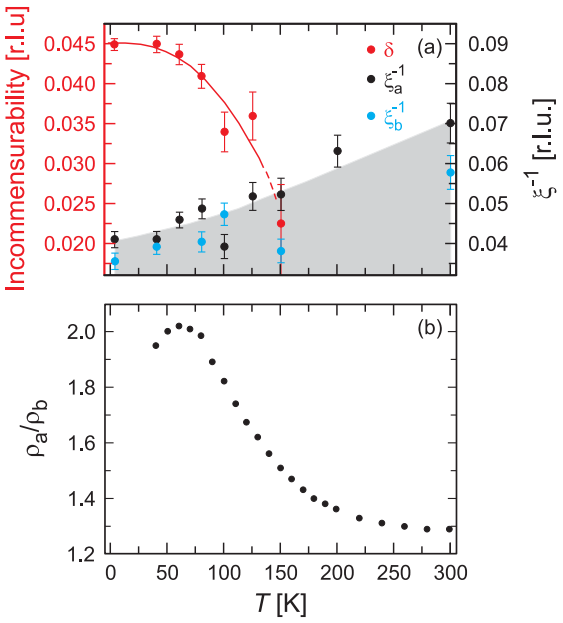

Figure 56: (a) Temperature evolution of the incommensurability δ and the half-width-at-half-maximum of the peaks along $a^\star$ (black symbols) and along $b^\star$ (open symbols) extracted from the raw data. (b) The ratio of the electrical resistivities along $a^\star$ and $b^\star$, ρ_a/ρ_b, of a sample with similar doping level as ours, reproduced from [4].

The observed in-plane anisotropy evolves in an unusual way with T: In Fig. 56(a) we show that δ exhibits an order-parameter-like behavior with an onset temperature ≈ 150 K. It is remarkable that the in-plane resistivity ratio ρ_a/ρ_b in a sample of similar doping exhibits a pronounced enhancement below a comparable temperature (Fig. 56(b)).

Ordinary magnetic phase transitions are associated with the formation of static magnetic moments, which are absent in our sample above 2 K, as we found in muon spin rotation measurements. The signal derives entirely from the CuO_2 planes – thus, coupling to the spins on the 1D CuO chains can be ruled out as a driving force of the correlations. This implies that the spin system in the CuO_2 planes becomes inherently unstable toward the formation of a uniaxial fluctuating spin texture at ≈ 150 K. The small orthorhombic distortion ($a = 3.8388$ Å, $b = 3.8747$ Å) serves as an aligning field for the incommensurate domains. It is remarkable that while a temperature evolution of δ has previously been reported for the $La_{2-x}(Sr, Ba)_xCuO_4$ family, a spontaneous onset of the incommensurability has thus far not been observed.

We remark that in the more highly doped $YBa_2Cu_3O_{6.6}$ – although the orthorhombicity is enhanced – ρ_a/ρ_b is reduced and much less temperature dependent, whereas the spectral weight of the low-energy collective spin excitations is strongly diminished and the in-plane anisotropy at the lowest detectable energies is reduced ('spin gap') compared to $YBa_2Cu_3O_{6.45}$ [5].

The explored energy and momentum dependence allows conclusions about the microscopic model of the interplay of the spin and charge system in the cuprates. The incommensurate peaks can arise either from a spatial modulation of the amplitude of collinear spin moments or from a configuration in which the moment direction varies but the amplitude remains constant. In the literature, the terms 'stripe modulation' and 'spiral modulation' are used for these two cases. Spin-amplitude modulated states are associated with a modulation of the charge carrier density, resulting in a difference of the carrier mobility along and perpendicular to the modulation axis. Further work is necessary to clarify whether an anisotropic hopping transport mechanism can explain the in-plane resistivity anisotropy in a spiral model.

In summary, the spin dynamics of $YBa_2Cu_3O_{6.45}$ provides strong evidence of a cooperative transition to an electronic nematic state. Finally, we note that the dispersion and in-plane geometry of the excitations *above* T_c at energies exceeding the spin gap of $YBa_2Cu_3O_{6.6}$ [5] bear resemblance to the nearly gapless low-energy excitations in $YBa_2Cu_3O_{6.45}$ [3]. This suggests the presence of a quantum phase transition at an oxygen content of $O_{6.5}$, where the nematic order disappears and the spin gap opens up.

[1] *Kivelson, S.A., W. Fradkin and V.J.Emery.* Nature **393**, 550–553 (1998).

[2] *Borzi, R.A., S.A. Grigera, J. Farrell, R.S. Perry, S.J.S. Lister, S.L. Lee, D.A. Tennant,Y. Maeno and A.P. Mackenzie.* Science **315**, 214–217 (2007).

[3] *Hinkov, V., D. Haug, B. Fauqué, P. Bourges, Y. Sidis, A. Ivanov, C. Bernhard, C.T. Lin, and B. Keimer.* Science **319**, 597–600 (2008).

[4] *Ando, Y., S. Kouji, S. Komiya and A.N. Lavrov.* Physical Review Letters **88**, 137005 (2002).

[5] *Hinkov, V., P. Bourges, S. Pailhès, Y. Sidis, A. Ivanov, C.D. Frost, T.G. Perring, C.T. Lin, D.P. Chen and B. Keimer.* Nature Physics **3**, 780–785 (2007).

Structural phase transition of $YBa_2Cu_4O_8$ under pressure

X. Wang, F.H. Su, S. Karmakar, K. Syassen, Y.T. Song and C.T. Lin;
H. Wilhelm (Diamond Light Source, Didcot, UK); M. Hanfland (ESRF Grenoble, France)

The pressure dependence of the superconducting transition temperature of cuprate high-T_c superconductors (HTSCs) is thought to be of fundamental interest for elucidating the microscopic mechanism of the superconducting state as well as for finding new materials with higher critical temperature. Extensive electrical transport and magnetic studies of HTSCs have revealed a canonical change of T_c with pressure [1]: It first increases, passes through a maximum value at some intermediate pressure, and then decreases. This scenario also applies to the underdoped double chain compound $YBa_2Cu_4O_8$, as is illustrated in Fig. 57 [2]. Different from other HTSCs, $YBa_2Cu_4O_8$ has a fixed stoichiometry. Hence, for this compound the effects of pressure can be assumed independent of the ordering of mobile oxygen defects.

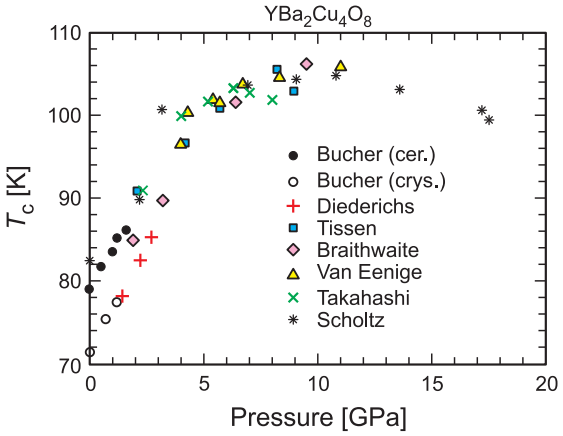

Figure 57: The superconducting transition temperature of $YBa_2Cu_4O_8$ as a function of pressure from different sources as compiled in [2].

Although the question of the pairing mechanism responsible for high-T_c superconductivity remains unsettled, it is generally believed that one of the key parameters controlling the T_c values in cuprates is the charge carrier concentration in the CuO_2 planes. It has been postulated that the application of high pressure leads to the change of the hole concentration; this is supported by a number of measurements. However, attempts at a quantitative analysis of the dependence of T_c on pressure, based solely on a pressure-driven charge redistribution, have not been particularly satisfactory, and other mechanisms linked to a change in the Cu–O–Cu buckling angle within the CuO_2 planes are invoked [1,2].

In order to explore the possibility that the T_c maximum of $YBa_2Cu_4O_8$ near 10 GPa (Fig. 57) is caused by changes in structural and/or dynamical properties, we have studied the structural and lattice dynamical properties of $YBa_2Cu_4O_8$ at pressures up to 20 GPa by synchrotron X-ray diffraction and Raman spectroscopy.

The high-quality single crystals available for the present study originated in the Crystal Growth Service Group at MPI-FKF. They were grown at ambient air/oxygen pressure by a flux method [3]. This is different from the conventional growth method for $YBa_2Cu_4O_8$ which involves high oxygen pressure. Our recent Raman measurements on $YBa_2Cu_4O_8$ clearly indicate a structural phase transition to take place near 11 GPa. The most prominent spectral change was a major loss of intensity of chain-related Raman modes. We skip here over various aspects of the Raman studies and focus on the structural effects.

The structural phase transition is supported by powder X-ray diffraction studies. Figure 58 shows high-pressure diffraction diagrams taken just before (10.1 GPa) and after (11.9 GPa) the phase transition. Like the starting phase, the diffraction data for the high pressure phase can be interpreted in terms of an orthorhombic lattice. Systematic extinctions are compatible with space group *Imm*2.

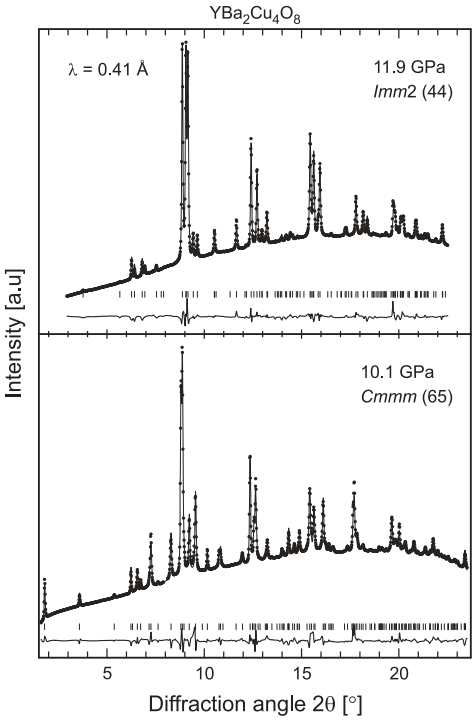

Figure 58: Observed, calculated, and difference X-ray powder patterns of $YBa_2Cu_4O_8$ for the *Cmmm* phase at 10.1 GPa (bottom) and the high–pressure *Imm*2 phase at 11.9 GPa (top).

Refined lattice parameters are shown in Fig. 59. One observes that the *a*- and *b*-axes as well as the *a*/*b*-ratio, i.e., the orthorhombicity, are only weakly affected by the transition, whereas the *c*-axis undergoes a major collapse, causing a 6% decrease in specific volume.

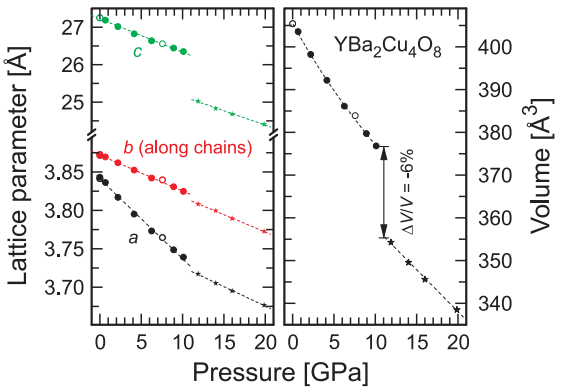

Figure 59: Lattice parameters and unit cell volume of $YBa_2Cu_4O_8$ versus pressure for the ambient- and high-pressure phases.

The diffraction diagrams, recorded under nearly hydrostatic pressure conditions, were suitable for analysis by full-profile (Rietveld) refinements, such that internal positional parameters could be determined. Segments of the crystal structures before and after the phase transition are shown in Fig. 60. The structural building blocks of the ambient-pressure phase of $YBa_2Cu_4O_8$ consist of double-layer Cu(2)–O(2,3) planes with apical O(1) atoms attached and of double chains of Cu(1)–O(4) atoms running along the *b*-axis. Subsequent double-layer CuO_2 blocks along *c* are displaced with respect to each other by half a unit cell dimension along the *b*-direction. Obviously, the structure has a large empty channel located

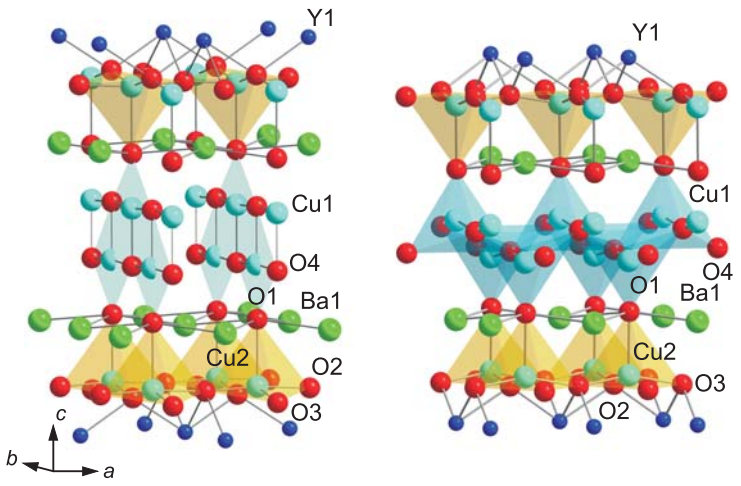

Figure 60: Crystal structure of the ambient-pressure phase of $YBa_2Cu_4O_8$ (left) and of the high-pressure modification at 11.9 GPa. To save space, only one half of the unit cell along *c* is shown. The cut is at the Y-atom layers located in between the CuO_2 planes forming the double layers.

between two neighboring double chains. These open channels make the structure susceptible to a pressure-induced instability. The phase transition can be viewed as a concerted tilting of the double chain ribbons away from the *c*-axis direction combined with a shear motion of nearly rigid CuO_2 double-layers and the attached apical oxygen atoms. In this way the structure collapses along *c*.

Perhaps the most remarkable structural effect is that the coordination of the chain Cu(1) atoms by oxygen atoms increases at the phase transition. This should affect the oxidation state of Cu(1) and involve a redistribution of charge within the unit cell. In other words, we speculate that holes are withdrawn from the double-layers, thus reducing the hole doping of the layers. This should then affect the superconducting transition temperature in a discontinuous manner because the phase transition is of the first order. Measurements of the pressure dependence of T_c published so far (Fig. 57) show a broad maximum near 10 GPa. This apparent inconsistency with our structural studies can be explained by the fact, that the T_c measurements were performed under non-hydrostatic conditions, where the phase transition is likely to be smeared out in pressure.

In summary, $YBa_2Cu_4O_8$ undergoes a first-order structural phase transition at a pressure of ≈ 11 GPa. The transition can be interpreted as a displacement of successive double-layer CuO_2 building blocks with respect to each other. That displacement is coupled to a tilt plus distortion of the double chain ribbons and a change in the coordination of Cu(1) atoms which form the chains in the original structure. The observation of a structural instability of $YBa_2Cu_4O_8$ sheds new light on the interpretation of the T_c maximum under pressure. So far, modeling of the T_c maximum was based on the assumption that the ambient-pressure structure of $YBa_2Cu_4O_8$ remains stable under pressure. The finding reported here may stimulate a more detailed experimental study of the superconducting properties near 10 GPa and may also lead to reconsider a theoretical modeling of the electronic structure by taking into account the structural phase transition.

[1] *Schilling, J.S.* in: *High-Temperature Superconductivity: A Treatise on Theory and Applications.* J.R. Schrieffer and J.S. Brooks (Eds.); Springer, Berlin (2007).

[2] *Chen, X.J., H.Q. Lin and C.D. Gong.* Physical Review Letters **85**, 2180–2183 (2000).

[3] *Song, Y.T., J.B. Peng, X. Wang, G.L. Sun and C.T. Lin.* Journal of Crystal Growth **300**, 263–266 (2007).

Antiferromagnetism and *d*-wave superconductivity in the two-dimensional Hubbard model

J. Reiss, D. Rohe and W. Metzner

One of the most frequently discussed models for the electrons in the copper-oxide planes of high-temperature superconductors is the two-dimensional Hubbard model. The model describes tight-binding electrons with a local repulsion $U > 0$, as specified by the Hamiltonian

$$H = \sum_{\mathbf{i},\mathbf{j}} \sum_{\sigma} t_{\mathbf{ij}}\, c^{\dagger}_{\mathbf{i}\sigma} c_{\mathbf{j}\sigma} + U \sum_{\mathbf{j}} n_{\mathbf{j}\uparrow} n_{\mathbf{j}\downarrow} \qquad (6)$$

in standard second quantization notation.

A hopping amplitude $-t$ between nearest neighbors and an amplitude $-t'$ between next-nearest neighbors on a square lattice leads to the dispersion relation $\varepsilon_k = -2t(\cos k_x + \cos k_y) - 4t' \cos k_x \cos k_y$ for single-particle states. In agreement with the generic phase diagram of the cuprates, the Hubbard model is an antiferromagnetic insulator at half-filling (provided t' is not too big), and is expected to become a *d*-wave superconductor away from half-filling

in two dimensions. It turned out to be very hard to detect superconductivity in the Hubbard model by exact numerical computation, as a consequence of finite size and/or temperature limitations.

The tendency toward antiferromagnetism and *d*-wave pairing in the two-dimensional Hubbard model is present already at weak coupling. However, conventional perturbation theory breaks down in the most interesting density regime, since competing infrared divergences appear as a consequence of Fermi surface nesting and van Hove singularities. A controlled treatment of these divergences can be achieved by a renormalization group (RG) analysis, which takes into account the particle-particle and particle-hole channels on equal footing.

A suitable framework for a systematic RG analysis of the 2D Hubbard model is provided by the so-called exact or *functional* RG [1]. In this approach, fermionic fields in a functional integral representation of the model are integrated successively, descending step by step in energy scales. This can be formulated as an exact hierarchy of flow equations for the effective interactions. The energy scale of the fields, Λ, is the flow parameter. Several groups have computed the flow of effective two-particle interactions for the two-dimensional Hubbard model, using various versions of the functional RG in one-loop approximation. The effective interactions exhibit a pronounced momentum dependence. Antiferromagnetic and superconducting instabilities were detected from the flow of the corresponding susceptibilities [1].

At low temperatures, and in particular at $T = 0$, the effective two-particle interaction Γ^{Λ} obtained from the RG flow in one-loop approximation diverges at a finite scale $\Lambda_c > 0$, that is, before all fields have been integrated out. The physical reason for this divergence is the tendency of the system to order, that is, spontaneous symmetry breaking. In principle, an order parameter could be included in the functional RG framework. However, in case of two competing order parameters (antiferromagnetism and superconductivity) a full RG treatment of the ordered phases is rather complicated. We therefore explore a simpler alternative and combine the RG with a mean-field (MF) theory of symmetry breaking [2]. In this RG + MF approach the one-loop flow is stopped at a scale Λ_{MF} that is small compared to the bandwidth, but still safely above the scale Λ_c where the two-particle vertex diverges. At this point the vertex has developed already a pronounced momentum dependence, reflecting in particular antiferromagnetic and superconducting correlations. The integration over the remaining degrees of freedom, below Λ_{MF}, is treated in a mean-field approximation allowing, in particular, antiferromagnetic and superconducting order.

The mean-field Hamiltonian is defined on a restricted momentum region near the Fermi surface, with $|\varepsilon_k - \mu| < \Lambda_{\mathrm{MF}}$, and the effective interactions entering the mean-field equations are extracted from $\Gamma^{\Lambda_{\mathrm{MF}}}$. The order parameter for superconductivity (gap function) is given by

$$\Delta_{\mathbf{k}} = \frac{1}{L} \sum_{\mathbf{k}'} V_{\mathbf{k}\mathbf{k}'} \langle a_{-\mathbf{k}\downarrow} a_{\mathbf{k}\uparrow} \rangle , \tag{7}$$

where $a_{k\sigma}$ is the annihilation operator in momentum space and L the number of lattice sites. The pairing interaction $V_{kk'}$ is obtained from the spin singlet component of $\Gamma^{\Lambda_{\mathrm{MF}}}$ in the Cooper channel. The antiferromagnetic order parameter is

$$A_{\mathbf{k}} = \frac{1}{L} \sum_{\mathbf{k}'} U_{\mathbf{k}\mathbf{k}'} \langle m_{\mathbf{k}} \rangle , \tag{8}$$

where $\langle m_{\mathbf{k}} \rangle = \langle a^{\dagger}_{\mathbf{k}\uparrow} a_{\mathbf{k}+\mathbf{Q}\uparrow} - a^{\dagger}_{\mathbf{k}\downarrow} a_{\mathbf{k}+\mathbf{Q}\downarrow} \rangle$ is the staggered magnetization. The interaction $U_{\mathbf{k}\mathbf{k}'}$ driving the antiferromagnetic order is also extracted from $\Gamma^{\Lambda_{\mathrm{MF}}}$. Antiferromagnetic order splits the single band $\varepsilon_{\mathbf{k}}$ in two subbands of the form

$$E^{\pm}_{\mathbf{k}} = \frac{\varepsilon_{\mathbf{k}} + \varepsilon_{\mathbf{k}+\mathbf{Q}}}{2} \pm \sqrt{\frac{1}{4}(\varepsilon_{\mathbf{k}} - \varepsilon_{\mathbf{k}+\mathbf{Q}})^2 + A^2_{\mathbf{k}}} , \tag{9}$$

with momenta restricted to the reduced ('magnetic') Brillouin zone corresponding to the reduced translation invariance of the antiferromagnetic state.

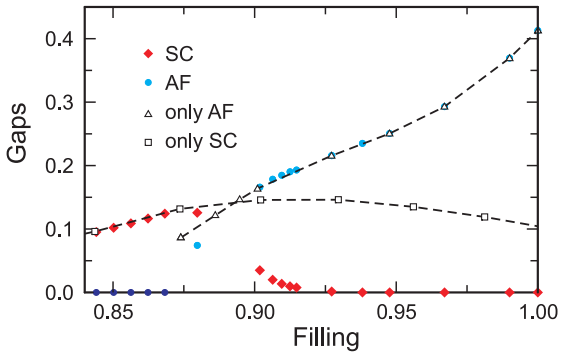

Figure 61: Amplitudes of the superconducting gap function $\Delta_{\mathbf{k}}$ and the antiferromagnetic order parameter $A_{\mathbf{k}}$ as a function of density for $U = 2.5$ and $t' = -0.15$. Filled colored symbols represent the results obtained for the combined theory with two order parameters, while in the results represented by black symbols (connected by dotted lines) only one order parameter, either antiferromagnetic or superconducting, was allowed in the mean-field calculation.

In Fig. 61 we show results from the RG + MF calculation for the amplitude of the (*d*-wave shaped) superconducting gap function and its antiferromagnetic analogue as a function of the electron density. Here and in the following we set $t = 1$, that is, all quantities with dimension energy are defined in units of t.

The interaction $U = 2.5$ is strong enough to stabilize an antiferromagnetic insulator at half-filling, in spite of the slight magnetic frustration induced by the next-to-nearest neighbor hopping $t' = -0.15$. The system is fully gapped at half-filling and the superconducting order parameter is strictly zero there. With decreasing filling the antiferromagnetic gap decreases monotonically, while Δ_k remains practically zero.

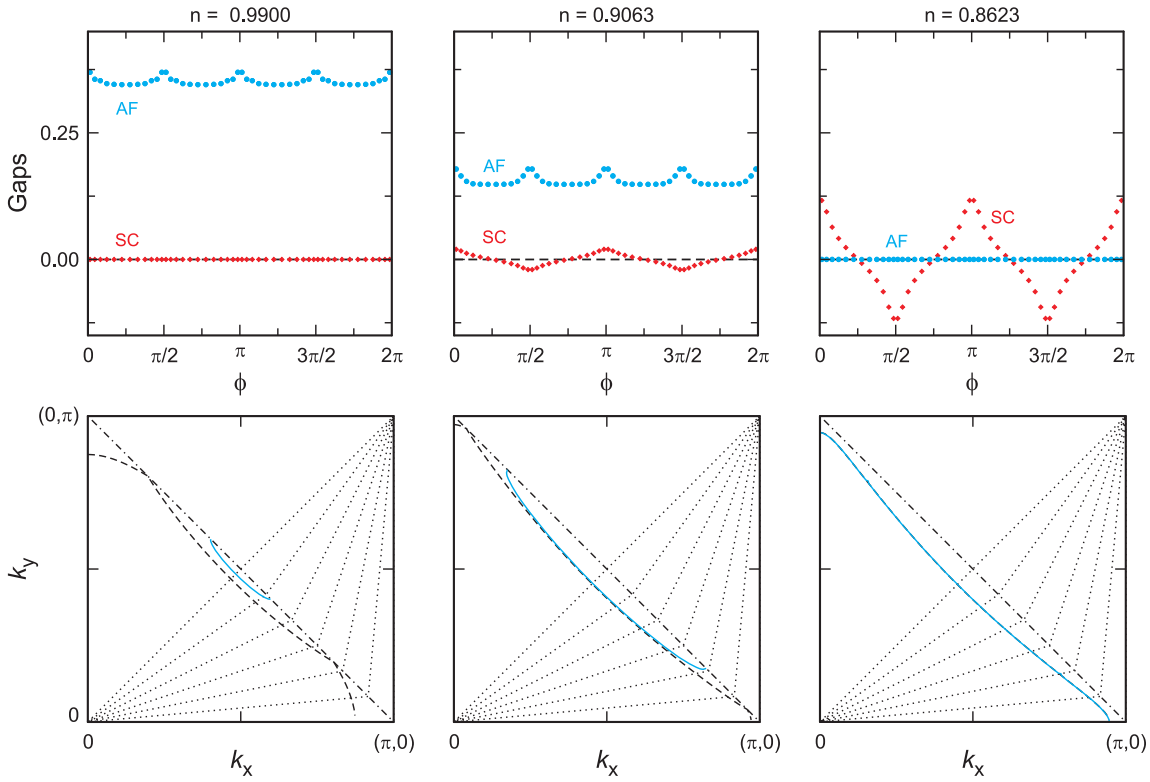

Figure 62: Top: Angular dependence of the *d*-wave superconducting and antiferromagnetic order parameters at three different densities. Bottom: Fermi surfaces in the magnetic Brillouin zone (solid blue lines); in the antiferromagnetic state close to half-filling the Fermi surface forms a hole pocket around $(\pi/2, \pi/2)$. The corresponding bare Fermi surfaces, backfolded with respect to the magnetic Brillouin zone boundary, are shown as broken lines. The straight dotted lines indicate the momentum discretization. The parameters $U = 2.5$ and $t' = -0.15$ are the same as in Fig. 61.

For electron densities below one, holes appear first in pockets around $(\pi/2, \pi/2)$, which define a surface of low-energy excitations of the non-half filled system. In principle, this residual Fermi surface is always unstable against superconductivity, due to the attractive interaction in the *d*-wave Cooper channel. However, very close to half-filling, where the pockets are small, the superconducting gap is tiny, since the *d*-wave attraction is very small near the Brillouin zone diagonal. When the hole pockets are large enough, roughly for $n < 0.92$, a sizeable superconducting gap develops, coexisting with a finite antiferromagnetic order parameter. Reducing the density further, the antiferromagnetic order drops rapidly to zero, while Δ_k remains finite and decreases comparatively slowly. The respective results for each order parameter when the other one is set to zero are also shown in Fig. 61. When A_k is set to zero, the superconducting gap Δ_k persists even at half filling. When Δ_k is set to zero, the antiferromagnetic order parameter is enhanced in the coexistence region. In both cases a finite value for one order parameter leads to a suppression of the other.

In Fig. 62 we show the angular dependence of Δ_k and A_k for three selected densities, along with the corresponding effective Fermi surfaces. The angle ϕ is defined with respect to the k_x-axis. For $n = 0.99$ we obtain a sizable antiferromagnetic gap which has *s*-wave symmetry and is slightly anisotropic. The superconducting gap is practically zero. The hole pocket enclosed by the effective Fermi surface is rather small and does not support a sizable superconducting gap.

For $n = 0.906$ we observe a coexistence of both order parameters. While A_k is reduced in size compared to the case $n = 0.99$, its shape remains essentially the same. The hole pocket extends further away from the Brillouin zone diagonal and allows for a substantial superconducting gap with *d*-wave symmetry. For the even smaller density $n = 0.862$ the antiferromagnetic order parameter vanishes and only a *d*-wave superconducting gap remains, which extends over the whole Fermi surface except at the nodal points. Note that the momentum dependence of the gap function has peaks near the van Hove points and is relatively flat near the Brillouin zone diagonal, implying that terms beyond the lowest *d*-wave harmonic $\cos k_x - \cos k_y$ contribute significantly to Δ_k.

[1] For a short review, see *Metzner, W.* Progress of Theoretical Physics, Supplement **160**, 58–78 (2005).

[2] *Reiss, J., D. Rohe and W. Metzner.* Physical Review B **75**, 075110 (2007).

Novel Josephson effects in a triplet-superconductor – ferromagnet – triplet-superconductor junction

P.M.R. Brydon and D. Manske

Since the discovery of the high-T_c cuprates, much attention has been directed towards the fabrication of phase-sensitive devices using unconventional superconducting materials. Such devices are not only of technological importance, but they also provide insight into fundamental questions such as the symmetry of the pairing wavefunction [1]. Focus has recently shifted to the properties of junctions involving *triplet* superconductors, motivated in large part by the confirmation of triplet superconductivity in Sr_2RuO_4 [2]. The triplet spin-state of the Cooper pairs implies an intimate relationship to magnetism, leading to novel tunneling effects in structures involving both triplet superconductors and magnetic phases.

Together with B. Kastening (RWTH Aachen) and D.K. Morr (University of Illinois), we have theoretically studied a device combining triplet superconductivity with magnetism, the so-called triplet-superconductor – ferromagnet – triplet-superconductor (TFT) junction [3,4]. In this junction, a thin ferromagnetic barrier is sandwiched between two bulk p_z-wave superconductors, as shown schematically in Fig. 63. The triplet-superconductor vector order parameters, the so-called $\boldsymbol{d}$-vectors, lie in the $x-y$ plane, giving Cooper pairs with $S^z = \pm 1$. The $\boldsymbol{d}$-vector in the superconductor on the left defines the x-axis; the $\boldsymbol{d}$-vector on the right is inclined to this by the angle θ. The two superconductors both have a gap of magnitude Δ_0, but there is a phase difference ϕ between them. Within the barrier, there is a component of the magnetization $\boldsymbol{M}_\perp$ in the $x-y$ plane, and a component $\boldsymbol{M}_\parallel$ along the z-axis; charge scattering is included by the potential U_P.

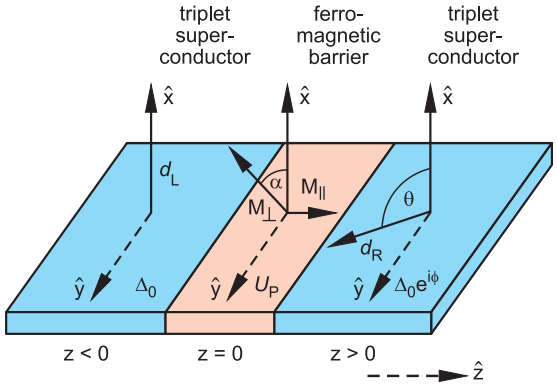

Figure 63: Schematic diagram of the TFT junction studied in this work. The $\boldsymbol{d}$-vectors in the two superconductors are misaligned by an angle θ, and there is a phase difference ϕ between the two condensates. We decompose the magnetic moment of the barrier into a component along the z-axis, $\boldsymbol{M}_\parallel$, an a component in the $x-y$ plane, $\boldsymbol{M}_\perp$, parameterized by the angle α. Charge scattering is described by the potential U_P.

We obtain the current through the barrier by solving the Bogoliubov-de Gennes equations for the junction. This yields the energies of the so-called Andreev bound states (subgap states localized at the barrier) from which the Josephson current I_J may be deduced. In what follows, we express the current in units of $ek_F\Delta_0/\hbar$ and the scattering potentials in units of $\hbar^2 k_F/m$, where k_F and m are respectively the Fermi wavevector and effective mass in the bulk superconductors. All results are for zero temperature.

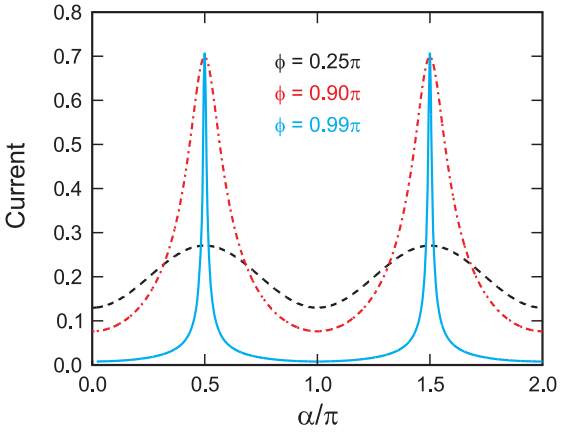

Figure 64: Dependence of the Josephson current on the angle α for several values of ϕ. $\boldsymbol{M}_\parallel = U_P = 0$, $\boldsymbol{M}_\perp = 1$, and $\theta = 0$.

In the case of a ferromagnetic barrier between two singlet superconductors, only the *magnitude* of the ferromagnetic moment is relevant to the transport. In contrast, the current through the TFT junction also depends crucially upon the *orientation* of the moment with respect to the $\boldsymbol{d}$-vectors. In the special case when the $\boldsymbol{d}$-vectors are parallel, the current is strongly dependent upon $\boldsymbol{M}_\perp$: Rotating the moment about the z-axis, the current at fixed ϕ shows a periodic dependence upon the angle α between $\boldsymbol{M}_\perp$ and the x-axis, with a maximum value when $\boldsymbol{M}_\perp \perp d_{L,R}$ (Fig. 64). The maximum becomes very sharply peaked as the phase difference approaches $\phi = \pi$; in this limit, small changes in the alignment of $\boldsymbol{M}_\perp$ produce very large changes in the current. This effect can be exploited to build a 'Josephson current switch' in which the current is turned 'on' ($I_J \neq 0$) or 'off' ($I_J \approx 0$) by rotation of the barrier moment. This 'switch' has possible relevance to quantum computing, as the behavior of the junction is similar to other two-level systems proposed as qubits. Importantly from this perspective, we find that the effect is robust to a component of the magnetization along the z-axis and charge scattering at the barrier.

As another example of the non-trivial dependence of the current on the orientation of the magnetic moment, we consider the case when $|\boldsymbol{M}_\perp| = 0$. Here the absence of spin-flip scattering at the barrier decouples the two spin channels. Misalignment of the $\boldsymbol{d}$-vectors then produces *spin-dependent* effective phase differences, $\phi_\sigma = \phi - \sigma\theta$. At $\phi = 0$, therefore, each spin channel sees a *finite* effective phase difference $-\sigma\theta$; although the current through each spin sector is finite, the total current is nevertheless vanishing (see Fig. 65). This is because the barrier transparency is the same for each spin channel, and the two contributions therefore cancel. When there is both charge scattering and scattering off a longitudinal moment, however, the effective scattering potential at the barrier is also spin-dependent and given by $U_\mathrm{P} - \sigma|\boldsymbol{M}_\parallel|$. This reduces the transmission through the spin$\downarrow$ channel more than that through the spin$\uparrow$ channel, and so as shown in Fig. 65 the current through the two channels does not cancel at $\phi = 0$. The appearance of a finite current without a phase difference between the two condensates is a very unusual result.

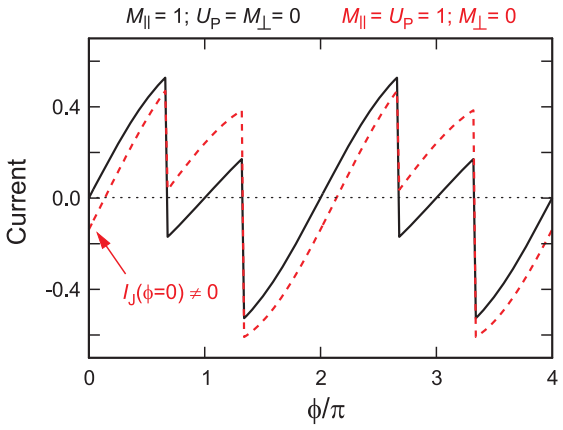

Figure 65: Current vs. phase relations for the junction showing the appearance of a finite current at $\phi = 0$ for misaligned $\boldsymbol{d}$-vectors ($\theta = \pi/3$).

The critical current of the junction is defined as the maximum current with respect to ϕ for given barrier potentials and $\boldsymbol{d}$-vector alignment. We find that the critical current of the TFT junction shows pronounced non-analyticities as a function of the barrier parameters. These are shown for example in Fig. 66, where the critical current is plotted as a function of U_P and $|\boldsymbol{M}_\perp|$. As marked in white, there is a line of first-order non-analyticity (solid) and also third-order non-analyticity (broken). These lines define the boundaries of different 'phases' of the junction, A, B and C. Within each phase, the critical current occurs at qualitatively different points along the I_J vs. ϕ curve: In region A it occurs at $\phi = \pi \pm \theta \pm 0^+$, on one side of jump discontinuities in I_J (e.g., as in Fig. 65); in region B it occurs at a stationary point; and in region C it occurs at $\phi = \pi \pm \theta \mp 0^+$, on the opposite side of the jump discontinuities compared to region A. As the scattering at the barrier is changed, or the alignment of the $\boldsymbol{d}$-vectors altered, the junction undergoes a 'transition' from one critical current state to another. We predict that these transitions will produce an observable signal in the critical current, especially so when the accompanying non-analyticity is of first-order.

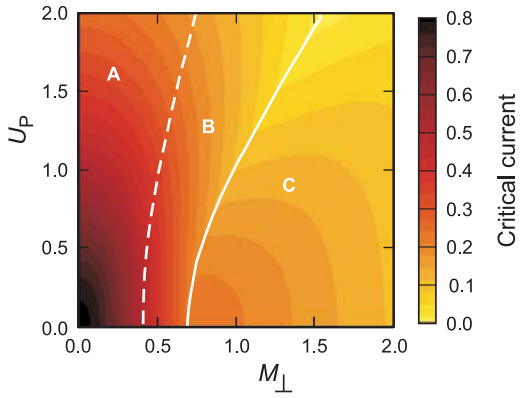

Figure 66: 'Phase diagram' for the critical current as a function of U_P and $|\boldsymbol{M}_\perp|$, for $\alpha = 0.2\,\pi$ and $\theta = 0.35\,\pi$. The solid white line indicates a first-order non-analyticity, while the broken white line denotes a third-order non-analyticity. The 'phases' A, B and C are defined in the text.

To summarize, we have extensively characterized the Josephson current through the TFT junction. We have found that the magnetic structure of the triplet pairing state significantly expands the phase space of the junction compared to a singlet system. In particular, the orientation of the magnetic moment strongly influences the current, leading to a number of exotic Josephson effects.

We have also constructed a phase diagram for the junction, which provides a novel classification scheme for the different critical current states. Our study of the TFT junction is ongoing: In addition to the charge Josephson effect discussed here, it is likely that there will also be a spontaneous *spin* current through the TFT junction. The occurrence of such a highly unconventional effect would expand the potential applications for this device.

[1] *Kashiwaya, S. and Y. Tanaka.* Reports on Progress in Physics **63**, 1641–1724 (2000).

[2] *Mackenzie, A.P. and Y. Maeno.* Reviews of Modern Physics **75**, 657–712 (2003).

[3] *Kastening, B., D.K. Morr, D. Manske and K. Bennemann.* Physical Review Letters **96**, 047009 (2006).

[4] *Brydon, P.M.R., B. Kastening, D.K. Morr and D. Manske.* Physical Review B **77**, 104504 (2008).

Pressure effects on the superconducting transition in nH-CaAlSi

L. Boeri, J.S. Kim and R.K. Kremer; M. Giantomassi (Université Catholique de Louvain, Belgium); F.S. Razavi (Brock University, St. Catherines, Canada); S. Kuroiwa and J. Akimitsu (Aoyama-Gakuin University, Kanagawa, Japan)

Superconductivity in hexagonal layered compounds has attracted broad interest since the discovery of 'high-T_c' superconductivity in MgB_2 and other structurally related compounds such as $CaSi_2$, and, very recently, alkaline-earth intercalated graphites. In all these compounds the light elements are arranged in honeycomb layers which are intercalated by alkaline earth atoms. Depending on the elements forming the honeycomb layer, the electron and phonon states involved in the superconducting pairing are different. In MgB_2, holes in the σ-bands of the B-layer couple strongly to the B bond-stretching phonon modes. In $CaSi_2$, which can be considered as the 'antibonding analogue' to MgB_2, the $\sigma^\star$-bands are strongly coupled to the bond-stretching phonons of the Si-layer. In alkali-earth intercalated graphites, CaC_6 and SrC_6, the so-called *interlayer* bands are filled and experience significant electron-phonon (e-ph) interaction to the out-of-plane buckling vibrations of the honeycomb layers [1].

CaAlSi belongs to a class of recently synthesized ternary alloys, formed by Al and Si atoms sitting on graphene-like sheets, and alkaline-earth atoms (Ca, Sr, Ba) intercalated between them. CaAlSi and SrAlSi are superconducting, with a T_c of 7.8 K and 5.4 K respectively, while BaAlSi is not down to 0.3 K [2]. Like in CaC_6 and SrC_6, the superconductivity is mainly due to the interaction of 'interlayer' and $\pi^\star$ electrons with the out-of-plane vibrations of the honeycomb layers; the σ-bands are completely full and do not contribute to the pairing [3].

CaAlSi has recently attracted considerable interest, because it exhibits an ultrasoft phonon mode and crystalizes with several stacking variants. Thermodynamic experiments on polycrystals have revealed unexpected differences between CaAlSi and the isoelectronic and isostructural SrAlSi. Whereas SrAlSi behaves like a standard weak-coupling BCS superconductor, CaAlSi is in the strong-coupling limit. Furthermore, T_c *decreases* with pressure in SrAlSi, and *increases* in CaAlSi. *Ab initio* calculations, and later neutron scattering experiments, have shown that an ultrasoft phonon mode exists in CaAlSi, but not in SrAlSi, which can explain the observed differences. These *ab initio* calculations so far, and analyses of the experimental data based thereon, have assumed that the stacking of Al-Si planes along the *c*-axis is either uniform or completely disordered.

However, recent X-ray diffraction experiments on nH-CaAlSi single crystals revealed several stacking variations of the Al–Si layers, denoted as A and B in the following (see Fig. 67). The A- and B-layers differ by a 60° rotation around the *c*-axis. Besides the simple 1H structure characterized by a |A|A|A|... stacking, two more stacking variants were found: 5H with a AABBB and 6H with a AAABBB sequence. Stacking of the A- and B-layers induces internal stress on the structure, causing buckling of *boundary layers*, i.e., layers with an unlike neighboring layer.

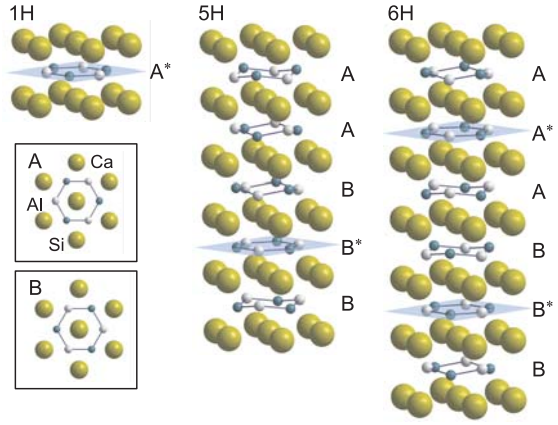

Figure 67: Crystal structure of 1H-, 5H- and 6H–CaAlSi, which are characterized by a different sequence of A- and B-layers. A- and B-layers are rotated by 60° around the *c*-axis with respect to each other. Flat and buckled Al-Si layers are indicated with and without an asterisk, respectively.

We have investigated the effects of pressure on the superconducting properties of nH-CaAlSi by experiments on single crystals and *ab initio* linear-response calculations of their e-ph properties [4]. This has allowed us to understand the interplay between stacking variants, soft modes and superconductivity in nH-CaAlSi.

Our measurements reveal that the pressure variation of T_c in nH-CaAlSi strongly depends on the stacking sequence. Figure 68 shows the temperature dependence of the magnetic susceptibility ($\chi(T)$) of nH-CaAlSi single crystals under pressures up to ≈ 10 kbar. At ambient pressure, the T_c's of 1H-, 5H-, and 6H-CaAlSi are 6.50 K, 5.95 K, and 7.89 K, respectively, consistent with previous reports [2]. For 1H-CaAlSi, T_c *decreases* linearly with a rate of $\Delta T_c/T_c = -0.03$ K/kbar. In contrast, the pressure dependence in 5H-CaAlSi is slightly nonlinear with an initial slope of +0.013 K/kbar, while 6H-CaAlSi exhibits a more pronounced nonlinear behavior and saturation at $T_c \approx 7.95$ K already at ≈ 10 Kbar.

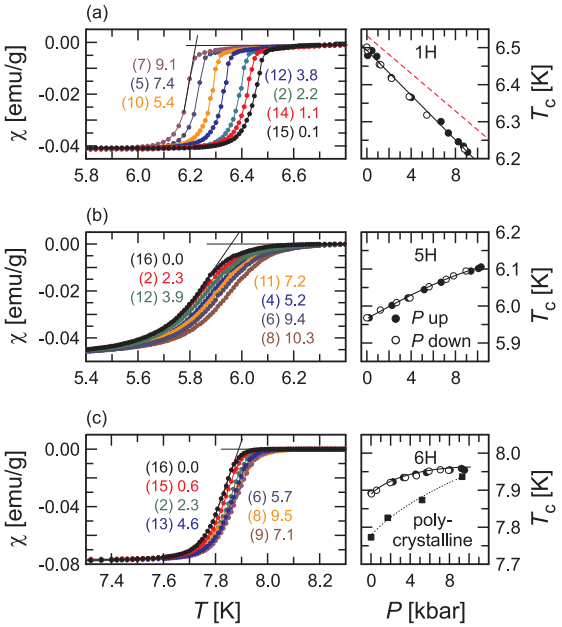

Figure 68: (color online) Left: Temperature dependence of the susceptibility for CaAlSi single crystals at different pressures. The numbers next to the data and in the parenthesis correspond to the applied pressure (kbar) and the sequential order of the measurement runs, respectively. The extrapolation method to determine T_c is demonstrated with solid lines. Right: Pressure dependence of T_c for (a) 1H-, (b) 5H-, (b) 6H-CaAlSi single crystals. For comparison we plot the previous data for polycrystalline sample from [5] in (c) and the theoretical curve for $T_c(P)$ in (a) for 1H-CaAlSi with (red) dashed line.

The decrease of T_c with P in 1H-CaAlSi is adverse both to previous reports on polycrystalline samples and to an existing *ab initio* study which predicts an abrupt increase of T_c accompanied by a lattice instability. The behavior of T_c with P in 5H- and 6H-CaAlSi suggests that also in these variants a phonon softening occurs.

Our *ab initio* calculations confirm that indeed a strong phonon softening occurs in all the identified stacking variants of CaAlSi, and that this is not sufficient to lead to an increase of T_c with P in 1H-CaAlSi. We calculated the structural, electronic and vibrational properties of nH-CaAlSi as a function of pressure, up to 100 kbar. Besides the identified 1H, 5H and 6H stacking variants, we also considered hypothetical 2H- and 3H-CaAlSi, characterized by an |AB|AB| and |AAB|AAB| stacking of the Al-Si planes, respectively. In sign and magnitude, our calculations correctly reproduce the corrugation ('buckling') of the Al-Si planes in the 5H- and 6H-structures; a corrugation is also obtained for 3H-CaAlSi.

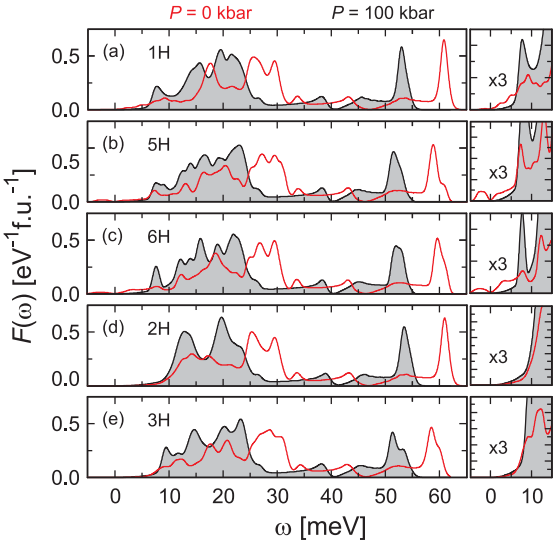

Figure 69: (color online) Linear Response Phonon DOS (phDOS) for different nH-CaAlSi at $P = 0$ and $P = 100$ kbar; in the right sub-panel we show an enlargement of the low-energy region.

In Fig. 69, we display the phonon density of states (DOS) of nH-CaAlSi, calculated at the theoretical equilibrium pressure ($P = 0$) and at the highest pressure considered (100 Kbar). At $P = 0$, the 1H, 5H and 6H stacking variants all show a peak at ≈ 7 meV, associated with the out-of-plane vibrations of the Al-Si planes. Under pressure, roughly one half of the corresponding phonon states soften and drive the system to a structural instability at $P \approx 80$ Kbar. The hypothetical 2H-CaAlSi and 3H-CaAlSi, on the other hand, do not display the ultrasoft phonon peak at $P = 0$, and all phonon modes harden with increasing pressure.

The softening of a single phonon mode can in some cases lead to an increase of T_c with pressure. According to Hopfield's formula, the partial electron-phonon coupling associated to a single phonon mode is given by:

$$\lambda = \frac{N(\varepsilon_F) D^2}{M\omega^2}, \qquad (10)$$

where $N(\varepsilon_F)$ is the electronic DOS at the Fermi level, D is the deformation potential, and $M\omega^2$ is twice the phonon force constant.

Usually, $N(\varepsilon_F)$ decreases and ω increases with P, leading to a net decrease of λ and hence T_c. This is what happens, for example, in 2H- and 3H-CaAlSi. However, if ω of one particular phonon decreases with P, it is possible to have a net increase of T_c, if the coupling of the electrons is sufficiently strong to overcome the opposing effect of the other phonons and of the DOS.

A careful linear response calculation of the full electron-phonon spectral function $\alpha^2 F(\omega)$ as a function of P shows that this does not happen in 1H-CaAlSi. In Tab. 3, we report the T_c of 1H-CaAlSi, estimated via the McMillan formula,

$$T_c = \frac{\langle\omega_{ln}\rangle}{1.2} \exp\left[\frac{-1.04(1+\lambda)}{\lambda - (1+0.62\lambda)\mu^*}\right], \qquad (11)$$

where ω_{ln} is the logarithmic-averaged phonon frequency and $\mu^\star$ is the Coulomb pseudopotential, fixed to $\mu^\star = 0$ in the following.

Table 3: Calculated superconducting properties of 1H-CaAlSi as a function of pressure. T_c was obtained by the McMillan formula, with $\mu^\star = 0.1$. For comparison, we give in parentheses the results for 2H.

P [Kbar]	$\langle\omega_{ln}\rangle$ [K]	λ	T_c [K]
0	139.2 (160)	0.73 (0.60)	5.35 (3.66)
20	139.9 (186)	0.70 (0.47)	4.86 (1.75)
40	134.0 (200)	0.70 (0.43)	4.65 (1.24)

The temperature T_c is seen to decrease with P, with $\Delta T_c/dP = -0.02$ K/kbar, in nice agreement with the experiments. This is due to a delicate balance between $\langle\omega_{ln}\rangle$ and λ. For comparison, in the same table we also show the data for 2H-CaAlSi, which shows a much more usual behavior.

For 5H- and 6H-CaAlSi, due to their very large unit cells (15 and 18 atoms, respectively), and the extreme sensitivity of the results to computational parameters, we did not perform a full e-ph calculation. Although there are some subtle differences in the electron and phonon dispersions, their electronic DOS's and soft mode phonon frequencies decrease with the same rate as in 1H-CaAlSi. For this reason, we assume that their $\alpha^2F(\omega)$'s have very similar characteristics to that of 1H-CaAlSi. A simple model, based on a Gaussian decomposition of the $\alpha^2F(\omega)$ of 1H-CaAlSi, shows that the different pressure dependence of T_c for 5H and 6H can be explained assuming an increasing behavior of the spectral weight for the ultrasoft phonon mode under pressure. This could reflect either small differences in the electron-phonon matrix elements due to the buckling of some planes, or a different number of phonon modes that soften under pressure.

Our calculations thus show the identified stacking variants of nH-CaAlSi have very similar electronic and vibrational properties; the differences in their superconducting properties reflect small details of the e-ph interaction. In contrast, the hypothetical systems 2H- and 3H-CaAlSi show a completely different behavior. First, they are energetically disfavored with respect to existing stacking variants, because of a non-optimized energy balance between the formation of AB interfaces and buckling. Second, they do not display any soft phonon modes, which only appear if three or more Al atoms arrange in a sequence along the *c*-axis.

[1] *Calandra, M. and F. Mauri.* Physical Review Letters **95**, 237002 (2005); *Kim, J.S., L. Boeri, J.R. O'Brien, F.S. Razavi and R.K. Kremer.* Physical Review Letters **99**, 027001 (2007); *Kim, J.S., R.K. Kremer, L. Boeri and F.S. Razavi.* Physical Review Letters **96**, 217002 (2006); *Kim, J.S., L. Boeri, R.K. Kremer and F.S. Razavi.* Physical Review B **74**, 214513 (2006); *Boeri, L., G.B. Bachelet, M. Giantomassi and O.K. Andersen.* Physical Review B **76**, 064510 (2007); or see also the Annual Report of the Max-Planck-Institut für Festkörperforschung (2006) and references therein.

[2] *Imai, M., K. Nishida, T. Kimura and H. Abe.* Applied Physics Letters **80**, 1019–1021 (2002); *Lorenz, B., J. Cmaidalka, R.L. Meng and C.W. Chu.* Physical Review B **68**, 014512 (2003); *Sagayama, H., Y. Wakabayashi, H. Sawa, T. Kamiyama, A. Hoshikawa, S. Harjo, K. Uozato, A.K. Ghosh, M. Tokunaga and T. Tamegai.* Journal of the Physical Society of Japan **75**, 043713 (2006).

[3] *Mazin, I.I. and D.A. Papaconstantopoulos.* Physical Review B **69**, 180512(R) (2004); *Giantomassi, ,M., L. Boeri and G.B. Bachelet.* Physical Review B **72**, 224512 (2005); *Huang, G.Q., L.F. Chen, M. Liu and D.Y. Xing.* Physical Review B **69**, 064509 (2004); *Huang, G.Q., L.F. Chen, M. Liu and D.Y. Xing.* Physical Review B **71**, 172506 (2005); *Heid, R., K.-P. Bohnen, B. Renker, P. Adelmann, T. Wolf, D. Ernst and H. Schober.* Journal of Low Temperature Physics **147**, 375–386 (2007).

[4] *Boeri, L., J.S. Kim, M. Giantomassi, F.S. Razavi, S. Kuroiwa, J. Akimitsu and R.K. Kremer.* cond-mat/0712.2955.

[5] *Lorenz, B., J. Cmaidalka, R.L. Meng and C.W. Chu.* Physical Review B **68**, 014512 (2003).

Electron interactions and unusual electronic properties

Electron interactions often lead to states at low temperature with surprising properties ranging from peculiar spin and/or charge order to superconductivity or the quantum Hall effect. Each case poses a new challenge to the scientists to unravel the secrets of the particular system or compound. The first contribution reports the fascinating onset of a drag current in one bilayer sheet if a current flows through the other layer. The remarkable effect is attributed to exciton condensation and occurs only if the filling fraction of the individual layers is close to 1/2. A new class of ternary oxides formed by trigonal $[NiO_2]^-$ layers poses a new challenge, as orbital degeneracy of Ni^{3+} and Jahn-Teller distortions conspire and complex magnetic structures emerge. The third contribution analyzes the appearance of the anisotropic Seebeck effect in colossal magnetoresistant manganite thin film, while the following contribution reports a giant amplification of the splitting of energy levels due to spin-orbit interaction for Bi atoms embedded in a Ag(111) surface. By means of angular resolved photoemission the spin-splitting of unprecedented magnitude can be visualized. The last but one contribution deals with the effect of spin-orbit coupling on the electronic structure of the semimetals Bi and Sb. It is shown that spin-orbit coupling must be considered in ab initio calculations of thermodynamic properties of such compounds to arrive at a quantitative agreement with experimental data. The unexpected discovery of superconductivity in MgB_2 has stimulated the investigation of the electronic structure of sp^2-bonded solids in order to understand the origin of superconductivity. The concluding article in this section explains the subtle differences of the electronic structures of the related superconductors α- and β-$ThSi_2$.

Exciton condensate at a total filling factor of one in Corbino 2D electron bilayers

L. Tiemann, J.G.S. Lok, M. Hauser, W. Dietsche and K. v. Klitzing

Exposed to a strong perpendicular magnetic field B, the density of states of a two-dimensional electron system (2DES) will condense into a discrete set of sub-bands, the Landau levels. The total number of occupied states is then parameterized by the filling factor $\nu = \frac{hn}{eB}$, where n is the electron density. The design of samples which consists of two closely spaced 2DES that can be contacted independently is the foundation to create a novel quantum Hall (QH) state. This new QH state which is governed by Coulomb interactions occurs when the filling factors of both 2DES are simultaneously at 1/2 (i.e., at a *total* filling factor of 1). The double-layer system can then be viewed as a Bose condensate of interlayer quasi-excitons by coupling an electron from layer 1 to a vacant state from layer 2 and vice versa. Both theoretically and experimentally it is found that this condensate in bilayers occurs when the ratio of the layer separation d and the magnetic length $l_B = \sqrt{\hbar/eB}$ is smaller than ≈ 2.

Interlayer drag experiments on Hall bars have revealed a Hall drive and drag which approaches a quantized value of h/e^2. The quantization of the Hall drag is an indirect indication of a superfluid mode of excitons. We performed these drag measurements for the first time on a *quasi*-Corbino electron bilayer system with independent contacts to both layers. We observe

that at a total filling factor of 1 ($\nu_{tot} = 1$) a voltage develops in the drag layer that equals in sign and magnitude the voltage across the drive layer, and at lowest temperatures, the conductance of the drive layer vanishes. Due to the absence of sample edges connecting source and drain contacts in a ring, the current is driven selectively through the bulk of the $\nu_{tot} = 1$ system.

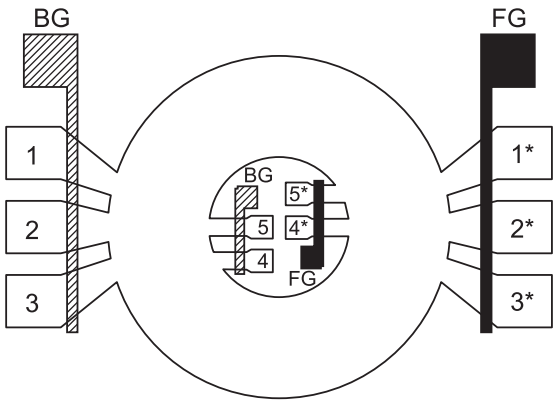

Figure 70: Schematic view of the Corbino geometry that was used in the experiment. Application of appropriate voltages to the back gates (marked as 'BG') and front gates ('FG') will lead to contact separation, i.e., contacts 1 through 5 will connect to the upper quantum well and 1^* through 5^* to the lower one.

We employ a quasi-Corbino geometry with four contact arms attached to each ring as depicted in Fig. 70. The back gates were patterned *ex situ* from a Si-doped GaAs epilayer before growing an insulating GaAs/AlGaAs superlattice and the bilayer on top. Separate contacts to the two layers are achieved by applying appropriate negative voltages to the buried back gates and metallic front gates which cross the contact arms. One set of contacts can then be used to pass a current and another one to measure the voltage across the ring. The density in each layer can be adjusted independently by using another set of front and back gates (not shown).

Figure 71 plots the measured (radial) current in the drive layer and the corresponding drive and drag voltages as a function of the magnetic field at lowest temperatures. The electron densities in the two layers were adjusted to be equal, producing a total density of $4.8{\cdot}10^{14}\,\mathrm{m}^{-2}$. Below 1.5 T, the current oscillates reflecting the varying filling factors and integer QH states. At a total filling factor of 1 which occurs here at about 2.0 T, we observe a strong minimum in the current like at the ordinary QH states at lower magnetic fields. As a result, the voltage drop over the drive layer almost equals the source voltage (Fig. 71(a)). Meanwhile, a large drag voltage develops over the region of the correlated $\nu_{tot} = 1$ phase, with the sign and magnitude identical to that of the drive layer. Since the radial component of the current in the drive layer is nearly zero, one possible explanation for the observed drag voltage is the existence of an azimuthal (i.e., circling) current in the drive layer, in analogy to the ordinary QH states.

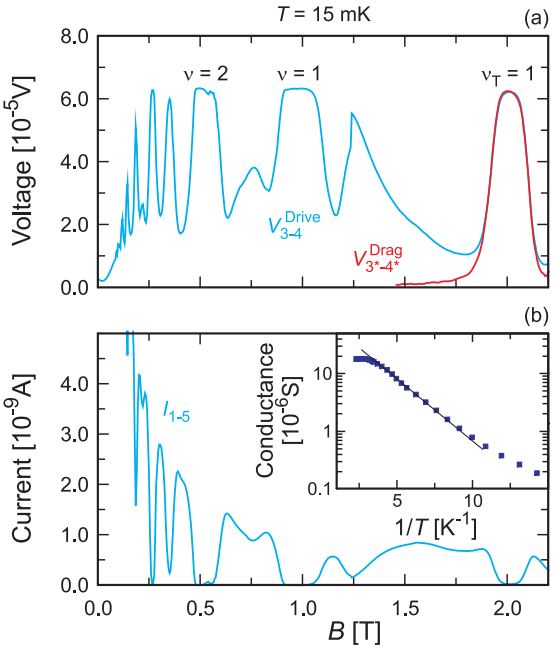

Figure 71: (a) Measured drive (blue) and drag (red) voltages at $T_{bath} = 15$ mK. The (integer) filling factors $\nu \leq 2$ and $\nu_{tot} = 1$ ($d/l_B = 1.62$) are labeled. (b) Measured current in the drive layer. The inset plots the temperature dependence of the radial conductance G; the line is a fit using $G \propto \exp(-E_{gap}/T)$.

Owing to the excitonic coupling it would trigger an azimuthal current of the same magnitude in the drag layer, leading to identical voltages across both layers. However, we neither know the nature of this excitonic current nor

where it flows. It could be homogeneously distributed throughout the bulk or rather concentrated at the sample edges. Nevertheless, the well-established model of electron-hole pairing around $\nu_{tot} = 1$ implies that such a transport mode in Corbino bilayers might be possible. Supported is that notion by the fact that the Ohmic contacts of the drag layer in our geometry are located at the opposite side of the ring, i.e., approximately 1 mm away from the Ohmic contacts of the drive layer. In previous drag experiments using a standard Hall bar geometry, identical Hall voltages in the drag and drive layers were also considered to be signaling the underlying excitonic superfluidity.

Figure 72 plots data taken at a temperature of $T = 0.25$ K. The densities in both layers are still equal but reduced to a total electron density of approximately $4.2{\cdot}10^{14}\,\mathrm{m}^{-2}$. Now $\nu_{tot} = 1$ occurs at $B = 1.76$ T which corresponds to $d/l_B = 1.49$. At 0.25 K the minimum in the current has almost entirely disappeared (Fig. 72(b)). Nonetheless, there is still a sizeable peak in the drive voltage at $\nu_{tot} = 1$ (blue line in Fig. 72(a)). Surprisingly, the voltage over the drag layer (red line) also displays a peak *with the same amplitude*. This striking observation of a nearly doubled dissipation in the drive layer accompanied by an identical drag voltage can be interpreted as evidence that both layers are in a state of commencing interlayer correlation.

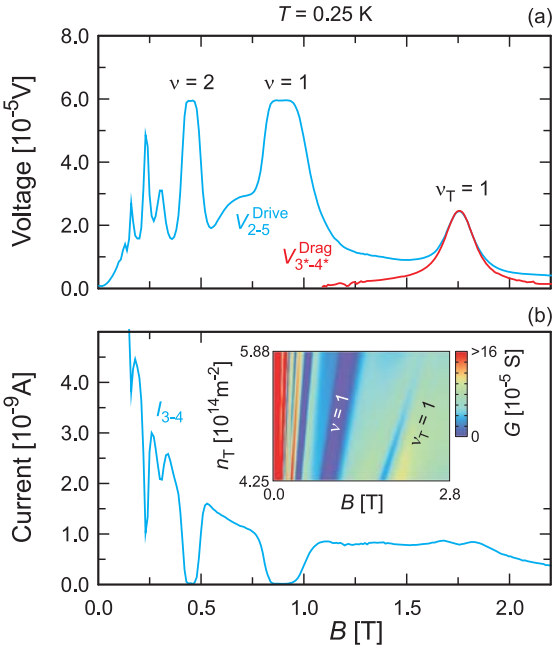

Figure 72: (a) Drive (blue) and drag (red) voltage versus the magnetic field at $T = 0.25$ K. (b) The current in the drive layer measured simultaneously. The inset illustrates the conductance G of the drive layer as a function of the magnetic field and the total density. Clearly visible is how the conductance at $\nu_{tot} = 1$ decreases as the total density n_{tot} is reduced.

In conclusion, we have conducted interlayer drag experiments on a quasi-Corbino electron bilayer system. At the lowest temperature and strong coupling, drag and drive voltages are identical while the conductance in the drive layer vanishes. These data imply a circular potential distribution along the sample edges owing to a circling (azimuthal) excitonic current in both layers.

Jahn-Teller distortion vs. charge ordering in trigonal $[NiO_2]^-$ layers

U. Wedig, M. Sofin, T. Sörgel, J. Nuss and M. Jansen

Ternary oxides of the delafossite type are exceptionally well suited to study spin and orbital ordering phenomena. They consist of transition metal oxide sheets where the edge sharing octahedra form a triangular lattice. These sheets are intercalated by layers of alkaline or group 11 elements. In the case of $[NiO_2]^-$ sheets with Ni^{3+} ions in the low spin state ($t_{2g}^6\, e_g^1$), distortions lifting the orbital degeneracy are expected to occur, in addition to a complex spin

structure at low temperatures, caused by frustration. Different ordering patterns may arise from the interaction with the diverse intercalating layers. Indeed, many of these compounds show several phase transitions. However, the detection of small structural changes induced by the ordering phenomena require availability of high quality crystals and sophisticated synthesis routes.

In $NaNiO_2$, prepared via the azide/nitrate route [1], a Jahn-Teller distortion is observed at temperatures below 470 K. The set of six equivalent Ni–O bonds in the high-temperature phase splits into 4 bonds of length 1.913 Å and 2 bonds of length 2.159 Å. Below 18 K, $NaNiO_2$ becomes an A-type antiferromagnet, i.e., the spin order is ferromagnetic within the $[NiO_2]^-$ sheets and antiferromagnetic between them.

Like $NaNiO_2$, Ag_2NiO_2 undergoes two phase transitions, at $T = 56$ K and $T = 260$ K, respectively [2]. Ag_2NiO_2 can be synthesized by a solid state reaction at high oxygen pressure [3] or via electrochemical intercalation of the 3R-polytype of $AgNiO_2$ [4]. In contrast to $AgNiO_2$, the $[NiO_2]^-$ sheets are separated by close packed double-layers of subvalent silver. The intercalation of an additional Ag-layer, however, affects neither the geometric nor the electronic structure of the $[NiO_2]^-$ sheets substantially, as has been confirmed by photoelectron spectroscopy, XANES measurements and quantum mechanical calculations [5].

In both compounds a broad valence band with sizeable Ag 5*s*/5*p* character crosses the manifold of Ag 4*d*, Ni 3*d* and O 2*p*-bands. The partial occupancy of Ag 5*s*/5*p* in 3R-$AgNiO_2$ is compensated by vacancies in the 4*d*-shell, which also can be seen in the Ag L_{III}-edge XANES spectrum, and which leads to metallic conductivity in this compound. The conductivity in Ag_2NiO_2 is, by one order of magnitude, larger due to the subvalent nature of the silver atoms.

By a thorough analysis of the X-ray diffraction data recorded for Ag_2NiO_2 at 100 K, a Jahn-Teller distortion could be established. As a result of the twin refinement of a monoclinic structure (*C*2/*m*), two sets of bond distances were found in the NiO_6 octahedra, 4×1.937 Å and 2×2.027 Å (Fig. 73). This distortion is similar to the one observed in $NaNiO_2$, although smaller in magnitude.

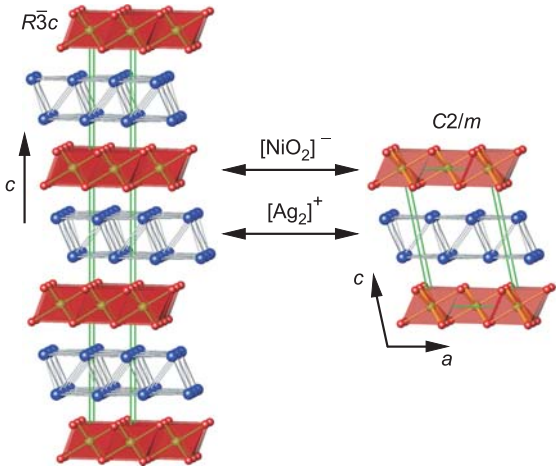

Figure 73: Rhombohedral ($R\bar{3}m$, left) and monoclinic (*C*2/*m*, right) structures of Ag_2NiO_2. The short Ni-O distances in the monoclinic structure are marked by thick, the long ones by thin sticks.

According to band structure calculations using a hybrid functional, an A-type antiferromagnetic order is also possible in Ag_2NiO_2. The high Néel temperature of Ag_2NiO_2 (56 K) suggests even a further stabilization due to a RKKY type interaction between the spins mediated by a polarization of the itinerant electrons in the silver double-layer. The magnetic order within the sheets, however, need not be ferromagnetic. Calculations with a sixfold monoclinic supercell result in a ferrimagnetic honeycomb like spin density (Fig. 74).

A completely different ordering pattern is observed in 2H-$AgNiO_2$, a stacking variant of 3R-$AgNiO_2$. The pure polytype 2H-$AgNiO_2$ was synthesized by oxidizing a co-precipitate of nickel nitrate and silver nitrate, which was subsequently recrystallized under high oxygen pressure [6]. Neutron diffraction patterns of a powder sample were recorded at the ISIS neutron source [7]. The main peaks are consistent with the hexagonal space group $P6_3/mmc$ as deduced from X-ray diffraction.

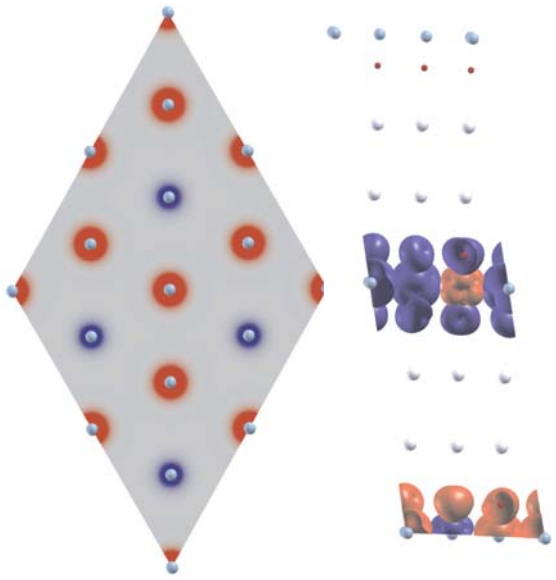

Figure 74: Spin density of Ag_2NiO_2 in a sixfold monoclinic supercell as obtained from a hybrid functional calculation (10% HF-exchange, program CRYSTAL98).

Additional peaks indicate a tripled unit cell in the $[NiO_2]^-$ sheets. The resulting structure ($P6_322$) contains three inequivalent Ni sites. Each single NiO_6 octahedron has six equal Ni–O distances. The coordination polyhedra around Ni2 and Ni3 are shrunk, those around Ni1 expanded (Fig. 75).

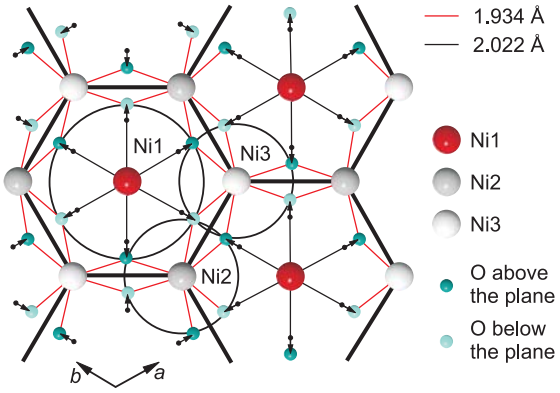

Figure 75: Charge ordered $[NiO_2]^-$ layers in 2H-$AgNiO_2$ with enlarged (Ni1) and contracted (Ni2, Ni3) NiO_6 polyhedra.

These changes can be explained by a charge ordering scenario, where Ni1 is electron enriched (Ni^{2+}) and both Ni2 and Ni3 are electron depleted ($Ni^{3.5+}$). Additional peaks in the neutron diffraction pattern below 20 K indicate a novel magnetic structure. The spins of the Ni1 ions (S = 1) are arranged in alternating ferromagnetic rows that are surrounded honeycomb-like by the nonmagnetic Ni2 and Ni3 ions (Fig. 76). Recent zero field muon-spin relaxation experiments have confirmed this model [8].

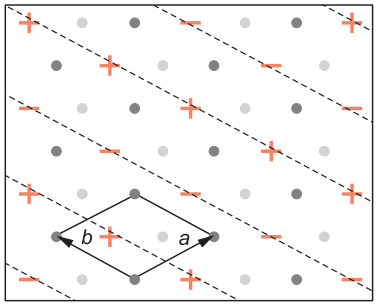

Figure 76: Magnetic structure within the $[NiO_2]^-$ layers of 2H-$AgNiO_2$. The spins at the Ni1 sites are arranged in alternating ferromagnetic stripes.

Although the $[NiO_2]^-$ sheets in the compounds presented here appear to be virtually identical at a first glance, more detailed investigations show various responses of the system to orbital degeneracy and spin frustration. As a consequence, a particular ordering scheme cannot be understood on the basis of a single $[NiO_2]^-$ sheet alone, but the coupling mechanisms via the intercalating ions also have to be considered.

[1] *Sofin, M. and M. Jansen.* Zeitschrift für Naturforschung B **60**, 701–704 (2005).

[2] *Yoshida, H., Y. Muraoka, T. Sörgel, M. Jansen and Z. Hiroi.* Physical Review B **73**, 020408 (2006).

[3] *Schreyer, M. and M. Jansen.* Angewandte Chemie International Edition **41**, 643–646 (2002).

[4] *Sörgel, T.* Thesis, University of Stuttgart (2006).

[5] *Wedig, U., P. Adler, J. Nuss, H. Modrow and M. Jansen.* Solid State Sciences **8**, 753–763 (2006).

[6] *Sörgel, T. and M. Jansen.* Zeitschrift für anorganische und allgemeine Chemie **631**, 2970–2972 (2005).

[7] *Wawrzyńska, E., R. Coldea, E.M. Wheeler, I.I. Mazin, M.D. Johannes, T. Sörgel, M. Jansen, R.M. Ibberson and P.G. Radaelli.* Physical Review Letters **99**, 157204 (2007).

[8] *Lancaster, T., S.J. Blundell, P.J. Baker, M.L. Brooks, W. Hayes, F.L. Pratt, R. Coldea, T. Sörgel and M. Jansen.* Physical Review Letters **100**, 017206 (2008).

Mesoscopic phase separation and the anisotropic Seebeck effect in $La_{0.67}Ca_{0.33}MnO_3$ thin films

P.X. Zhang and H.-U. Habermeier

Investigations of perovskite-type doped rare earth manganites, which demonstrate the colossal magnetoresistance (CMR) effect, have revealed a large amount of novel properties of condensed matter characterized by strong electron correlation. The manganites can serve as a prototype material for basic studies of strong electron correlation and electron-lattice coupling effects representing a candidate for potential spintronic device applications: One of the most important recent discoveries in this type of material is the coexistence and/or competition of several phases at the nanoscale level, commonly described as mesoscopic phase separation [1]. This phase separation has been predicted theoretically and has been proven experimentally in several material systems such as cuprates, vanadates and titanates [1]. It appears to be a general feature of compounds with strong electron correlations in which cations surrounded by oxygen octahedra occur in a valence state where Jahn-Teller distortions are present and consequently a strong coupling of the lattice with the electronic system is taking place. The coexistence and/or competition of phases are a consequence of the complexity of electronic and electron-lattice interactions at comparable energy scales. Taking $La_{0.67}Ca_{0.33}MnO_3$ as a prototype, several possible new phases have been identified such as the charge ordered (CO) and orbital ordered (OO) antiferromagnetic (AF) insulating phases with different ordered structures.

The coexistence of these phases with the ferromagnetic metallic (FMM) one, and the percolation of the FMM domains with temperature or magnetic field is considered to be the main reason for the CMR effect. Therefore, the study of the physical properties, especially the transport properties, of these materials in a parameter range where these new phases coexist is very critical for understanding related mechanisms such as the CMR effect. It was reported that these new phases exist near and even above the Curie temperature, T_{Curie}. Due to the nanoscale nature of phase separation and the similarity of the crystal structure of these coexistent phases, information obtained by most of the volume averaging experiments such as simple transport and magnetization measurements, neutron scattering, ESR, and X-ray diffractometry, are barely suitable to investigate these inhomogeneities. Local probes such as scanning tunneling microscopy or high-resolution electron microscopy (TEM) are either surface sensitive, only, or the bulk properties are potentially altered by the special destructive preparation required for TEM samples. Therefore, alternative techniques are required to shed some light on the phase separation problem, even if they give information only indirectly. The competition of these different phases starts at a temperature higher than the transition temperature T_{Curie} and so far there is little information available in the literature focusing on this temperature range. To our knowledge, there are neither magnetic nor transport measurements known, addressing the question of anisotropy in manganites either intrinsic or phase separation induced, even for the model composition of $La_{0.67}Ca_{0.33}MnO_3$.

We performed a new experiment, which provides information on anisotropic transport properties in any material in a wide temperature range including the regime interesting for CMR materials near and above T_{Curie}. We demonstrate for the first time that there is clear evidence of transport anisotropy arising from anisotropy in the Seebeck coefficients in the nominally cubic paramagnetic phase at temperature above T_{Curie} in $La_{0.67}Ca_{0.33}MnO_3$. This anisotropic transport property is regarded to be closely connected to a special charge ordered antiferromagnetic phase.

The experiment is based on the laser induced transient voltage effect (LITV), discovered in 1990 in $YBa_2Cu_3O_7$ thin films [2]. Several years of investigation unveiled that this effect is due to a thermoelectric response based on the anisotropy of the Seebeck coefficients in $YBa_2Cu_3O_7$. An incident pulsed laser beam heats the surface of the film, the transient temperature difference between top and bottom parts of the film produces a transverse voltage (see Fig. 77) provided nonzero off-diagonal elements of the Seebeck tensor exist.

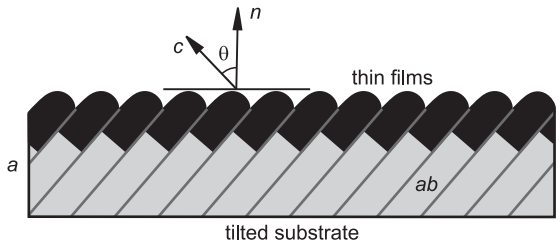

Figure 77: Sketch of an anisotropic thin film on a vicinal cut substrate.

The response signal due to the laser-induced heat pulse is characterized by a peak voltage U_p and its decay time which is due to thermal diffusion. In films grown epitaxially on vicinal cut single crystal substrates such as (100)-oriented $SrTiO_3$, the projection of the Seebeck tensor to the surface plane of the substrate reveals off-diagonal elements of the form $0.5(S_{ab}-S_c)\sin(2\Theta)$, where S_{ab}, and S_c are the Seebeck coefficients in the plane and perpendicular to the unit cell of the material and Θ is the angle between the substrate normal and *c* direction of the unit cell (see Fig. 77). Lengfellner *et al.* derived a formula to describe the effect quantitatively [3]:

$$U_x = 0.5\,(S_{ab}-S_c)\sin(2\Theta)\,\nabla_z T \qquad (12)$$

Here, U_x corresponds to the induced voltage in *x*-direction, *l* and *d* are the length and thickness of the film, respectively (see Fig. 77) $\nabla_z T$ is the temperature gradient perpendicular to the film plane produced by laser irradiation. One specific feature of this LITV effect is the $\sin(2\Theta)$ dependence of the induced voltage, which is unique and does not appear in other photo-induced effects, one can thereby identify the nature of induced voltage as the thermoelectric anisotropy.

During our investigations of the CMR effect in $La_{0.67}Ca_{0.33}MnO_3$ thin films, we observed the existence of substantial large LITV signals when films grown on vicinal cut substrates are exposed to pulsed photon beams at room temperature [4]. This observation was a surprise at the beginning since the crystal structure is cubic or quasi-cubic (some lattice distortions may occur due to substrate lattice mismatch), and the film is in the paramagnetic state where no magnetization-induced anisotropy is expected and consequently the difference $(S_{ab}-S_c)$ should vanish. This puzzle can be solved by introducing in analogy to the phase separation picture a two phase model, applicable especially in the temperature range near and above T_{Curie}.

Assuming that there are two competing phases, the ferromagnetic metallic (FMM) and charge ordered antiferromagnetic (COAF) insulating phase, whose volume fraction changes with temperature, the total induced voltage is composed of the contribution of the two:

$$U_p(T) = A[(1-c(T))\,\Delta S_{COAF}(T) + \\ + c(T)\,\Delta S_{FMM}(T)] \qquad (13)$$

Here, $U_p(T)$ corresponds to the peak value of the induced voltage, ΔS_{COAF} and ΔS_{FMM} are defined as $(S_{ab}-S_c)$ in the COAF and FMM phases, respectively, and $c(T)$ is the temperature dependent fraction of the FMM phase. A is a constant related to the geometry of the sample and the temperature gradient produced by the pulsed laser beam. The Seebeck coefficients are known to be temperature dependent, thus, in a first approximation, we treat their anisotropy $(S_{ab}-S_c)$ analogously. Provided no structural phase transitions take place in the interesting temperature range – which applies for the $La_{0.67}Ca_{0.33}MnO_3$ as far as bulk measurements reveal – two extreme cases can be

discussed. At $T \gg T_{\mathrm{Curie}}$, the FMM phase disappears, c approaches zero, and according to equation (2) the only reason for a LITV effect is due to the Seebeck anisotropy arising from the COAF phase. At $T \ll T_{\mathrm{Curie}}$, the material is completely in the ferromagnetic metallic phase, the contribution of COAF phase is negligibly small and a measured LITV signal is attributed to the Seebeck anisotropy of the FMM phase.

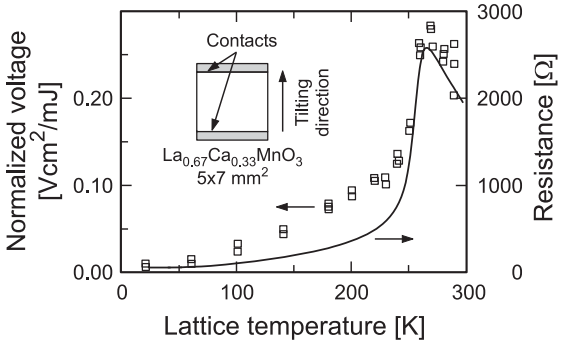

Figure 78: Temperature dependence of the LITV signal of a 150 nm thick $La_{0.67}Ca_{0.33}MnO_3$ thin film deposited on to a $SrTiO_3$ (100)-oriented substrate with a miscut of 10^0 vs. [010]. (The signal is normalized to the photon fluency of the illuminating laser beam $\lambda = 248$ nm).

Figure 78 shows the LITV experimental results obtained from $La_{0.67}Ca_{0.33}MnO_3$ thin films grown on vicinal cut STO substrates showing a remarkable large signal around T_{Curie} and a vanishing one at low temperatures. (The signal is normalized to the photon fluency of the illuminating laser beam.) According to these results, ΔS_{COAF} (high-T) = 0.2/A and ΔS_{FMM} (low-T) = 0.01/A resulting in an anisotropy ratio ΔS_{COAF} (high-T)/ΔS_{FMM} (low-T) = 20. Qualitatively, this result suggests that the COAF phase is anisotropic whereas the FMM phase remains cubic with an anisotropy close to zero. Considering the close relation of the Seebeck coefficient and the conductivity

$$S = -(\pi^2/3)(k_B^2 T/e)[\sigma'(E_F)/\sigma(E_F)] \qquad (14)$$

($\sigma(E_F)$ is the conductivity at Fermi level, and $\sigma'(E_F) = \delta\sigma/\delta E$, k_B and e are the Boltzmann's constant and the elementary charge) an approximation of Eq.(14) for Seebeck coefficients in most of metallic and insulating system can be expressed as $\Delta S/S \sim \Delta\rho/\rho$. For the two coexistent phases near and above T_c, the FMM phase has a low resistivity, therefore small Seebeck coefficients, while the COAF phase is insulating with large resistivity, and thus exhibits a large Seebeck coefficient. Considering in addition the anisotropy ratio ΔS_{COAF}(high-T)/ΔS_{FMM}(low-T) = 20, one can further simplify Eq.(13) to:

$$U_p(T) = A[(1 - c(T)]\,\Delta S_{\mathrm{COAF}}(T)\,.$$

This approximation is valid in the temperature range near and above T_c. Since $c(T)$ can be determined from measurements of the temperature dependence of the magnetization $c(H,T) = M(H,T)/M_{\mathrm{sat}}$, the temperature dependence of $\Delta S_{\mathrm{COAF}}(T)$ easily estimated.

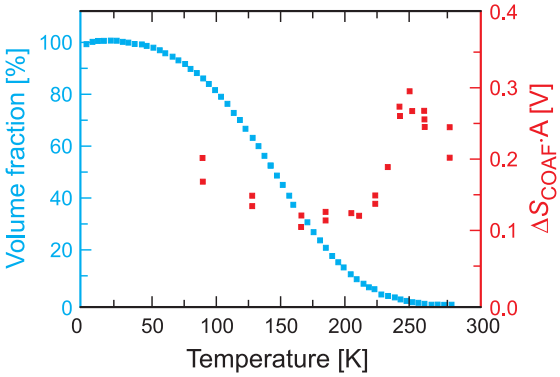

Figure 79: Temperature dependence of Seebeck coefficient anisotropy $\Delta S_{\mathrm{COAF}}(T)$ determined from the measured LITV signal based on a two phases model.

Figure 79 displays the obtained ΔS_{COAF}–T dependence, together with the concentration c of the FMM phase as determined from the magnetization measurements. It is shown that upon lowering the temperature, $\Delta S_{\mathrm{COAF}}(T)$, increases first, reaches a maximum at around T_c, and then decreases. We would like to emphasize that since there are relatively large LITV signals measured above T_c, the anisotropy is robust, and an anisotropic transport behavior is definitely observed above T_c in paramagnetic phase of $La_{0.67}Ca_{0.33}MnO_3$ thin films. This is completely unexpected, since the sample has a cubic structure and is magnetically in the paramagnetic phase.

In summary, a new experimental method – laser induced thermoelectric voltage effect from CMR thin films – was used for the first time to reveal the transport anisotropy at a temperature near and above T_{Curie} the in $La_{0.67}Ca_{0.33}MnO_3$ thin films. By neglecting the contribution of the FMM phase, the temperature dependence of ΔS_{COAF} in the COAF phase was evaluated, providing a clear evidence for the existence of a noncubic, anisotropic phase above T_{Curie}. The results show that the technique using LITV opens a new possibility to investigate intrinsic anisotropies of materials and contribute to the understanding of the electronic properties of materials with complex phase competition and phase coexistence [5].

[1] *Dagotto, E.* in: *Nanoscale Phase Separation and Colossal Magnetoresistance.* Springer Series in Solid State Physics **136**, Springer Verlag, Berlin/Heidelberg, Germany (2003).

[2] *Chang, C.L., A. Kleinhammes, W.G. Moulton and L.R. Testardi.* Physical Review B **41**, 11564–11567 (1990).

[3] *Lengfellner, H., G. Kremb, A. Schnellbögl, J. Betz, K.F. Renk and W. Prettl.* Applied Physics Letters **60**, 501–503 (1992).

[4] *Li, X.H., H.-U. Habermeier and P.X. Zhang.* Journal of Magnetism and Magnetic Materials **211**, 232–237 (2000).

[5] *Yu, L., Y. Krockenberger, I. Fritsch and H.-U. Habermeier.* Progress in Solid State Chemistry **35** 545–551 (2007).

Giant spin-splitting in the Bi/Ag(111) surface alloy

C.R. Ast, G. Wittich, P. Wahl, R. Vogelgesang and K. Kern;
L. Moreschini, M. Falub, D. Pacilé and M. Grioni (EPFL Lausanne, Switzerland)

In nonmagnetic solids, electronic states of opposite spin orientation are often implicitly taken to be degenerate (Kramers' degeneracy). However, spin degeneracy is a consequence of both time-reversal and inversion symmetry. If one of the latter is broken, the degeneracy can be lifted by, e.g., the spin-orbit (SO) interaction. This is, for example, the case in crystals that lack a center of inversion in the bulk (Dresselhaus effect). But also a structural inversion asymmetry, as it shows up at surfaces or interfaces, can lead to spin-split electronic states (Rashba-Bychkov effect). In particular, clean surfaces of noble metals show spin-split surface states, where the splitting increases with the strength of the atomic SO coupling. The splitting can be further enhanced by adsorption of adatoms. Hence, using morphology and chemistry to tune the spin splitting of two-dimensional electronic states is a promising path to create a new class of nanoscale structures suitable for spintronic devices. We have found a new class of materials that exhibits a giant spin splitting in the surface electronic structure [1,2]. Using the concept of surface alloying, the Ag(111) (Z = 47) surface layer was doped with the heavy element Bi (Z = 83). The 2D band structure of the Bi/Ag(111) surface alloy was investigated by ARPES and exhibits a spin splitting of unprecedented magnitude.

In Fig. 80(a) the structure of the surface alloy is shown. Each Bi atom (orange) is surrounded by six Ag atoms (blue), which results in a reconstruction. Fig. 80(b) shows a side view with the outward relaxation of the Bi atoms. The experimental band structure is shown in Fig. 80(c). The characteristic band dispersion due to the spin-splitting showing two singly degenerate parabola-like bands (with negative effective mass), whose maxima are shifted away from the high symmetry point, is clearly visible. The strength of the spin-orbit splitting can be projected onto a momentum scale as well as an energy scale. The corresponding momentum offset $k_0 = 0.13\ \text{Å}^{-1}$ and the Rashba energy

$E_R = 200$ meV are indicated in Fig. 80(c). The large spin-orbit splitting opens up new opportunities for investigation of SO split states.

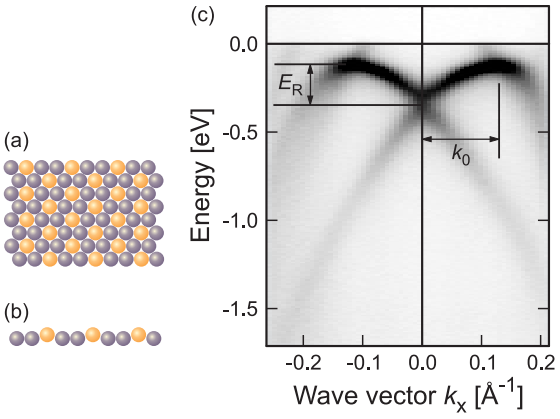

Figure 80: (a) The schematic top view of the $(\sqrt{3}\times\sqrt{3})$R30° Bi/Ag(111) surface alloy (Bi orange, Ag blue). (b) Side view of the schematic, illustrating the outward relaxation of Bi in the surface layer. (c) Experimental band structure obtained by ARPES. The abscissa is the wavevector k_x along the $\overline{\text{M}}$–$\overline{\Gamma}$–$\overline{\text{M}}$ line in the vicinity of the center of the surface alloy Brillouin zone (SBZ; $\overline{\Gamma}$, i.e., $\vec{k}_{||} = 0$). The ordinate gives the energy below the Fermi level (0 eV).

The Rashba-Bychkov model cannot explain the giant SO splitting in the surface alloy. The electronic structure of the Bi/Ag(111) surface alloy was calculated from first principles within the framework of the local spin-density approximation to density-functional theory. A relativistic multiple-scattering approach (layer Korringa-Kohn-Rostoker method), in which spin-orbit coupling is fully accounted via the Dirac equation, was used to compute spin-, layer-, and atom-resolved Bloch spectral densities, hence allowing to characterize the electronic structure in much detail. The result is shown in Fig. 81. It reproduces the features of the experimental band structure quite well, in particular, the size of the spin-orbit splitting.

The calculations show that it is the result of a sizable in-plane gradient of the potential. The in-plane gradient manifests itself in the out-of-plane rotation of the spin polarization, as obtained from the calculations, as well as in a hexagonal shape of the outer branches in the constant energy contours, as obtained from the experiment.

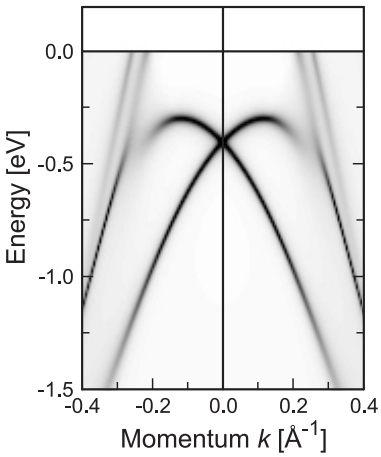

Figure 81: Band structure calculation using density functional theory in the vicinity of the $\overline{\Gamma}$ point. The spin-orbit splitting is well reproduced.

The first-principles calculations do not allow to separate directly the different contributions to the spin splitting, in contrast to a nearly-free electron model for a 2D electron gas [3]. The nearly-free electron model calculations fully confirm the findings of the *ab initio* calculations and show further that the in-plane potential gradient contributes considerably to the strength of the spin splitting. We conclude that the giant spin splitting in the Bi/Ag(111) surface alloy is the result of a strong in-plane potential gradient.

The Bi/Ag(111) surface alloy is the first system in which a giant spin splitting is observed. It goes beyond the giant spin-orbit bowing effect seen in the doped $GaAs_{1-x}Bi_x$ system [4], since here the spin-splitting is manipulated directly through the in-plane gradient. This in-plane gradient has its origin in the concept of surface alloying itself: Each Bi atom is surrounded by six Ag atoms, which results in a strong in-plane gradient of the potential, possibly enhanced further by the outward relaxation of the Bi atom. The threefold rotational symmetry of the surface destroys the inversion symmetry within the surface plane.

The density functional theory calculations show that the electronic surface states are strongly localized within the topmost surface layer, exposing them substantially to the in-plane gradient.

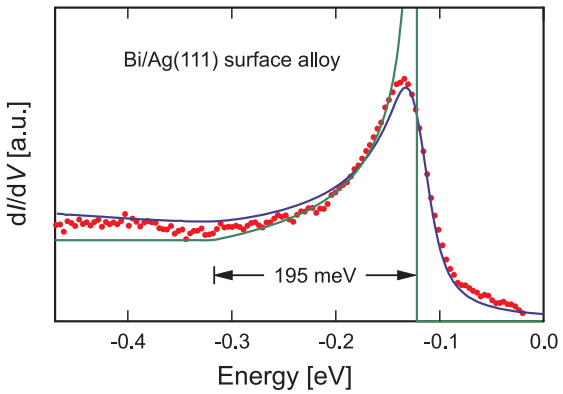

Figure 82: Differential conductance spectrum near the surface state onset for the Bi/Ag(111) surface alloy. The red dotted lines correspond to the measured dI/dV spectra, while the blue lines show a fit to the density of states within the Tersoff-Hamann model. The green lines show the unconvoluted density of states.

In addition, by scanning tunneling spectroscopy it is possible to extract the strength of the spin-splitting in a two-dimensional (2D) energy band from the local density of states [2]. A differential conductance spectrum of the Bi/Ag(111) surface alloy is shown in Fig. 82. It shows a peak at the onset of the surface state onset, which can be attributed to a singularity in the density of states. This observation can be qualitatively understood on the basis of spin-orbit split nearly free electron model. The density of states is given by (green line in Fig. 82):

$$D(E) = \begin{cases} \dfrac{|m^*|}{\pi\hbar^2}\sqrt{\dfrac{E_R}{E-E_0}} & ;\, E \in \text{Region I} \\ \dfrac{|m^*|}{\pi\hbar^2} = \text{const.} & ;\, E \in \text{Region II} \end{cases}$$

Here region I is between the band maximum and the crossing point and region II is beyond the crossing point. This introduces a characteristic energy $E_R = \hbar^2 k_0^2/2m^\star$ (also called Rashba energy), which is related to the strength of the spin-splitting. Using the Tersoff-Hamann model the Rashba Energy can be quantified in the fit (blue line in Fig. 82) to be 195 meV for the Bi/Ag(111) surface alloy. This is in excellent agreement with the Rashba energy determined from the ARPES measurements.

[1] *J. Henk, A. Ernst, L. Moreschini, M.C. Falub, D. Pacilé, P. Bruno, K. Kern and M. Grioni.* Physical Review Letters **98**, 186807 (2007).

[2] *Ast, C.R., G. Wittich, P. Wahl, R. Vogelgesang, D. Pacilé, M.C. Falub, L. Moreschini, M. Papagno, M. Grioni and K. Kern.* Physical Review B **75**, 201401 (2007).

[3] *Premper, P., M. Trautmann, J. Henk and P. Bruno.* Physical Review B **76**, 073310 (2007).

[4] *Fluegel, B., S. Francoeur, A. Mascarenhas, S. Tixier, E.C. Young and T. Tiedje.* Physical Review Letters **97**, 067205 (2006).

Effect of the spin-orbit interaction on the thermodynamic properties of crystals

M. Cardona and R.K. Kremer; L.E. Díaz-Sánchez and A.H. Romero (Querétaro, Mexico); X. Gonze (Louvain-la-Neuve, Belgium); J. Serrano (ESRF Grenoble, France)

In the past years we have carried out a series of experiments as well as *ab initio* calculations of the dependence of the specific heat of semiconductors and insulators on temperature and isotopic masses. Recent results on the binary lead chalcogenides PbS and PbSe revealed marked differences between the calculated and the experimental heat capacities and the phonon dispersion relations [1]. This finding raised the question of whether these discrepancies were due to the lack of spin-orbit (*s-o*) coupling in the *ab initio* electronic structure calculations.

To avoid computational problems especially arising from $\boldsymbol{q} \rightarrow 0$ divergences of the optical phonons related to the strongly ionic, nearly ferroelectric character of PbS and PbSe we extended our studies to metals and reinvestigated in detail the low-temperature heat capacities of high purity single crystals of Bi and calculated the phonon band structures and thermodynamical properties based on Density-Functional Perturbation Theory, including spin-orbit interaction. To compare with a closely related system, albeit with significantly reduced spin-orbit coupling, we performed heat capacity measurements and *ab initio* calculations also for antimony.

Bismuth and antimony are semimetals closely related to the lead chalcogenides. They have 10 valence electrons per primitive cell and a rhombohedral structure which can be derived from the structure of PbS by making both atoms equal and applying a Peierls-like distortion to the PbS cube, involving an elongation of one of its [111] axes. The structure is characterized by three parameters: The bond length a_0, the rhombohedral angle and a shift between the two sublattices. These parameters were determined by energy minimization. The results obtained for these parameters with and without *s-o* coupling differ by less than 1%. By including *s-o* coupling, excellent agreement with experimental phonon dispersion relations for Bi was obtained whereas without *s-o*, the calculated bands lying higher in frequency than the measured ones (not shown here).

Figure 83 displays a comparison of the experimental heat capacities of Bi and Sb with the calculated heat capacities with and without inclusion of *s-o* coupling. For Bi the discrepancies between experimental and calculated data (without *s-o* coupling) are largest near 10 K where the maximum in the quantity $C(T)/T^3$ occurs. The differences are significantly reduced if *s-o* coupling is included, the calculated curve now lying by about 7% higher than the experimental data. For the lighter element Sb the difference between calculated data with and without *s-o* coupling is less pronounced ($\approx 4\%$). The experimental data agree rather well with the data obtained without inclusion of *s-o* coupling.

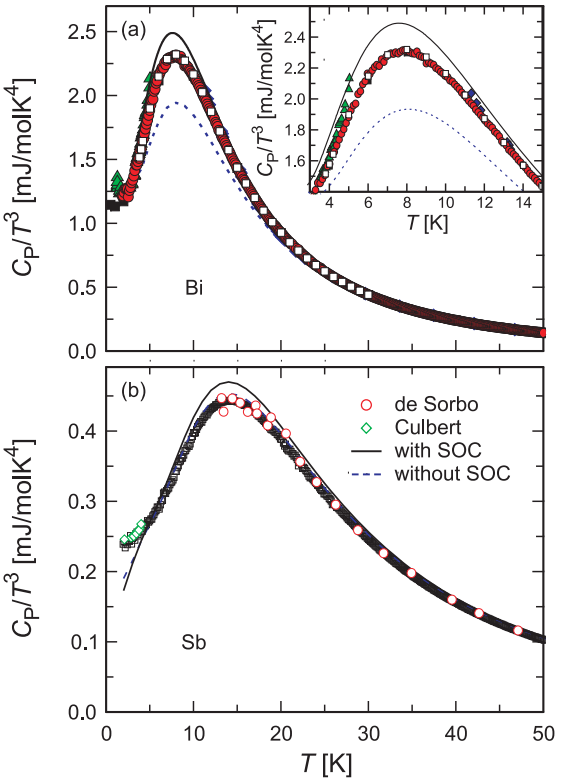

Figure 83: (a) Heat capacity of a Bi single crystal, purity 99.9999% [2]. Red filled circles compared with literature data obtained on polycrystalline samples. Black solid line: *ab initio* results with spin-orbit coupling included and without spin-orbit coupling (blue) dashed line. (b) Temperature dependence of the specific heat of Sb (open squares) are compared with data from the literature (see inset) [3] and with *ab initio* calculations with (black, solid) and without (blue, dashed) spin-orbit interaction (SOC).

In order to follow and quantify the effects of *s-o* interaction on the maximum in $C_\mathrm{p}/T^3_\mathrm{max}$, the rhombohedral lattice parameter a_0 and the cohesive energy E_c, we varied the spin-orbit interaction by multiplying the *s-o* coupling Hamiltonian by a factor $-1 < \lambda < 1$, and repeated the full *ab initio* calculations for several values of λ. The results are summarized in Figs. 84 and 85.

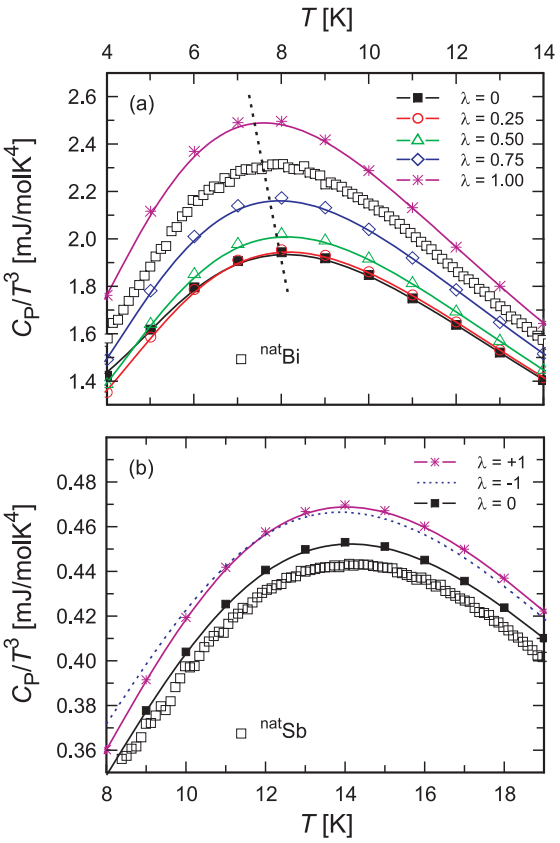

Figure 84: Measured and calculated heat capacities of Bi (a) and Sb (b). The calculations were performed with varying magnitude of the *s-o* coupling as indicated in the inset. Note that the maximum shifts to lower temperatures (inclined dashed line) with increasing *s-o* coupling, as corresponds to decreasing phonon frequencies (see text). The symbols show our experimental data, whereas the curves display the results of the calculations with various values of λ as specified in the insets.

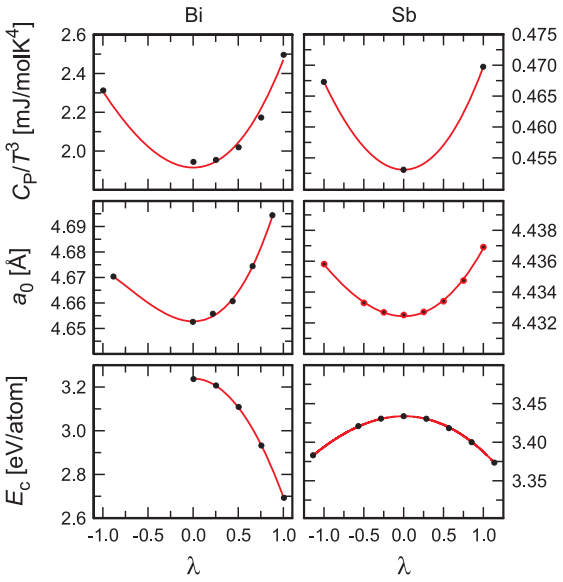

Figure 85: From top to bottom: Maxima of the quantity $C_p(T_{max})/T_{max}$ vs. *s-o* coupling parameter λ, energy minimized lattice parameter a_0 vs. *s-o* coupling parameter λ and cohesive energy of bismuth versus λ, calculated as discussed in the text. The circles (○) represent the results of our calculations, the dashed lines fits which lead to the parameters listed in the Tab. 4.

As noted above, the effects of *s-o* coupling on the calculated heat capacities of Bi are essential. The discrepancy in the maximum of C_p/T^3_{max} calculated with and without *s-o* coupling amounts to ≈25%. The maximum of C_p/T^3_{max} shifts to lower temperatures with increasing *s-o* coupling corresponding to decreasing phonon frequencies, an effect which has also been seen in the experimentally determined phonon dispersion relations. Best agreement of the experimental with the calculated heat capacity data is obtained with $\lambda \approx 0.8$.

Figure 85 reveals the strongly supralinear dependence of the *s-o* effect on C/T^3_{max}, the lattice constant a_0 and the cohesive energy E_c as a function of λ. E_c was obtained as the difference between the calculated total energy for the free atom and that for the solid, both calculated with the LDA approximation for exchange and correlation. All calculated quantities show a quasiparabolic dependence on λ, with a small but nevertheless significant contribution of a cubic term and can be well-fitted to the expression, $\propto c_0\,[1 + c_2\,\lambda^2\,(1 + c_3\,\lambda)]$. The fitted coefficients c_i are compiled in Tab. 4.

The absence of a linear term in λ is expected from the fact that the expansion of the *s-o* Hamiltonian in λ using perturbation theory contains terms only in λ^2 and higher orders, since linear terms in λ would imply a splitting between *z*-components of the spin upon the *s-o* interaction, a splitting that can only happen in the presence of a magnetic field.

Table 4:
Fit parameters c_i obtained by fitting a cubic polynomial (see text) to the calculated heat capacity maximum C_p/T^3_{max}, the lattice parameter a_0, and the cohesive energy E_c.

Quantity	Element	c_0	c_2	c_3
C_p/T^3_{max} [J/molK^4]	Bi	1914(23)	0.25(2)	0.17(5)
	Sb	453	0.034	0.079
a_0 [Å]	Bi	4.6528(5)	0.0064(2)	0.41(2)
	Sb	4.4324(1)	0.00089(2)	0.14(1)
E_c [eV/atom]	Bi	3.238(3)	–0.159(8)	0.058(52)
	Sb	3.4337(3)	–0.0162(2)	0.088(7)

Note that the square root of the ratio of the coefficients corresponding to the quadratic term in λ for the fits of a_0 and E_c of Bi and Sb, 2.7 and 3.1 respectively, is qualitatively similar to that of the *s-o* splitting, i.e., 1.7/0.7 = 2.42. This relation, which also holds for the dependence of the maximum value of C/T^3 on λ, implies a simple scaling of the effects of *s-o* interaction on the vibrational properties.

Following the same argument we conclude that the cube root of the ratio of $c_2 \times c_3$ for Bi to $c_2 \times c_3$ for Sb should also be close to the corresponding ration of *s-o* splittings (2.42). Using the values of these coefficients given in Tab. 4 we find an average value (for the three quantities in the table) of the cube root of the ratios of $c_2 \times c_3$ equal to 1.9, also close to the corresponding ratio of *s-o* splittings.

In conclusion, we have investigated the effect of *s-o* interaction on three thermodynamic properties, $C(T)$, a_0, and E_c, of the heavy element bismuth and compared them with those of the lighter isostructural element antimony. *s-o* coupling effects, apparently rather substantial for a first-principles calculation of the physical properties of solids, have not received much consideration in the literature so far. Their inclusion significantly reduces the discrepancies, e.g., between the experimental and calculated heat capacities of bismuth thus illustrating the importance of *s-o* interaction for the calculations of thermodynamic properties starting from *ab initio* electronic band structures for systems containing heavy atoms. These findings confirm our conjecture that similar discrepancies found for PbS and PbSe must be due to the lack of *s-o* coupling in the electronic structure calculations.

[1] *Cardona, M., R.K. Kremer, R. Lauck, G. Siegle, J. Serrano and A.H. Romero.* Physical Review B **76**, 075211 (2007) and unpublished results.

[2] *Díaz-Luis, L.E., A.H. Romero, M. Cardona, R.K. Kremer and X. Gonze.* Physical Review Letters **99**, 165504 (2007).

[3] *Serrano, J., R.K. Kremer, M. Cardona, G. Siegle, L.E. Díaz-Sánchez and A.H. Romero.* Physical Review B **77**, 054303 (2008).

Is there an interlayer band in α- and β-$ThSi_2$? An *N*MTO analysis

E. Zurek, O. Jepsen and O.K. Andersen

Since the discovery of superconductivity in MgB_2 much effort has been spent on studies of sp^2-bonded intercalated graphites and structurally related compounds (Fig. 86). With 4 electrons per boron, MgB_2 is isoelectronic with graphite, but is unique in having intercalated doubly-charged ions (Mg^{2+}) which lower the energy of the boron p_z-bands to the extent that holes occur at the top of the sp^2-bonding σ-bands. As first suggested by density-functional calculations, it is the strong coupling between these holes via the optical bond stretching modes which causes superconductivity with $T_c = 40$ K [1]. Whereas MgB_2 may thus be viewed as heavily hole-doped graphite, CaC_6, YbC_6, and Ca(AlSi), with respectively $4\frac{1}{3}$ and 5 electrons per C or Al/Si, are heavily electron-doped graphites with carriers in the ubiquitous interlayer band, which lies well above the σ-bands and crosses the p_z-antibonding π*-band. The interlayer band and the π*-band couple via buckling modes of the graphite sublattice and via in-plane modes of the intercalant sublattice, and this causes superconductivity with $T_c = 11$ K, 6 K, and 8 K, respectively [2]. The interlayer band has intercalant *s* and some d_{3z^2-1} character, but it exists also without intercalation. For the electron-phonon interaction it is important that the Wannier function of the interlayer band, chosen to be centered on the intercalant site, does not change sign upon 6-fold rotation, while the Wannier function of the π*-band has nodes between the C-atoms [2]. In this contribution we investigate whether a metallic interlayer band exists in the structurally related 6-electron compound $ThSi_2$ [3].

$ThSi_2$ can exist in one of two structures, depending upon the temperature of preparation. The hexagonal form, β-$ThSi_2$ shown at the top of Fig. 86, has the same AlB_2 structure as MgB_2: The silicon sublattice is cubic graphite (honeycomb) and the thorium atoms are located between two parallel hexagons thus forming triangular layers. The tetragonal form, α-$ThSi_2$, is a twisted version of this, and is shown at the bottom of Fig. 86: Starting out from a σ-bond in the *z*-direction (Si_1-Si_2 or Si_3-Si_4), the two remaining sp^2-directed orbitals at one end of the bond (Si_1 or Si_3) form σ-bonds lying in the *xz*-plane, while those at the other end (Si_2 or Si_4) form σ-bonds lying in the *yz*-plane. The silicon hexagons are thus cut and twisted to form intersecting honeycomb-stacks running in the *y*- and *x*-directions. At the intersections are the thorium atoms, which have 12 nearest silicon neighbors, like in β-$ThSi_2$. The α-form has two formula units per cell and the thorium sublattice is that of a high-pressure form of cesium (Cs IV). $ThSi_2$ is superconducting with the relatively low $T_c = 2$ K and 3 K for the β- and α-forms, respectively.

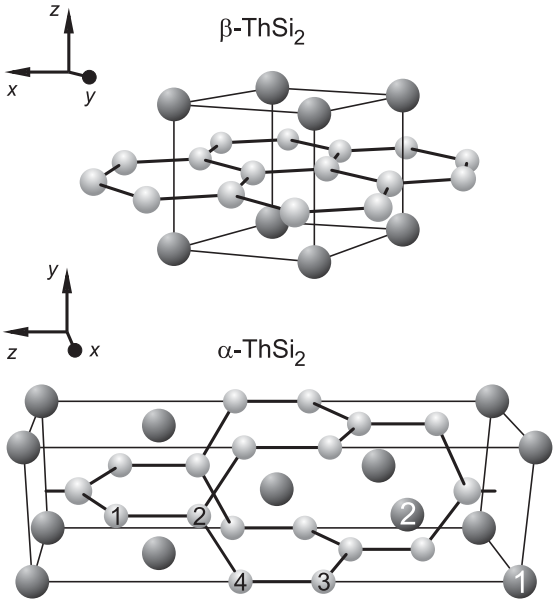

Figure 86: Unit cells of β- and α-$ThSi_2$. Si/Th are the white/grey atoms.

The upper parts of Figs. 87 and 88 show the LDA bands of β- and α-$ThSi_2$, respectively, with red and blue fatness (line thickness) proportional to the Si sp^2 and p_z partial-wave characters, respectively, and pink fatness proportional to the sum of the Th *s*- and d_{3z^2-1}-characters.

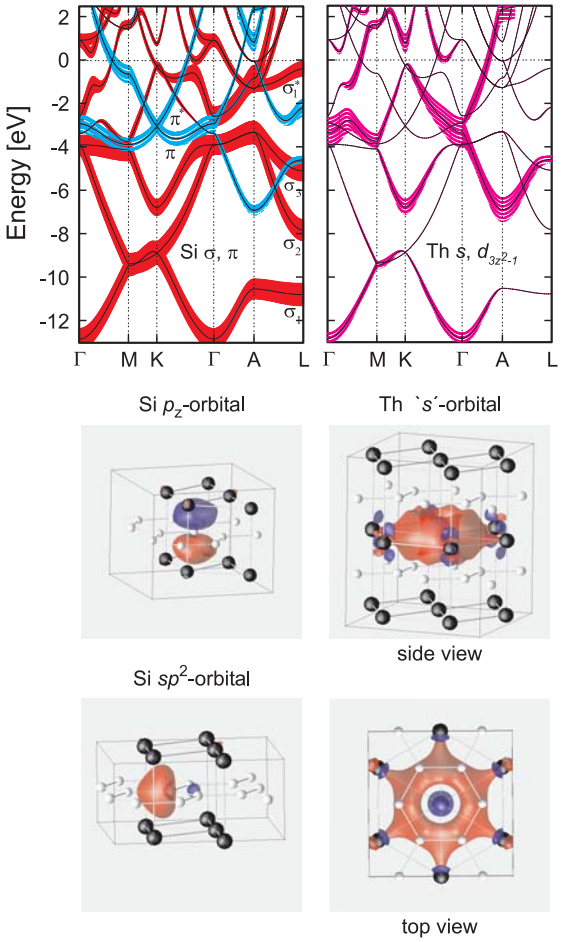

Figure 87: Top: Band structure of β-$ThSi_2$. The red/blue fatness is proportional to the Si sp^2/p_z character, and the pink fatness to Th *s*- and d_{3z^2-1}-character. Bottom: The Si sp^2- and p_z- and the Th *s*- (side and top view) *N*MTO Wannier-like functions which span the 2(3+1)+1 = 9 lowest bands, 6 of which are filled.

There are further characters which are not indicated, e.g., Th *d*. Six bands are full in the β-form and 12 in the α-form. Since the latter are bewilderingly complicated, we first explain those of the β-form (Fig. 87). At Γ, the three lowest states have σ-, the 4th Th-, the 5th π-, and the 6–8th sp^2-antibonding σ*-character. The π*-level is above the frame. Compared with the corresponding σ-levels in CaC_6 and YbC_6, the Si π-level is relatively higher and the Th level relatively lower, the latter being due to the relativistic mass-velocity and Darwin effects, as well as the higher filling of the Th-band. The three σ-bands are full, and so is essentially the lowest σ*-band, although in a region around M, it splits due to hybridization with the Th-band. The π- and π*-bands are also full, except near Γ, where the π*-band is empty and the Th-band full. Near ΓA, the lowest π- and π*-like bands are more Th- than Si-like. At the Fermi level, there are well-defined σ*-, π*-, and Th-bands.

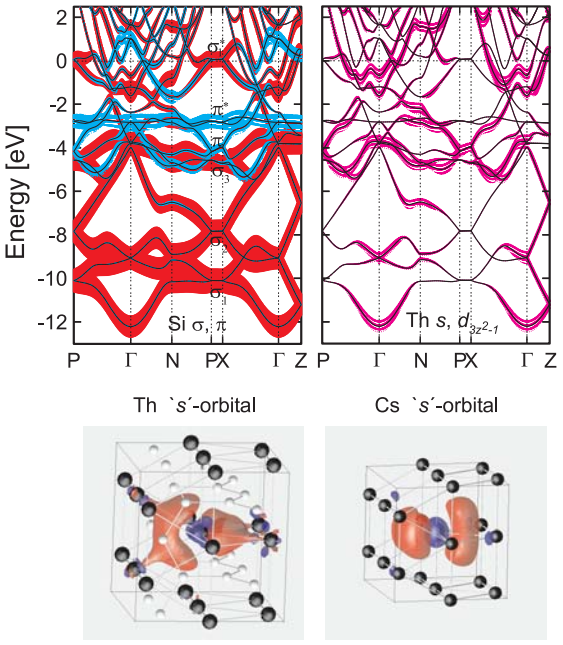

Figure 88: The same as in Fig. 87, for α-$ThSi_2$. The Si sp^2- and p_z-*N*MTOs are not shown since they are nearly identical to those calculated for β-$ThSi_2$. The Th-related orbital is strikingly different (seen here from the side). Also shown is the *N*MTO obtained for Cs-IV.

In order to decide whether the – somewhat fractured – Th-band can be viewed as the ubiquitous interlayer band, which by coupling to the σ*- and π*-bands via Si-buckling and Th-displacive modes, is the likely cause of the observed superconductivity, we consider its Wannier-like function. This we take as the Th *s*-like orbital of a complete, minimal basis set containing also the Si sp^2- and p_z-like orbitals generated by the *N*MTO downfolding-plus-*N*ization procedure [2-4]. The set of $1+2\times4=9$ *N*MTOs spans the occupied part of the 9 lowest bands exactly, and its orbitals are shown in the bottom part of Fig. 87. The Th *s*-*N*MTO has the property that it has *no* Th *s*-character on any *other* Th site and *no* Si *s*- or *p*-character. Similarly for

the Si sp^2- and p_z-*N*MTOs. Other partial-wave characters are present in the amounts needed to make the basis set complete. We see that the Th *s*-orbital *is* invariant to the 6-fold rotations, is shaped like a torus with a hole in the middle caused by the 7*s*- and $6d_{3z^2-1}$ characters, and bonds to 7*p*- and 6*d*-characters of the thorium neighbors in the plane. Since this orbital is very similar to the calcium-centered Wannier function for the interlayer band in CaC_6 and also for the vacancy $\boxdot C_6$ [2], we conclude that the Th-band in β-$ThSi_2$ *is* the interlayer band.

The bandstructure of α-$ThSi_2$, shown at the top of Fig. 88, may now be analyzed and found to be similar to that of β-$ThSi_2$, provided that the relation between the two structures (Fig. 86) is recognized. This result comes out much simpler if we construct the same minimal basis set as for the β-form. We then find that the Si sp^2- and p_z-*N*MTOs are so similar to those obtained for β-$ThSi_2$, that there is no point in showing them. At first, the Th *s*-*N*MTO in the bottom left panel of Fig. 88 appears to differ greatly from the interlayer orbital in β-$ThSi_2$ (Fig. 87), until one realizes that it *is* this torus-shaped orbital, but cut in two and twisted exactly like the Si-sublattice in Fig. 86.

Thus, for both allotropes of $ThSi_2$, the Th *s*-*N*MTO is strikingly similar to the previously calculated interlayer Wannier functions in graphites [2]. This suggests that the electron-phonon mechanism of superconductivity in $ThSi_2$ is similar to the one in the heavily electron-doped intercalated graphites where there are interlayer and π^*-bands at the Fermi level. In $ThSi_2$, also the σ^*-band is metallic. Since thorium is a heavy metal, one might fear that spin-orbit coupling between the several 6*d*-characters in α-$ThSi_2$ would remove the interlayer band from the Fermi level. But as fully relativistic calculations show, the Fermi surface is very little affected; there *is* in effect only one *d*-character.

A final remark: In elemental Cs IV, high pressure has transformed the cesium 6*s*-electron into a 5*d*-electron whose orbital is the one shown in the bottom right part of Fig. 88. Its shape is seen to be that of the Th-orbital in α-$ThSi_2$, but turned 90° in order to make up for the lack of silicon backbone, as conjectured by von Schnering and Nesper [3-5].

[1] *Kortus, J., I.I. Mazin, K.D. Belashchenko, V.P. Antropov, and L.L. Boyer.* Physical Review Letters **86**, 4656–4659 (2001); *An, J.M. and W.E. Pickett.* Physical Review Letters **86**, 4366–4369 (2001); *Kong, Y., O.V. Dolgov, O. Jepsen and O.K. Andersen.* Physical Review B **64**, 020501 (2001).

[2] *Giantomassi, M., L. Boeri and G.B. Bachelet.* Physical Review B **72**, 224512 (2005); *Boeri, L., G.B. Bachelet, M. Giantomassi and O.K. Andersen.* Physical Review B **76**, 064510 (2007); *Andersen, O.K., E. Zurek, L. Boeri, O. Jepsen, G.B. Bachelet and M. Giantomassi.* MPI-FKF Wissenschaftlicher Tätigkeitsbericht 2006, 60–62 (2007); the front-page logo is the interlayer Wannier function of CaC_6.

[3] *Zurek, E.* Thesis, University of Stuttgart (2006).

[4] *Andersen, O.K. and T. Saha-Dasgupta.* Physical Review B **62**, R16219 (2000); *Zurek, E., O. Jepsen and O.K. Andersen.* ChemPhysChem **6**, 1934–1942 (2005).

[5] *von Schnering, H.G. and R. Nesper.* Angewandte Chemie International Edition **26**, 1059–1080 (1987).